



SPRING / SUMMER 2019

VOLUME 11, NUMBER 1

Print ISSN: 2152-4157  
Online ISSN: 2152-4165

WWW.IJERI.ORG

# International Journal of Engineering Research & Innovation

Editor-in-Chief: Mark Rajai, Ph.D.  
California State University Northridge



Published by the  
**International Association of Journals & Conferences**



[www.ijeri.org](http://www.ijeri.org)

Print ISSN: 2152-4157  
Online ISSN: 2152-4165



[www.iajc.org](http://www.iajc.org)

# INTERNATIONAL JOURNAL OF ENGINEERING RESEARCH AND INNOVATION

## **ABOUT IJERI:**

- IJERI is the second official journal of the International Association of Journals and Conferences (IAJC).
- IJERI is a high-quality, independent journal steered by a distinguished board of directors and supported by an international review board representing many well-known universities, colleges, and corporations in the U.S. and abroad.
- IJERI has an impact factor of **1.58**, placing it among an elite group of most-cited engineering journals worldwide.

## **OTHER IAJC JOURNALS:**

- The International Journal of Modern Engineering (IJME)  
For more information visit [www.ijme.us](http://www.ijme.us)
- The Technology Interface International Journal (TIIJ)  
For more information visit [www.tiij.org](http://www.tiij.org)

## **IJERI SUBMISSIONS:**

- Manuscripts should be sent electronically to the manuscript editor, Dr. Philip Weinsier, at [philipw@bgsu.edu](mailto:philipw@bgsu.edu).

For submission guidelines visit  
[www.ijeri.org/submissions](http://www.ijeri.org/submissions)

## **TO JOIN THE REVIEW BOARD:**

- Contact the chair of the International Review Board, Dr. Philip Weinsier, at [philipw@bgsu.edu](mailto:philipw@bgsu.edu).

For more information visit  
[www.ijeri.org/editorial](http://www.ijeri.org/editorial)

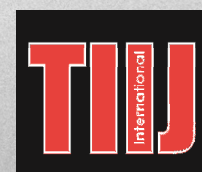
## **INDEXING ORGANIZATIONS:**

- IJERI is indexed by numerous agencies. For a complete listing, please visit us at [www.ijeri.org](http://www.ijeri.org).

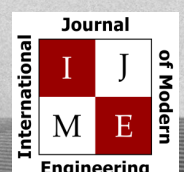
## **Contact us:**

**Mark Rajai, Ph.D.**

Editor-in-Chief  
California State University-Northridge  
College of Engineering and Computer Science  
Room: JD 4510  
Northridge, CA 91330  
Office: (818) 677-5003  
Email: [mrajai@csun.edu](mailto:mrajai@csun.edu)



[www.tiij.org](http://www.tiij.org)



[www.ijme.us](http://www.ijme.us)

---

# INTERNATIONAL JOURNAL OF ENGINEERING RESEARCH AND INNOVATION

The INTERNATIONAL JOURNAL OF ENGINEERING RESEARCH AND INNOVATION (IJERI) is an independent and not-for-profit publication, which aims to provide the engineering community with a resource and forum for scholarly expression and reflection.

IJERI is published twice annually (fall and spring issues) and includes peer-reviewed research articles, editorials, and commentary that contribute to our understanding of the issues, problems, and research associated with engineering and related fields. The journal encourages the submission of manuscripts from private, public, and academic sectors. The views expressed are those of the authors and do not necessarily reflect the opinions of the IJERI editors.

## EDITORIAL OFFICE:

Mark Rajai, Ph.D.  
Editor-in-Chief  
Office: (818) 677-2167  
Email: [ijmeeditor@iajc.org](mailto:ijmeeditor@iajc.org)  
Dept. of Manufacturing Systems  
Engineering & Management  
California State University-  
Northridge  
18111 Nordhoff Street  
Northridge, CA 91330-8332

## THE INTERNATIONAL JOURNAL OF ENGINEERING RESEARCH AND INNOVATION EDITORS

### *Editor-in-Chief:*

**Mark Rajai**

California State University-Northridge

### *Associate Editors:*

**Paul Wilder**

Vincennes University

**Li Tan**

Purdue University North Central

### *Production Editor:*

**Philip Weinsier**

Bowling Green State University-Firelands

### *Subscription Editor:*

**Morteza Sadat-Hossieny**

Northern Kentucky University

### *Web Administrator:*

**Saeed Namyar**

Advanced Information Systems

### *Manuscript Editor:*

**Philip Weinsier**

Bowling Green State University-Firelands

### *Copy Editors:*

**Li Tan**

Purdue University North Central

**Ahmad Sarfaraz**

California State University-Northridge

### *Technical Editors:*

**Marilyn Dyrud**

Oregon Institute of Technology

### *Publisher:*

**Bowling Green State University Firelands**

---

# TABLE OF CONTENTS

<i>Editor's Note: Academic Active-Shooter Incidents</i> .....	3
Philip Weinsier, IJERI Manuscript Editor	
<i>Analyzing Response Communication Mitigation Methods through Simulation Modeling</i> .....	5
Katherine E. Reichart, Purdue University; Anna R. Larson, Purdue University; Kristal K. Smith, Purdue University; J. Eric Dietz, Purdue University	
<i>Developing an Open Source, Inexpensive, Large-Scale Polar Configuration 3D Printer</i> .....	13
Sourabh Prashant Deshpande, University of Cincinnati; Shrinivas Kulkarni, Michigan Technological University; Sid Shah, Michigan Technological University; John Irwin, Michigan Technological University	
<i>A Comparative Study of the Thermal Efficiency of Solar Vacuum-Tube versus Flat-Plate Collectors for Water Heating Systems</i> .....	23
S.V. Vishnu Samudrala, Zimmer Biomet; Ahmed ElSawy, Tennessee Technological University; Mohan Rao, Tennessee Technological University; Stephen Idem, Tennessee Technological University	
<i>Design and Development of a GUI for RF Communications</i> .....	30
Ehsan Sheybani, University of South Florida; Giti Javidi, University of South Florida	
<i>A Diagnostic Clock for Verification of Image Time Synchronization</i> .....	37
Curtis Cohenour, Ohio University	
<i>Assessing the Effectiveness of an Automatic Door Lock System by Discharge Detection to Lower Casualties during an Academic Active Shooter Incident</i> .....	46
Jae Yong Lee, Purdue University; James Eric Dietz, Purdue University	
<i>Instructions for Authors: Manuscript Formatting Requirements</i> .....	53

# IN THIS ISSUE (P.46): ACADEMIC ACTIVE-SHOOTER INCIDENTS

Philip Weinsier, IJERI Manuscript Editor

---

So many of our children have experienced violent deaths in our nation's schools; the one place, we would like to think, where our children will be safe outside of their homes. Yet anyone listening to the news since the inventions of radio and TV are hearing otherwise. By any measure, and regardless of the source—the National Education Association (NEA), the American Federation of Teachers (AFT), Everytown (for gun safety), K12academics, CNN—too many of our children have lost their lives in school shootings. Due to media attention, TV viewers can be forgiven if they perceive school shootings as a relatively new phenomenon—15 events in 2019 alone; 39 between 2010 and 2018; and another 147 deaths between 2000 and 2010. But according to these same sources, there were another 98 incidents going back to 1764. In that first recorded event, nine of the 11 children and the schoolmaster were shot and killed.

Mass school shootings—as if it should make a difference how many children are slaughtered; even one should be cause for national concern and federal action—comprise only 1% of school gun violence incidents, while logging 28% of the total number of deaths. But lest we think that all of these shootings were perpetrated by crazed current or former students (40%) or faculty/staff or resource officers, it should be noted that 44% are actually suicides and attempted suicides, unintentional shootings, and legal interventions; not sure what that last category is. At least in New York, 79% of active-shooter incidents in schools were perpetrated by a school-aged student (and a current or recent graduate of the school).

The next question that we all ask is, where are these children getting their guns? As the vast majority of these shooters are under 18, they are not buying the guns themselves (at least not legally). Evidence suggests that 78% of them get their weapons from their own homes or those of friends and relatives. So far, all one can say is that there is a problem; a problem that has myriad facets. Given that government, irrespective of your opinion of the current administration, is either incapable or simply not doing enough on its end to mitigate the problem, society is trying to find its own solu-

tions. Instead of getting guns out of the hands of potential shooters—one facet of the problem that our elected officials will argue ad nauseam without effective results—there are many researchers working on scenarios to keep students safe, or at least as safe as possible, when an active-shooter situation arises. Currently, *run.hide.fight* (RHF) is a national mantra for being prepared for such events. But, according to the authors of this featured article (see *Assessing the Effectiveness of an Automatic Door Lock System by Discharge Detection to Lower Casualties during an Academic Active Shooter Incident* on p.46), modeling a scenario similar to the Parkland shooting suggests that the application of RHF without situational awareness of the shooter's location could cause higher casualty rates by an average of more than 1.26 individuals. Thus, in their study, the authors compared the casualty rates of two models.

The first model consisted only of hide (shelter-in-place) and run (evacuate). The second model applied the first model's components with an automatic door lock system, which was triggered by discharge detection. To exclude human participation, and to prevent physiological and psychological impact, agent-based modeling (ABM) was used to recreate a one-story academic infrastructure with 26 lecture halls and three exits containing 600 unarmed individuals. The flexibility of ABM allows multiple iterations, while manipulating various parameters. The ABM approach in active-shooter research also eliminates human error and logistical issues. The outcome of this study evaluates the effectiveness of an automated door lock system, based on firearm discharge detection with a campus-wide alert system to conduct lockdown.

As frustrating and embarrassing as it has been for, well, centuries now, it is my sincere hope that our techniques for increasing student safety will outpace the ability of frustrated, revengeful, and deranged individuals to enter our schools and harm our children. And by harm, I mean not only save the anguish on the part of the parents in their children's deaths, but also the life-long, debilitating, and mentally scarring effects on those surviving such shootings.

## Editorial Review Board Members

Mohammed Abdallah	State University of New York (NY)	Troy Ollison	University of Central Missouri (MO)
Paul Akangah	North Carolina A&T State University (NC)	Reynaldo Pablo	Purdue Fort Wayne (IN)
Nasser Alaraje	Michigan Tech (MI)	Basile Panoutsopoulos	Community College of Rhode Island (RI)
Ali Alavizadeh	Purdue University Northwest (IN)	Shahera Patel	Sardar Patel University (INDIA)
Lawal Anka	Zamfara AC Development (NIGERIA)	Thongchai Phairoh	Virginia State University (VA)
Jahangir Ansari	Virginia State University (VA)	Huyu Qu	Broadcom Corporation
Kevin Berisso	Memphis University (TN)	Desire Rasolomampionona	Warsaw University of Tech (POLAND)
Pankaj Bhambri	Guru Nanak Dev Engineering (INDIA)	Michael Reynolds	University of West Florida (FL)
Michelle Brodke	Bowling Green State Univ. Firelands (OH)	Nina Robson	California State University-Fullerton (CA)
Shaobiao Cai	Minnesota State University (MN)	Marla Rogers	Wireless Systems Engineer
Rajab Chaloo	Texas A&M University Kingsville (TX)	Dale Rowe	Brigham Young University (UT)
Isaac Chang	Illinois State University (IL)	Karen Ruggles	DeSales University (PA)
Shu-Hui (Susan) Chang	Iowa State University (IA)	Anca Sala	Baker College (MI)
Rigoberto Chinchilla	Eastern Illinois University (IL)	Alex Sergeev	Michigan Technological University (MI)
Phil Cochrane	Indiana State University (IN)	Mehdi Shabaninejad	Zagros Oil & Gas Company (IRAN)
Curtis Cohenour	Ohio University (OH)	Hiral Shah	St. Cloud State University (MN)
Emily Crawford	Claflin University (SC)	Mojtaba Shivaie	Shahrood University of Technology (IRAN)
Dongyang (Sunny) Deng	North Carolina A&T State University (NC)	Musibau Shofoluwe	North Carolina A&T State University (NC)
Z.T. Deng	Alabama A&M University (AL)	Amitkumar B. Solanki	Government Engineering College (INDIA)
Sagar Deshpande	Ferris State University (MI)	Jiahui Song	Wentworth Institute of Technology (MA)
David Domermuth	Appalachian State University (NC)	Carl Spezia	Southern Illinois University (IL)
Marilyn Dyrud	Oregon Institute of Technology (OR)	Michelle Surerus	Ohio University (OH)
Mehran Elahi	Elizabeth City State University (NC)	Harold Terano	Camarines Sur Polytechnic (PHILIPPINES)
Ahmed Elsayy	Tennessee Technological University (TN)	Sanjay Tewari	Missouri University of Science & Tech (MO)
Cindy English	Millersville University (PA)	Vassilios Tzouanas	University of Houston Downtown (TX)
Ignatius Fomunung	University of Tennessee Chattanooga (TN)	Jeff Ulmer	University of Central Missouri (MO)
Ahmed Gawad	Zagazig University EGYPT	Abraham Walton	University of South Florida Polytechnic (FL)
Mohsen Hamidi	Utah Valley University (UT)	Haoyu Wang	Central Connecticut State University (CT)
Mamoon Hammad	Abu Dhabi University (UAE)	Jyhwen Wang	Texas A&M University (TX)
Gene Harding	Purdue Polytechnic (IN)	Boonsap Witchayangkoon	Thammasat University (THAILAND)
Bernd Haupt	Penn State University (PA)	Shuju Wu	Central Connecticut State University (CT)
Youcef Himri	Safety Engineer in Sonelgaz (ALGERIA)	Baijian (Justin) Yang	Purdue University (IN)
Delowar Hossain	City University of New York (NY)	Eunice Yang	University of Pittsburgh Johnstown (PA)
Xiaobing Hou	Central Connecticut State University (CT)	Xiaoli (Lucy) Yang	Purdue University Calumet (IN)
Shelton Houston	University of Louisiana Lafayette (LA)	Faruk Yildiz	Sam Houston State University (TX)
Ying Huang	North Dakota State University (ND)	Yuqiu You	Ohio University (OH)
Christian Bock-Hyeng	North Carolina A&T University (NC)	Pao-Chiang Yuan	Jackson State University (MS)
Pete Hylton	Indiana University Purdue (IN)	Jinwen Zhu	Missouri Western State University (MO)
John Irwin	Michigan Tech (MI)		
Toqeer Israr	Eastern Illinois University (IL)		
Sudershan Jetley	Bowling Green State University (OH)		
Alex Johnson	Millersville University (PA)		
Rex Kanu	Purdue Polytechnic (IN)		
Reza Karim	North Dakota State University (ND)		
Manish Kewalramani	Abu Dhabi University (UAE)		
Tae-Hoon Kim	Purdue University Calumet (IN)		
Chris Kluse	Bowling Green State University (OH)		
Doug Koch	Southeast Missouri State University (MO)		
Resmi Krishnankuttyrema	Bowling Green State University (OH)		
Zaki Kuruppallil	Ohio University (OH)		
Shiyong Lee	Penn State University Berks (PA)		
Soo-Yen (Samson) Lee	Central Michigan University (MI)		
Chao Li	Florida A&M University (FL)		
Dale Litwhiler	Penn State University (PA)		
Mani Manivannan	ARUP Corporation		
G.H. Massiha	University of Louisiana (LA)		
Thomas McDonald	University of Southern Indiana (IN)		
David Melton	Eastern Illinois University (IL)		
Shokoufeh Mirzaei	Cal State Poly Pomona (CA)		
Sam Mryyan	Excelsior College (NY)		
Jessica Murphy	Jackson State University (MS)		
Rungun Nathan	Penn State Berks (PA)		
Arun Nambiar	California State University Fresno (CA)		
Aurenice Oliveira	Michigan Tech (MI)		

# ANALYZING RESPONSE COMMUNICATION MITIGATION METHODS THROUGH SIMULATION MODELING

Katherine E. Reichart, Purdue University; Anna R. Larson, Purdue University; Kristal K. Smith, Purdue University; J. Eric Dietz, Purdue University

## Abstract

Emergencies rely heavily on succinct and controlled announcements from a singular verified source. However, this has been an ideal, not reality. Often, veritable communication has occurred after events, as official sources may not have been available to comment or provide personal instruction to individuals. Current communication simulation modeling involves communication systems in commutation with actual communication. Systems are not the only way information is spread. In this study, the authors analyzed formal and informal response methods in an emergency at a large event. By comparing multiple methods in a systems dynamic model, the researchers estimated the relative value of four communication sources in terms of impact and response metrics. The results influenced subsequent agent-based models that reflected a real evacuation of messaging. The study resulted in increased understanding of evacuation communication procedures as well as the simultaneous testing of multiple forms of communication. The models proved that the most reliable and rapid communication has the most impact on saving lives. Additionally, these procedures gave insight into communication effectiveness as well as the best combinations of messaging. Thus, these models, as estimates, should offer insight into the current communication response procedures and their future applications.

## Introduction

Current communication simulation modeling should involve communication systems in commutation with actual communication. Consider that an Amber alert and an online network might be similar in communication structure, but not in actual practice. Miscommunication in an online network means losing all connection. In an emergency, false and inconsistent messages occur. According to the Department of Homeland Security, emergencies rely heavily on succinct and controlled announcements from a singular verified source. However, this is an ideal as opposed to the reality (DHS, 2014). Communication will often be announced after the event, as official sources may not be available to comment immediately or provide personal instruction to individuals. Worse, the communication itself will stem from various sources that may worsen the emergency. An example of multiple sources would be the difference between formal and informal sources.

When modeling active shooter scenarios, communicating proper procedures saves lives. Notifying authorities increases response time, which prevents fatal casualties. The shooter will engage the police instead. In the 2015 Orlando nightclub shooting, police were notified at 2:02 am from an off-duty officer acting as a security guard (Ellis, Fantz, Karimi, & McLoughlin, 2016). This was four minutes after shooting started. However, additional external communication did not only come from the Orlando police department. Rather, the nightclub itself used social media to communicate with patrons. People inside also provided personal and external communication to the police or family members. Active shooters represent a scenario in which communication and procedure must be set in place prior to the emergency to accurately work. In this way, simulation modeling can provide “practice” in the distribution of responders, areas of weakness, and effective communication. Choosing a simulation modeling source means selecting a system that provides multiple modeling scenarios. AnyLogic Personal Learning Edition (PLE) affords the creation of limited yet diverse models. Using agent-based logic, modeling communication could be as realistic and individualized as needed.

## Venue Case Studies

Venues must adapt to different daily scenarios, as crowds change with the event. Therefore, getting an accurate evacuation time is difficult, mostly because publishing this data has the potential to hurt a venue’s security. Based on evacuation times in apartment buildings, the average time it takes to start evacuating (from a fire) is approximately 10 minutes, assuming alert systems are in place (Proulx, 1995). In combination with that time, the average evacuation took approximately 22 minutes to complete. However, this study was done on apartment buildings, as opposed to a large event venue like a stadium. Given the magnitude of such, evacuation times are more akin to typical exit procedures. However, these times are not measured and may be skewed as patrons are not forced to leave. Therefore, the aforementioned study may be more useful to compare timing than data collected from an after-hours event. This study also took mobility constraints into consideration involving those with special needs. Ultimately, the study does show that communication effects evacuation rates. The next step was to compare this information to large event venues and their communication methods.

---

In a 2014 study of Ladd Pebbles Stadium in Mobile, Alabama, focusing on stadium design, researchers spoke to the international standard of eight minutes for a stadium evacuation to occur. This study focused on the physical limitations associated with evacuations (crowding, collisions, social norms, etc.). However, very little attention was paid to communication factors that could affect timing in an emergency. Instead, the study focused on evacuation flow rate simulation and avoiding and assuming communication dynamics (Aldana, Fox, Diehl, & Dimitoglou, 2014). However, case studies show how vital communication is to evacuation planning. At AT&T Stadium, staff members are given a rundown on their tasks of the day and what to expect in terms of safety at the beginning of each shift. These task sheets include updates and reminders for the event and provide photos of what the passes and wristbands look like, so there are no copies (AT&T, 2018). It also reminds them if they see something, to say something. Each staff member is also expected to get a formal safety briefing from their supervisor prior to doors opening.

However, arenas are not the only example of a large event venue. University stadiums, arenas, and event centers are typically less secure and at higher risk for an emergency. Surveying three universities and their plans offered a more comprehensive list of evacuation procedures and methods. Additionally, these case studies offered the opportunity to see how they communicated information consistently to both long-time and first-time visitors. Though they also showed methods related to staffing, this was not an important factor for the current research project. Townson University has a public version of their arena's emergency response plan, and they outline a list of important information items for their event staff to know before their event. This list covers familiarizing staff and contractors on emergency procedures, fire procedures, emergency exit policies, equipment and seating policies, and other general rules.

The Townson report also covers the procedures during an emergency. As soon as an incident occurs, it is noted on the PA and via a bullhorn, in case of a fire alarm or PA equipment failure; the TUPD will designate a safe location outside; management will direct patrons during evacuation, and will use the radio for communication, and an operations commander will be assigned. These procedures are based on the National Incident Management System (NIMS), the National Response Framework (NRF), and the Incident Command System (ICS). These provide guidelines for preparedness and compliance. Anyone involved in security management should be fully aware, especially when ensuring the safety of over several hundred people (Towson, 2018). From these case studies, responses require necessary preparation and practice. Based on this information, evacua-

tion times should be estimated at approximately 20 minutes for an average venue with systems in place prior to the event itself. This time includes both the processing and actual physical evacuation time. The communication methods employed by these venues will be further explored in the following section.

## Emergency Communication Methods

In 2008, the Department of Homeland Security designed a planning guide for emergencies in stadiums. The guide has a section for a notification system during emergencies. During emergencies, understanding the different reactions that people can have is important to consider. Using the different possibilities can be helpful in designing an efficient notification system. The employees also need to be trained on all aspects of the system to be sure that communication will be effective. Using common language during emergencies allows for everyone to understand. The guide also advises everyone to ensure that they have a plan for displaying information (screens, jumbotrons, etc.), along with having employees check areas without any displays (DHS, 2008). Thus, communication response methods should relate to two communication systems: visual and audio. Sight and hearing are the primary ways that any person will begin to understand a message.

Stadiums typically have public announcement systems that will take into consideration both visual and auditory public announcement systems, but do not capitalize on additional communication systems that may be available to their audience. According to Kenneth Burke, the percentage rate of text messages being opened is 99%. Burke's article also states that 95% of text messages are opened within three minutes and, on average, they are read in under five seconds (Bankers, 2018). This statistic is particularly useful, considering that many stadiums have fan text messaging that could evolve into an emergency communication service. For example, Bankers Life Fieldhouse, a stadium in Indianapolis, Indiana, offers several different fan information services. Among website information, is the texting service that is offered to fans. Bankers Life Fieldhouse offers a texting service that fans can use if they ever encounter anything suspicious during events. The service is anonymous so they can inform building management without needing to give any personal information. Bankers Life Fieldhouse also specifies that if the service is misused, the number will be blocked for a full 24 hours (2018).

According to Cutlip and Center's *Effective Public Relations* (2013), there are several communication methods to apply to audiences (Broom, Sha, Seshadrinathan, Center, & Cutlip, 2013). Among the various communication models,

---

and relevant to communications in emergency management, the mass communication model is the most effective. The mass communications model has six elements: 1) the sender; 2) the message; 3) the medium or channel; 4) the receivers; 5) relationship contexts; and, 6) the social environment. Therefore, the sender is the source of the impact and can influence how it is received (Broom et al., 2013). Consequently, credibility intensifies information and could impact how effective a message is. A message is information that is sent or given to someone.

Furthermore from Cutlip and Center, messages are categorized into “text, verbal, multimedia, print, etc.” (Broom et al., 2013). Assumption suggests that emergency management messages have to be clear and concise. However, interpretation occurs when communicating with the masses and must be considered as a potential obstacle when crafting a message (Broom et al., 2013). The medium or channel that a message uses has equal importance to the message. From a 1971 body language study, face-to-face communication delivers effective communication information, yet 70-90% of communication is through nonverbal cues like gestures and facial expressions (Mehrabian, 1971). Such direct communication is valuable, but using technology as a medium for communication, such as social media, has resulted in creating more ways to communicate during emergencies (Broom et al., 2013). These options should be explored more fully in terms of emergency communications.

Alertus Technologies is a unified mass notification communication system. Alertus is often used for large events and companies for emergency situations. Alertus utilizes a combination of communication methods to maximize the possibility of reaching all parties. The different methods include text messaging, email, public announcement systems, digital signage, and desktop computers. A few companies that utilize Alertus Technologies include Disney, ESPN, and Toronto Pan AM Sports Centre (Alertus Technologies, 2018). This technology system appears to encompass all communication systems. However, the full system relies on the combination of systems. Whether this combination is effective or not depends on how accurate or effective the communication is. Alertus does what many arenas are capable of but, in a way, that puts the control in a unified separate entity.

## Methodology

In developing a way to model response communication, the authors determined that a system dynamics model would provide a new look at response communication. Response communication requires speed, time, and people. Balancing these three variables is essential to effective communica-

tion. Some constants, such as communication and evacuation rate, can be influenced by these variables. Thus, communication is a system that can be made more effective and accurate through modeling. The systems dynamics model being used was based on a Bass diffusion model. Developed in 1969 by Frank M. Bass and John A. Norton, a Bass diffusion model represents how a potential market is affected by advertisers and word of mouth (1987). Advertising has the potential to spread a concise, clear, and strong message with little to no resources. Thus, this model is a great reference for emergency communication.

Regarding this specific project, the Bass Diffusion model was changed to reflect emergency communication. This method was chosen based on how well advertisement mirrors communication. It necessitates and requires effective understanding, but also showcases errors that are corrected based on an alternate system. Bass diffusion takes communication by word of mouth into consideration, and is a large part of emergency communication. If all emergency communication systems were to fail, word of mouth would still be prevalent. Thus, word of mouth acts as a constant in this current model of emergency response communication. However, it has an obvious error rate regarding miscommunication and timely understanding.

## Bass Diffusion Model

Figure 1 shows how initial method research was conducted in order to see how well a Bass Diffusion model could adapt to emergency communication. By replacing the population to reflect the emergency at hand, the communication rate was no longer influenced by advertisement but by an auditory public announcement (PA) system. As mentioned earlier, word-of-mouth communication is still reflected and influenced by contact rate and the evacuation message rate (Norton & Bass, 1987). The model appeared to accurately reflect evacuation message procedures, including a delay that reflects understanding or processing time.

Regarding this study, the error lies in uniformity of message. Different communication systems have different challenges. The message to evacuate goes through several different paths, thus some of the messages are delayed, whether through human or technologically dictated circumstances. Developing a flowchart allowed the authors to show the specific challenges associated with each system and how they could apply to the model. Figure 2 shows how the steps associated with each system should result in understanding. This is where the Bass Diffusion model ends, as understanding implies that they have fully received the evacuation message. This does not account for the actual time that it would take for a person to evacuate (a lengthier process).

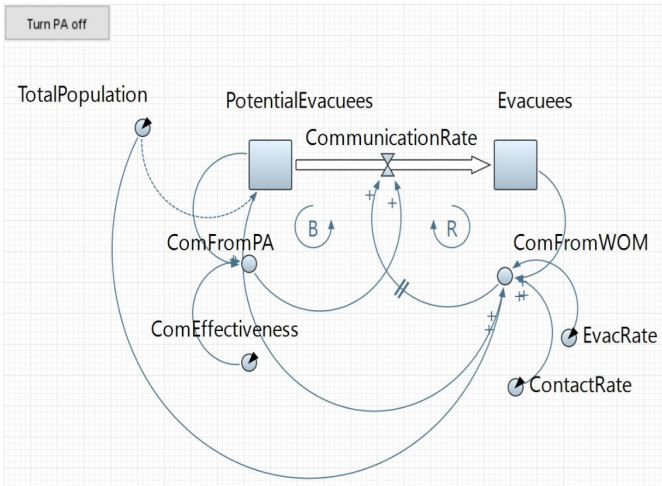


Figure 1. Original bass diffusion model.

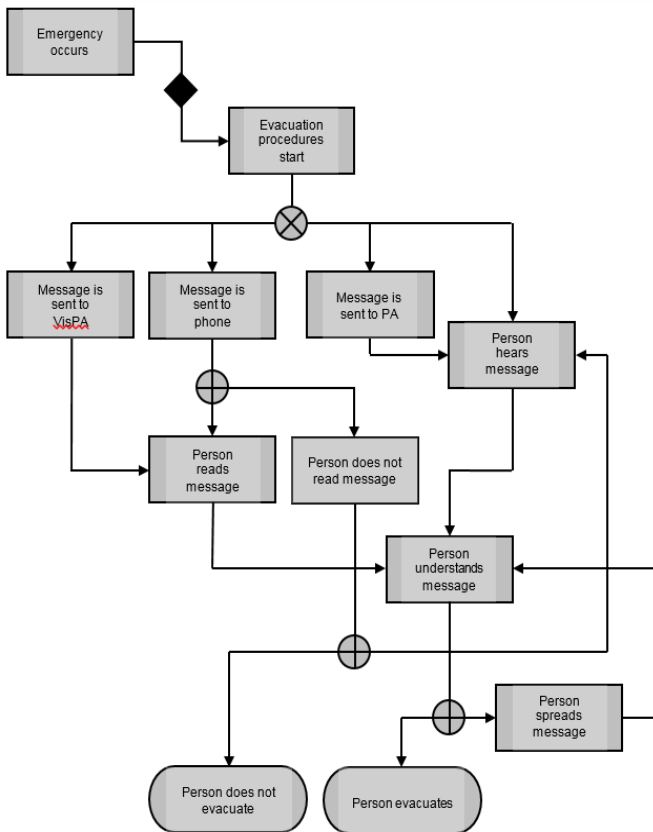


Figure 2. Communication flowchart.

The flowchart shows the four systems that could be modeled in an evacuation communication scenario. This is meant to come from the viewpoint of evacuees, not the first responders that would arrive. Therefore, the communication systems are all processes that the average person would have available. The four communication methods used were

an auditory PA system, visual PA system, texting notification system, and word of mouth. Figure 3 shows these systems.

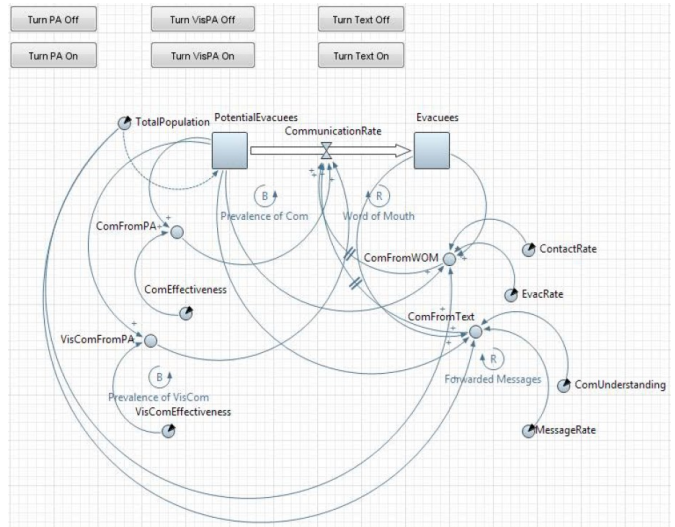


Figure 3. Final bass diffusion model.

For example, limited research suggests that public announcement systems are 60% effective at distributing a message (Alertus Technologies, 2018). This comes from public relations data as opposed to testing of several emergency public announcement systems. However, this assumes that the system is in perfect working order without any limitations (noise, miscommunication, etc.). Because the model is highly flexible, these circumstances can be reflected by inputting different numbers into the effectiveness variables. Using averages obtained from studies of similar systems, effectiveness was a variable inputted at different levels, depending on which system was in use. Thus, effectiveness for both public announcement systems (auditory and visual) used the same initial effectiveness rating of 60%, while the texting system was given a 50% effectiveness rating but with a message rate of approximately 5%, considering how often people would check their phones in each emergency. The five-second delay was implemented in the program as well. Text message systems align closely with word of mouth, as they are a technological reflection of the same process, but with higher numbers.

Finally, word-of-mouth communication had a contact rate of approximately 1.1%, as shown in prior Bass Diffusion models. Word of mouth is a communication system that exists at all times, visual and audible systems only boost this system, but it does require proximity in order to work. In this specific scenario, people were in each proximity to the event and the message. However, word of mouth will act as a constant in this evacuation scenario. The effectiveness dictated by evacuation message rate was set to 50%.

## Pedestrian Traffic Model

Using an agent was necessary to show the second part of the flowchart in which the message is spread through behavior. People are the distributors of messages and their behavior should be considered. Stadium evacuation simulation has been used previously to measure crowd dynamics. In the aforementioned 2014 study of Ladd Pebbles Stadium, the researchers compared crowd simulation models. The chosen model was behavioral, using agent-based modeling as a means of crowd simulation. This allows for a more fully formed approach to stadium emergency evacuation and verifies that simulation can be used as a valid approach to evacuation research (Aldana et al., 2014).

Through AnyLogic 8's pedestrian traffic library, the message spread can be shown in real time. Figure 4 shows how the message can be spread, based on word-of-mouth data. Using a statechart, one can base the message on a specific variable as opposed to a parameter. Therefore, a statechart was created to manipulate the message variable as opposed to manipulating the parameters to reflect a variable. The statechart uses the same understanding and contact rate as word-of-mouth communication. This validates the Bass Diffusion Model. By using actual agents, the modeling is more successful than the systems dynamics model at displaying contact information. Additionally, pedestrian modeling will eventually show the full extent of evacuation as a result of the communication systems, not just the system itself.

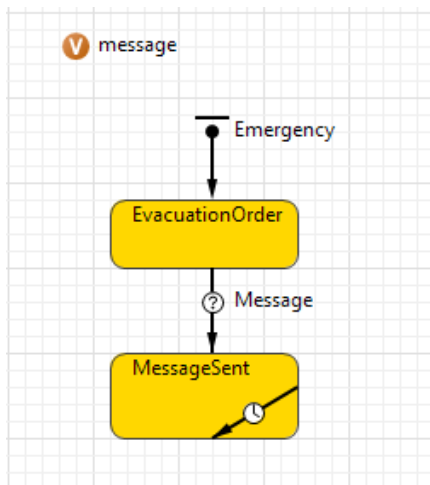


Figure 4. Pedestrian model statechart.

The physical structure of the pedestrian model is meant to reflect stadium seating so that communication rate is as close to realistic as possible. Figure 5 shows that the model uses two waiting areas with separate agents. The agents all

begin as blue, until the evacuation order is released. Then, the message is sent. Once one person has the message, they will turn red depending on contact and proximity. Error is included to account for misunderstanding due to chaos and human error.

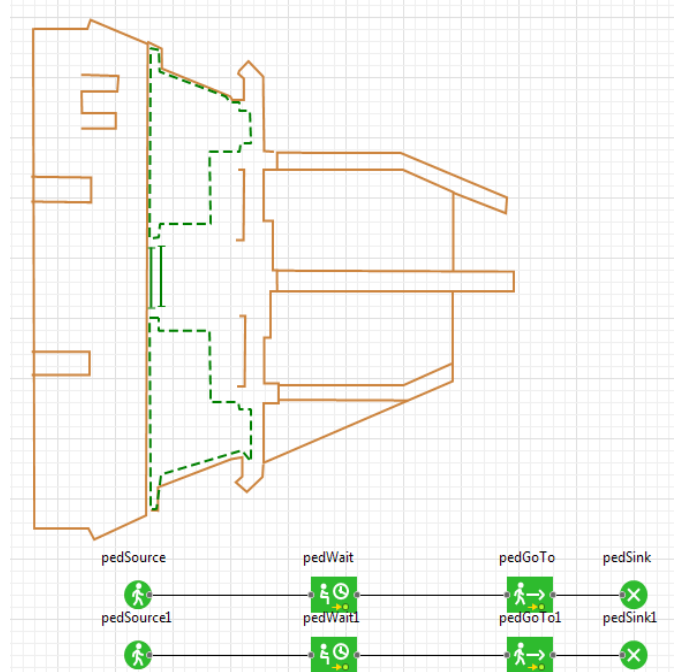


Figure 5. Final pedestrian model.

Ultimately, the final pedestrian model simulates one necessary communication method. Additional methods will require further modelling to validate and continue testing. This is something the researchers hope to pursue in the future, especially as new communication methods become popular.

## Results

Using the results from the systems dynamics model, the researchers modeled the effectiveness of different communication systems. Using word of mouth as a constant, three communication methods were compared against those initial values. In the following charts (Figures 6-10), two lines are shown. The darker line is the level of potential evacuees (the initial population) and the level of evacuees (the amount of people that successfully received the message). Acting as constant, word of mouth effectively distributed information in approximately 22 minutes. As a reminder, this is not an evacuation time, but the communication message time. As seen in Figure 6, the halfway point for the communication rate is much further than any other system.

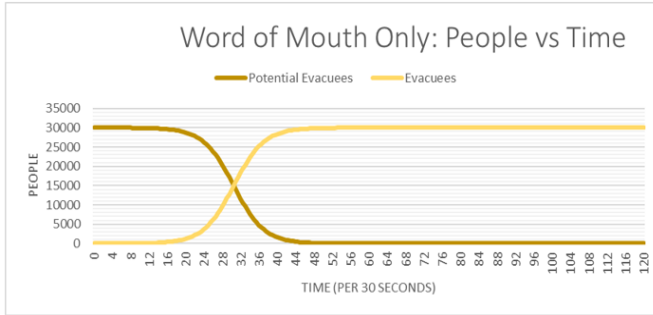


Figure 6. Word-of-mouth communication only.

Comparatively, in Figure 7, a text system in combination with word-of-mouth communication is only slightly better, taking approximately 20 minutes to spread an evacuation message. The system in question acted similarly if a single message was sent and spread amongst a stadium's fan service list. This would give a large event area the greatest chance at reaching patrons without using social media. It should be noted that this parameter will need to be studied further to establish proper manipulation and realistic boundaries.

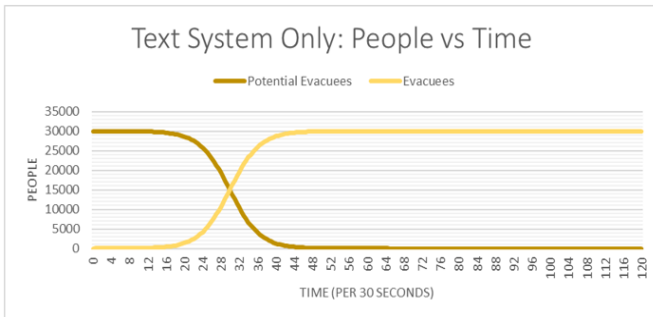


Figure 7. Text system only.

However, the systems that were more successful at issuing the message were the public announcement systems. In Figure 8, the audible public announcement system took approximately 10 minutes to communicate an evacuation message. As previously noted, these conditions were almost ideal for the public announcement system, but also assumed consistent communication being relayed at reasonable intervals. This system is necessary, but also ignores some special populations. In Figure 9, the visual system was overwhelmingly the best at successfully displaying an evacuation message. The system took approximately eight minutes to effectively communicate an evacuation message. This includes the timing and understanding delay incorporated into the data. Additionally, the authors included an example of all of the combined communication methods in Figure 10. This model took approximately nine minutes to complete, showing how multiple communication methods may negatively

affect a message spread when factoring in additional error rates. The all-methods communication scenario also reflects an inundated communication system in which a consistent error message breeds inaccuracies and response times.

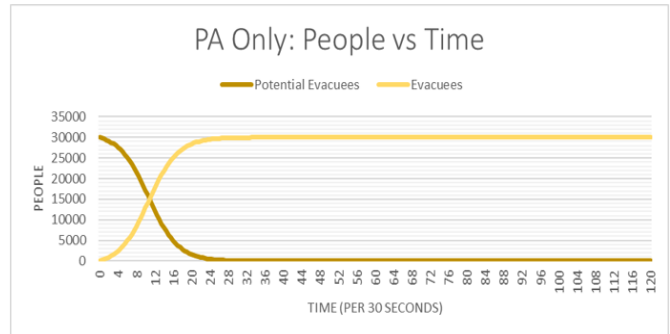


Figure 8. PA system only.

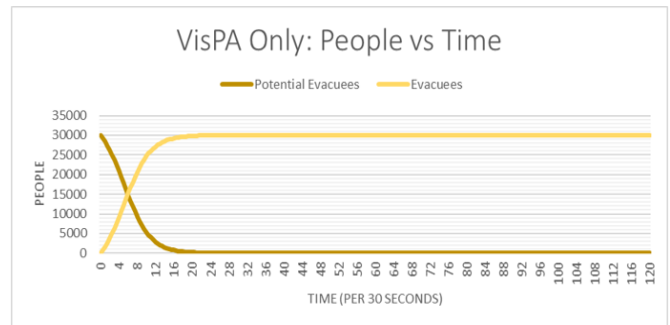


Figure 9. VisPA system only.

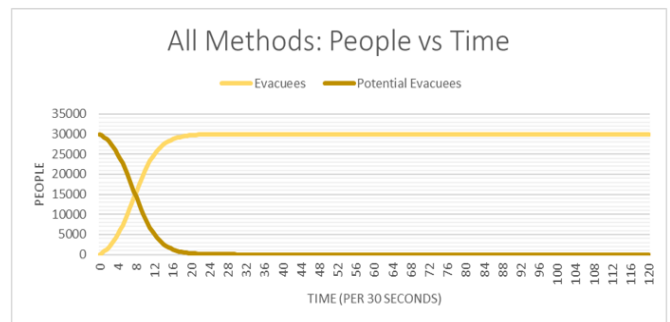


Figure 10. All communication methods.

Ultimately, the knowledge obtained from the resulting information will help improve and test emergency communication methods. This can be seen in the pedestrian model in Figure 11. The pedestrian traffic model shows that contact with the message was more realistic than a systems model. The model shows that contact rate does influence how quickly a message spreads and how word of mouth is the greatest influencer for that message. In this project, word-of-mouth communication was shown to improve communications and introduce error into any communication

system. Therefore, it is possibly the greatest asset or hindrance to response communication. The pedestrian model helps validate that theory, while also allowing further testing to occur. Though not yet in use, this pedestrian traffic model has applicability to other communication methods and provides a more realistic understanding of how communication would occur in an actual emergency, as opposed to a hypothetical one. The model above shows how contact rate affects method spread as the blue dots change to red when the message is effectively spread.

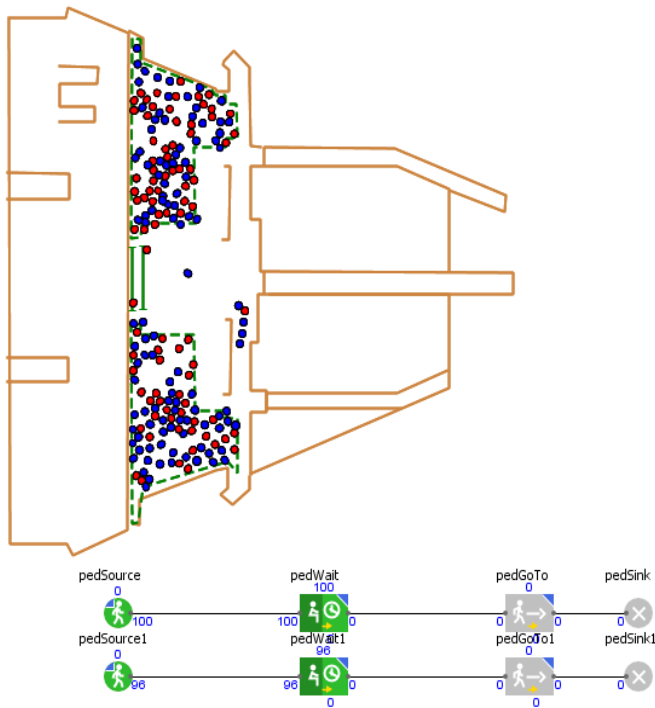


Figure 11. Pedestrian traffic model.

## Discussion

Though all the communication systems are shown differently, exploring communication contact rate as a key to effectiveness will need to be considered in subsequent trials. For example, text messaging systems have the potential to be the most effective evacuation communication method, as it can reach most people, and is still accessible to those with disabilities and those not in the main area of the stadium where the visual and audible public announcement systems are used. However, there is a possible issue in that the number of patrons on their phones could overload the cellular signal and the text message does not go through, undoing all of the benefits. Additionally, audible public announcements are the next most effective evacuation communication method. This method is also capable of reaching all patrons, not

only those in the main areas. However, the consideration of those with special needs should occur as this method does hinder the deaf or hard of hearing. Also, audible public announcements need to be used cautiously, as aggressively loud and commanding announcements could increase panic and induce anxiety. Testing will follow to see how valid this system is to an actual evacuation. Finally, visual public announcement systems are the least effective of all three methods, but the best in terms of understanding. This method can only reach patrons in the main areas and those who can read, observe, and understand what is announced. It does not take blind patrons into consideration. However, if the visual public announcement is flashed on and off, it could draw more attention to the message. Additionally, more information could be given via visual public announcement systems, information which could be more easily updated.

## Conclusions

Though examining the results appears to suggest that the visual public announcement system was the most effective model, this was only in regards to one factor. It only reaches a certain number of patrons at one time. Therefore, all methods of communication should use three reliable systems to issue an evacuation message. However, the message would need to be uniform and accurate for this model to work. While it is not feasible for all three methods to be consistently running at the same time, each situation would require a specific combination of the three. This question will require more consistent testing to deduce the correct order and should be used in combination with the pedestrian model to achieve the most realistic results. As testing continues, this same question will apply to the pedestrian model and contact rate. Additionally, incorporating social media as a communication method will be considered moving forward. However, this method has more complex intricacies, with obsolescence of equipment being a distinct possibility.

Notably, many of these systems can be altered to ensure that they perform more effectively than their standards. These differences may mean that one system is more effective than another at a certain venue, event, or scenario. These alterations continue to affect word-of-mouth communication; thus, all three methods should be considered in addition to this method. Word-of-mouth communication continues to be the communication at the base of each method, deciding effectiveness and understanding of evacuation. The faster a message is understood, the better the outcome of an evacuation. By assisting individual security, the venue is better prepared for an emergency. The faster they respond, the more lives saved. Therefore, communicating proper responses to patrons is the difference between life and death.

---

## References

- Aldana, N., Fox, C., Diehl, E., & Dimitoglou, G. (2014). A study of stadium exit design on evacuation performance. *Proceedings of the 27th International Conference on Computer Applications in Industry and Engineering*. Cary, NC: International Society for Computers and Their Applications.
- Alertus Technologies. (2018). *Mobile notification*. Retrieved from <https://www.alertus.com/personal/>
- AT&T Stadium operations manual. (2018). Retrieved from <https://attstadium.com/sites/default/files/dc-content-files/City%20of%20Arlington%20Policies.pdf>
- Bankers Life Fieldhouse. (2018). *Fan guide*. Retrieved from <http://www.bankerslifefieldhouse.com/arena-information/fan-guide/>
- Broom, G. M., Sha, B. L., Seshadrinathan, S., Center, A. H., & Cutlip, S. M. (2013). *Cutlip and Center's effective public relations*. (11th ed.). Upper Saddle River, NJ: Pearson.
- Burke, K. (2016). *73 texting statistics that answer all your questions*. Retrieved from <https://www.textrequest.com/blog/texting-statistics-answer-questions/>
- Centers for Disease Control and Prevention [CDC]. (2018). *Emergency preparedness and response: Social media*. Retrieved from <https://emergency.cdc.gov/socialmedia/index.asp>
- Department of Homeland Security [DHS]. (2008). *Evacuation planning guide for stadiums*. Retrieved from <https://www.dhs.gov/sites/default/files/publications/evacuation-planning-guide-stadiums-508.pdf>
- Department of Homeland Security [DHS]. (2014). *Communicating in an emergency. Federal Emergency Management Agency*. Retrieved from [https://training.fema.gov/emweb/is/is242b/student%20manual/sm\\_03.pdf](https://training.fema.gov/emweb/is/is242b/student%20manual/sm_03.pdf)
- Ellis, R., Fantz, A., Karimi, F., & McLoughlin, E. C. (2016). Orlando shooting: 49 killed, shooter pledged ISIS allegiance. *CNN*. Retrieved from <https://www.cnn.com/2016/06/12/us/orlando-nightclub-shooting/index.html>
- Mehrabian, A. (1971). *Silent messages*. Belmont, CA: Wadsworth.
- Mileti, D. S., & Sorensen, J. H. (1990). *Communication of emergency public warnings: A social science perspective and state-of-the-art assessment*. Washington, DC: FEMA. Retrieved from <https://doi:10.2172/6137387>
- Norton, J. A., & Bass, F. M. (1987). A diffusion theory model of adoption and substitution for successive generations of high-technology products. *Management Science*, 33(9), 1-19.
- Proulx, G. (1995). Evacuation time and movement in apartment buildings. *Fire Safety Journal*, 24(3), 229-246.

Retrieved from [https://doi.org/10.1016/0379-7112\(95\)00023-M](https://doi.org/10.1016/0379-7112(95)00023-M)

Towson University. (2018). *Emergencies*. Retrieved from <https://www.towson.edu/publicsafety/emergencies/>

## Biographies

**KATHERINE REICHART** is a graduate student in Homeland Security in the Computer Information Technology program at Purdue University. Her previous degree is in professional writing, also from Purdue University. Additionally, she is a member of the Purdue Homeland Security Institute. She has been involved in several research projects in the institute. Additionally, she is an assistant editor on several books in progress concerning those research topics. Her research will continue to focus on communication and reporting methods of large event security. Katherine Reichart may be reached at [kreichar@purdue.edu](mailto:kreichar@purdue.edu)

**ANNA LARSON** works for General Electric in Detroit, MI. She earned her BS in Computer Information Technology from Purdue University and MS in Computer and Information Technology, 2018, from her alma mater. Her interests include disaster network communication and cyberforensics. Anna Larson may be reached at [lar-sona@purdue.edu](mailto:larsona@purdue.edu)

**KRISTAL SMITH** works for Blue Horseshoe in Boulder, CO. She recently graduated from Purdue University with her BS in Computer and Information Technology. While there, she researched and participated in projects regarding emergency preparedness. Kristal Smith may be reached at [smit2265@purdue.edu](mailto:smit2265@purdue.edu)

**J. ERIC DIETZ**, PE, graduated in 1984 with a BS and again in 1986 with an MS in chemical engineering both from the Rose-Hulman Institute of Technology. He earned his PhD in chemical engineering in 1994 from Purdue University, where he is now a professor. In 2004, he retired as a Lieutenant Colonel from the U.S. Army. Thus, his research interests include optimization of emergency response, homeland security and defense, energy security, and engaging veterans in higher education. Dr. Dietz may be reached at [jedietz@purdue.edu](mailto:jedietz@purdue.edu)

# DEVELOPING AN OPEN SOURCE, INEXPENSIVE, LARGE-SCALE POLAR CONFIGURATION 3D PRINTER

Sourabh Prashant Deshpande, University of Cincinnati; Shrinivas Kulkarni, Michigan Technological University; Sid Shah, Michigan Technological University; John Irwin, Michigan Technological University

## Abstract

Various 3D printer configurations, such as Cartesian printers, operate similarly to a CNC machining center and Delta printers that have a stationary build platform with the use of three motors located on pillars controlling the end effector location. A less popular configuration is a Polar system, which utilizes a rotating table, a Z translation controlled by a linear actuator located beyond the edge of the rotating table, and a horizontal arm connected to the Z-axis that translates the end effector along the center axis. The Polar 3D printer configuration, being the simplest, was chosen in order to scale up to build and test a low-cost large-scale 3D printer with a build envelope of 1.83m x 1.83m x 1.53m (6ft x 6ft x 5ft).

This open source hardware 3D printer (OSALS-Polar) can be produced for approximately \$5,000 for materials, assuming that labor is provided by the user. To 3D print a part, any CAD software is used to output a stereo lithography (.stl) file, open source slicing software (Cura) to generate the G-code file, and open source software (Franklin) to operate the 3D printer. Testing the 3D printer requires calibration of the three axes to produce the desired positioning of the Theta-axis rotation, R-axis horizontal arm translation, and Z-axis vertical translation with the inputs into the Franklin software. Also, the system is set to start at a zero location, according to distances set from the end-stop limit switches. The final testing of the OSALS-Polar produced small extruded parts, although the accuracy and scaling up to larger parts not accomplished during this study. Future testing may encounter limitations in the size of prints, due to material cooling at various rates, causing warpage.

3D printing technology has become quite common, and increasingly applications for direct digital manufacturing are being implemented. RepRap (self-replicating machines) 3D printers (Sells, Bailard, Smith, Bowyer, & Olliver, 2010; Gibb, 2014) are open source 3D printer designs available for anyone to build. According to Wittbrodt et al. (2013), the cost of an open source 3D printer used for printing household components, such as a pierogi mold or paper towel holder, can be recuperated within a year or two if a reasonably fair number of household items are printed using the 3D printer (Wittbrodt et al. 2013; Wittbrodt, 2014). The

3D printer build envelope (printer platform times the printing height capability) can be a limitation of direct digital manufacturing, if the part exceeds this build envelope. Common desktop 3D printers have a build envelope of 203 mm (8 in.), length x 203 mm (8 in.), and width x 153 mm (6 in.) height. Larger-scale 3D printers, ranging from 5 to 10 times the size of the common desktop 3D printers, are typically very expensive to produce.

Methods of joining 3D-printed parts via acetone have been successful in producing parts such as wind turbine blades (Deshpande, Rao, Pradhan, & Irwin, 2016), although this method requires several manufacturing steps and can decrease overall part accuracy. The goal of the OSALS-Polar is to manufacture larger 3D-printed parts (such as wind turbine blades or propeller blades) that can be printed in a single setup without needing to be joined together. Wind turbine blades can operate at potentially high RPMs, and any structural concerns lead directly to safety concerns, making it advantageous to 3D print as one continuous part. To overcome size restrictions of desktop 3D printers, the OSALS-Polar can cost under \$5,000 for materials, assuming the user provides the labor. In this paper, the authors describe the assembly and testing of the OSALS-Polar with a build envelope of 1.83m x 1.83m x 1.53m (6ft x 6ft x 5ft). The build instructions for this system are also described here. The open source software used to create the slice file was Cura; to operate OSALS-Polar, the open source software Franklin was used.

## Introduction

Currently, there are many different 3D printer configurations, such as the X, Y, Z Cartesian coordinate 3D printers that operate similar to a CNC machining center, or the Delta, which has a stationary build platform with the extruder operated by three vertical axis translations located on a triangular base. A less popular method for controlling the movement of the axes is a Polar system. Figure 1 shows a benchmark 3D printer produced by Polar3D and its main components. This particular 3D printer has a build envelope of 203mm (8 in.) diameter x 153 mm (6 in.) height. The Polar 3D system was used as a datum design to develop the initial 9:1 OSALS-Polar CAD design and a set of manufacturing drawings. The Polar 3D system utilizes a rotating table (Theta-axis) with a horizontal arm (R-axis) that trans-

lates the extruder along a single axis to and from the center of the printing surface. The vertical (Z-axis) translation in this system is controlled by a linear power screw and guides located beyond the edge of the rotating surface. This Polar style 3D printer was determined to be the simplest design, when compared to the Cartesian and Delta styles, to up-scale.

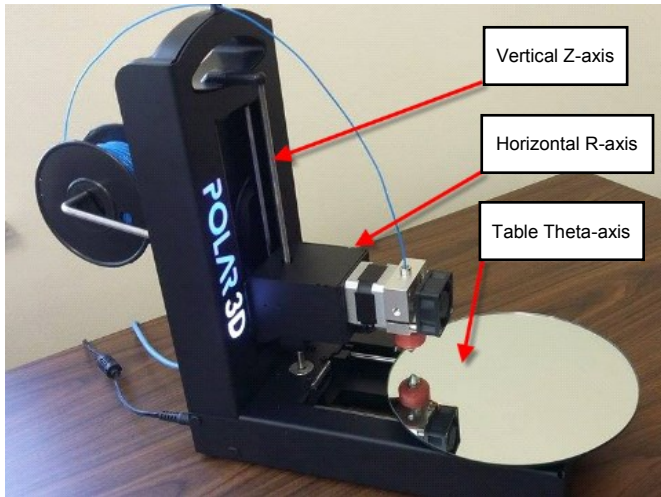


Figure 1. Polar3D printer (About, 2014). Reprinted with permission.

## Review of Related 3D Printing Systems

Rapid developments in the field of 3D printing technology have ranged in applications from prototyping to direct digital manufacturing. Berman (2012) compares the revolution of 3D printing technology with the digital books revolution and foresees its use in several promising applications such as medicine and construction. Gebler, Uiterkamp, & Visser (2014) discussed 3D printing technology in terms of sustainability and asserted that this technology will lower resource demands, energy use, and carbon dioxide emissions over the entire lifecycle. According to Wohlers (2013), use of additive manufacturing technology for direct part production has increased by more than 25% in the last few years.

Significant efforts are underway to build a large-scale 3D printing system to manufacture large-scale industrial components. Barnett and Gosselin (2013) designed a novel large-scale 3D printer with a cable-suspended mechanism and a full scaffolding solution. However, most of the research on large-scale 3D printers is based on Cartesian and Delta system configurations. A typical Polar 3D printing system has a higher build volume with fewer components, when compared with other types (Yusuf, 2015). A true Polar 3D printer has a rotating build plate (Theta-axis) with the vertical

arm (Z-axis) and the extruder placed on the horizontal arm (R-axis). Any point on a flat plane can be defined by knowing its angle theta, pole vertical location, and a measure of radius from an axis through the given pole (Horn & Hausman, 2017).

A Cincinnati-based Polar 3D technology company uses fused-filament fabrication technology for a Polar 3D printer having 203.2 mm (8 in.) diameter, 158.75 mm (6.25 in.) height with connectivity features such as Wi-Fi, Ethernet, and USB (About, 2014). R-360 is an open source Polar 3D printer with 210 mm (8.26 in.) disc x 200 mm (7.87 in.), with a total printing volume of 6,927,000 mm<sup>3</sup> (422.71 in<sup>3</sup>). It uses PLA or ABS as the printing material and has a maximum printing speed of 150 mm/s, along with features such as cloud slicing (Replicator, 2013; Farcas, 2016). Another Polar 3D printer with 304.8 mm (12 in.) diameter and 150 mm (5.9 in.) height has some major features, which include the use of four extruders and Decapede electronics for driving 10 stepper motors (Anderson, 2014). The PiMaker 3D printer also uses the Polar system, with 279.4 mm (11 in.) diameter and 203.2 mm (8 in.) height with an overall volume of over 10,650,000 mm<sup>3</sup> (650 in<sup>3</sup>) (Steele, 2016). 3D printers have also been made on modest budgets, such as a senior project by Hoy (2016), who developed a Polar 3D printer having 177.8 mm (7 in.) diameter that uses PLA filament.

## Polar 3D Printer Design

The OSALS-Polar is designed, manufactured, and assembled by configuring the Theta-axis, Z-axis, and R-axis, respectively. Engineering requirements are mapped using QFD methodology. The material for the table surface, vertical and horizontal supports, and the rotation drive system are selected using the decision matrix method. Accordingly, the major items selected are a tubular steel structure, circular glass printing plate, circular steel plate table, extruded aluminum horizontal arm, and stepper motors for axis motion. PFMEA is carried out to identify and reduce the potential failures in the system. The circular glass printing plate has the highest RPN value for which the use of glass edge guards is recommended to avoid breakage and/or injury.

The main frame is made up of steel I-beams and steel tubular sections welded together to manufacture the table frame. Then, pivot tabs welded to both the bottom frame and table frame provide assembly alignment and leveling capabilities. The steel table has a center shaft that is placed in the table frame center bearing after proper lubrication of all the parts. Figure 2 shows the assembly, after fixing the table roller bearings, center bearing, and the casters to the frame.

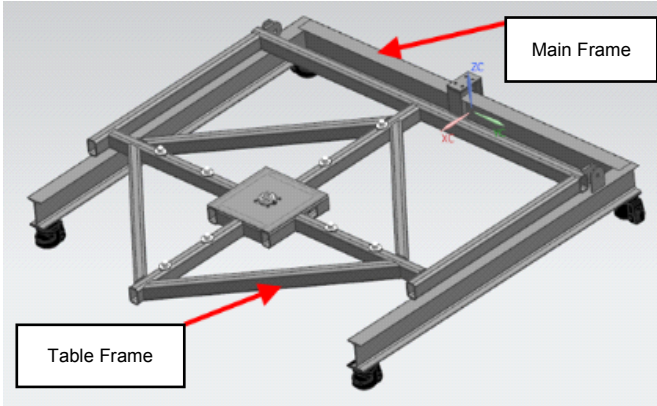


Figure 2. Frame assembly.

The main power transmission component for the Theta-axis rotating table is a stepper motor turning a spur gear driving an internal ring gear. The internal ring gear is manufactured by machining 10 segments that together form the 1,587.5 mm (62.5 in.) pitch diameter internal ring gear. The pinion gear is mounted to a NEMA 34-stepper motor that drives the ring gear. Despite several challenges introduced in the system, such as improper mating of the ring gear sections, providing larger clearance holes on the ring gear segment enabled smoother motion. The use of flexible pads in stepper motor mounting also helped to minimize the inaccuracies in the gear alignment (Pradhan, Irwin, Siddegowda, & Harsha, 2016). The internal gear drive mechanism shown in Figure 3 facilitates improved rotary motion of the table over the originally designed center worm-gear configuration that had many backlash issues.

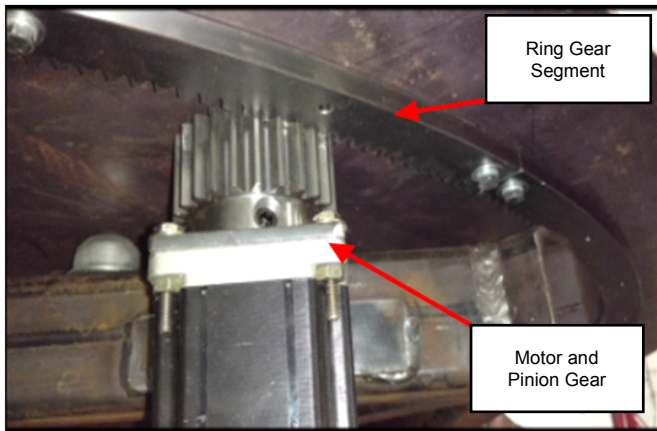


Figure 3. Theta-axis drive mechanism.

Figure 4 shows how the vertical Z-axis beam is bolted securely to the main frame, which supports the horizontal arm R-axis and the extruder. The Z-axis mounting bracket is used to attach the R-axis motor, accommodate the acme nut, and also fix the R-axis horizontal arm in place. The acme

rod is coupled to the Z-axis motor shaft with a straight coupling with no gearing or reduction. Two guide rails are designed for the travel of the Z-axis. FEA was carried out on the system, after which support brackets were added from the guide rails to the vertical Z-axis beam accordingly in order to avoid the deflection of the extruder through its travel.

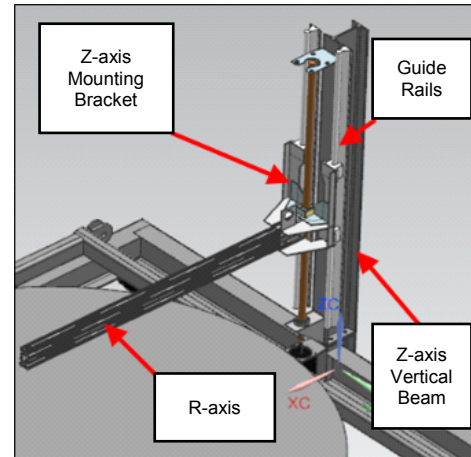


Figure 4. Vertical Z-axis.

The R-axis carriage wheels are locked into grooves on the R-axis horizontal arm, while a timing belt drive system shown in Figure 5 controls the translating motion. Figure 6 shows how the extruder, extruder motor, and hot end are integrated into the carriage assembly. The extruder, hot end bracket, and spool holder were manufactured using 3D printing.

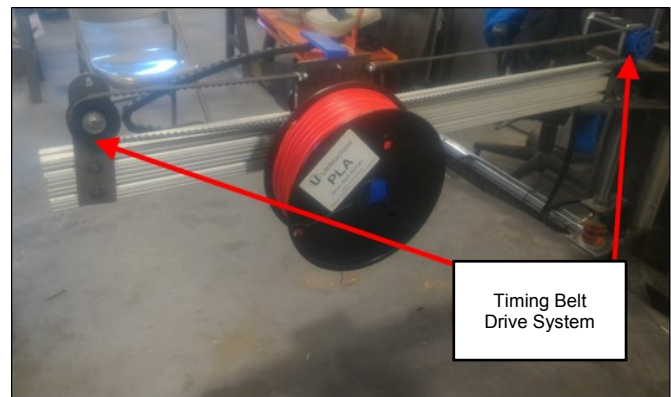


Figure 5. Drive system R-axis.

## Polar 3D Printer Controls

An electrical box houses the circuitry and auxiliary electronic components. Figure 7 shows how the unit is fixed to the back side of the vertical arm of the OSALS-Polar.

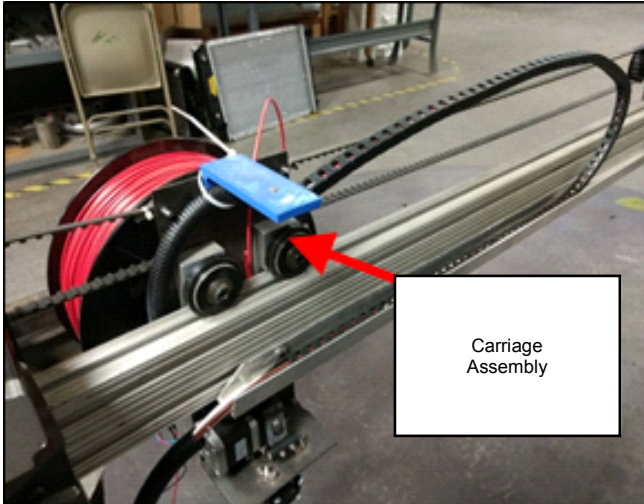


Figure 6. Carriage assembly R-axis.

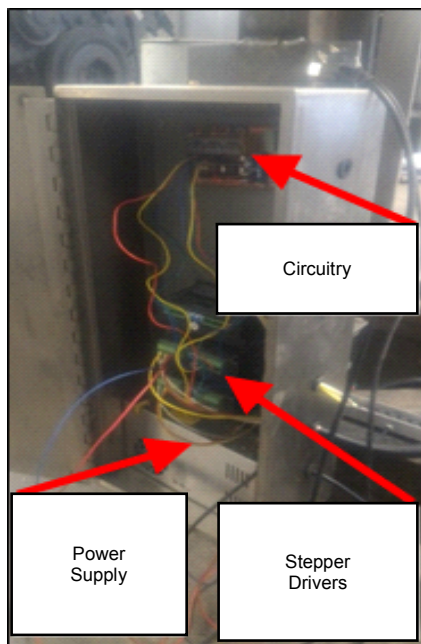


Figure 7. Electrical box layout.

The circuitry includes RAMPS 1.4 controller and a Beaglebone connected with a bridge board. All of the electrical components were integrated into the RAMPS 1.4 controller. Figure 8 shows the wiring diagram for the RAMPS 1.4. To adhere to the “affordable” goal of the OSALS-Polar, stepper motors were used rather than servo motors to facilitate the movement of the three axes. The motion of the axes is enabled by three DQ542MA micro-step drivers. Each stepper driver is controlled by Franklin firmware through a Pololu A4988 stepper driver carrier mounted on the RAMPS 1.4 board. The steps per revolution and the input current for

each axis motor were set using the DIP switches on the micro-step drivers. The DIP switches were set with 1, 3, 6, and 8 in the “on” position and 2, 4, 5, and 7 in the “off” position. Switches 1, 2, and 3 were set to the on, off, and on positions, respectively, to match the motor current (amperes) of 1.91 at peak and 1.36 RMS. Switch 4 was set to the off position so that standstill current would be half of the selected dynamic current. The Micro step resolution was set to 6,400 by setting switches 5, 6, 7, and 8 to the off, on, off, and on positions, respectively.

The RAMPS 1.4 also controls the extruder assembly, which consists of an extruder motor, a hot end to melt the filament, a cooling fan to control the outer temperature of the hot end, and a thermistor to indicate the hot end temperature. Figure 8 shows the wiring diagram for RAMPS 1.4. A Pololu A4988 stepper driver carrier was also used to control the extruder motor; however, for this motor, no micro-step driver was needed. The stepper drivers get power from a 36V power supply. Power for the extruder motor, fan, and the hot end are provided through the RAMPS 1.4. Since no heated bed is used in this printer, a 12V power supply is connected to the heated bed port to externally power the RAMPS 1.4 and direct that power to the extruder motor, hot end, and fan.

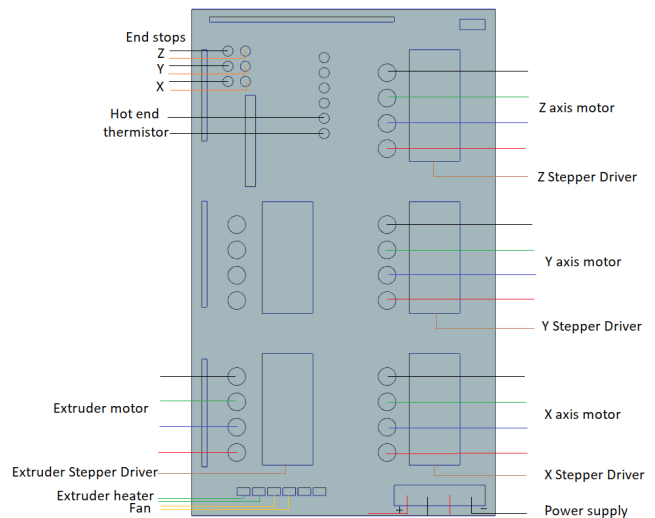


Figure 8. Ramps 1.4 wiring diagram.

Figure 9 shows how mechanical end stops on each axis allow the printer to start from a reference point. End stops can be mounted on the maximum or minimum position of an axis. Since the zero for this printer is set at the center of the rotating table, the end stops are located at the maximum position for the R-axis and Z-axis. Thus, the end stops are connected to the pins corresponding to the maximum position on the RAMPS 1.4 board.

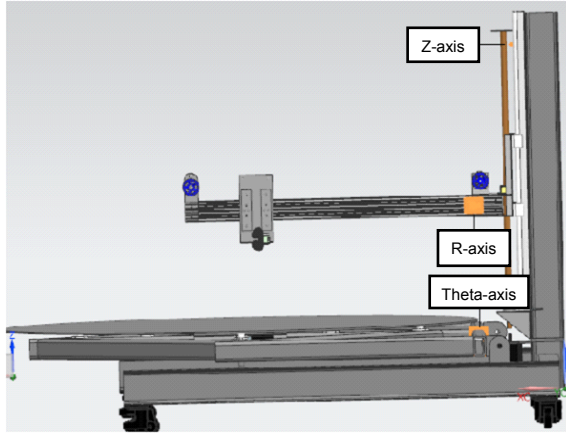


Figure 9. End stop mounting.

The RAMPS 1.4 circuit board is connected to a Beaglebone loaded with the Franklin firmware. The OSALS-Polar can be operated by connecting to the Beaglebone using an Ethernet cable from any host computer. Figure 10 shows how the Franklin software is accessed through a Web address in order to pull up a user interface. The printer configuration setup is completed on this user interface. The various attributes of the Franklin firmware are then mapped with the pins on RAMPS 1.4, using the pin assignments shown in Table 1.

Figure 11 shows the flow of signals from Beaglebone to the axis motors and the extruder assembly. This figure also shows a schematic diagram of the various components controlled by the Franklin firmware.

Table 1. Pin mapping.

Axis Motors						Extruder Assembly	
R Axis		Theta Axis		Z Axis			
X_STEP_PIN	54	Y_STEP_PIN	60	Z_STEP_PIN	46	E_STEP_PIN	26
X_DIR_PIN	55	Y_DIR_PIN	61	Z_DIR_PIN	48	E_DIR_PIN	28
X_ENABLE_PIN	38	Y_ENABLE_PIN	56	Z_ENABLE_PIN	62	E_ENABLE_PIN	24
X_MIN_PIN	3	Y_MIN_PIN	14	Z_MIN_PIN	18	FAN_PIN	9
X_MAX_PIN	2	Y_MAX_PIN	15	Z_MAX_PIN	19	HEATER_PIN	10
						THERMISTOR	13

<b>r</b>				
Step	D54 (A0)	<input checked="" type="checkbox"/> Valid	<input type="checkbox"/> Inverted	Set
Dir	D55 (A1)	<input checked="" type="checkbox"/> Valid	<input type="checkbox"/> Inverted	Set
Enable	D38	<input checked="" type="checkbox"/> Valid	<input type="checkbox"/> Inverted	Set
Min Limit	D3	<input type="checkbox"/> Valid	<input type="checkbox"/> Inverted	Set
Max Limit	D2	<input checked="" type="checkbox"/> Valid	<input type="checkbox"/> Inverted	Set
<b>θ</b>				
Step	D60 (A6)	<input checked="" type="checkbox"/> Valid	<input type="checkbox"/> Inverted	Set
Dir	D61 (A7)	<input checked="" type="checkbox"/> Valid	<input type="checkbox"/> Inverted	Set
Enable	D56 (A2)	<input checked="" type="checkbox"/> Valid	<input type="checkbox"/> Inverted	Set
Min Limit	D14	<input checked="" type="checkbox"/> Valid	<input type="checkbox"/> Inverted	Set
Max Limit	D15	<input type="checkbox"/> Valid	<input type="checkbox"/> Inverted	Set
<b>z</b>				
Step	D46	<input checked="" type="checkbox"/> Valid	<input type="checkbox"/> Inverted	Set
Dir	D48	<input checked="" type="checkbox"/> Valid	<input checked="" type="checkbox"/> Inverted	Set
Enable	D62 (A8)	<input checked="" type="checkbox"/> Valid	<input type="checkbox"/> Inverted	Set
Min Limit	D18	<input type="checkbox"/> Valid	<input type="checkbox"/> Inverted	Set
Max Limit	D19	<input checked="" type="checkbox"/> Valid	<input type="checkbox"/> Inverted	Set
<b>extruder 0</b>				
Step	D26	<input checked="" type="checkbox"/> Valid	<input type="checkbox"/> Inverted	Set
Dir	D28	<input checked="" type="checkbox"/> Valid	<input checked="" type="checkbox"/> Inverted	Set
Enable	D24	<input checked="" type="checkbox"/> Valid	<input checked="" type="checkbox"/> Inverted	Set
Min Limit	D0	<input type="checkbox"/> Valid	<input type="checkbox"/> Inverted	Set
Max Limit	D0	<input type="checkbox"/> Valid	<input type="checkbox"/> Inverted	Set

Figure 10. Franklin software settings.

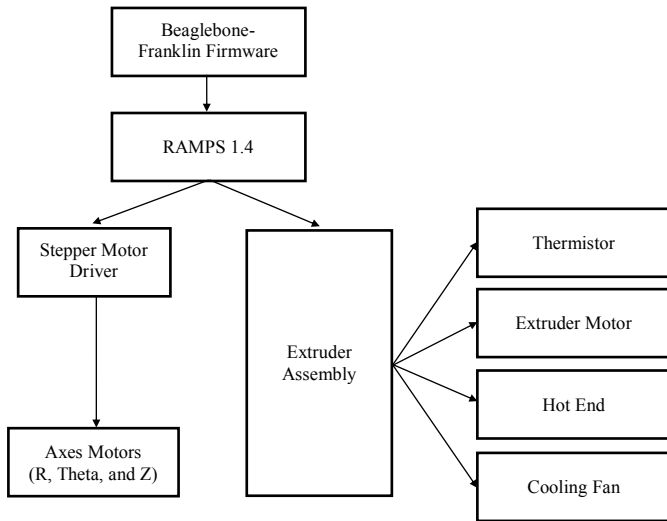


Figure 11. Electrical component diagram.

## OSALS-Polar Operation Methods

3D printing is carried out by using CAD to output a stereo lithography (.stl) file, slicing software (Cura) to generate the G-code file, and Franklin to operate the OSALS-Polar. Siemens PLM NX CAD software can be used to insert the formulas and expressions for the parametric modeling intent (Irwin, 2013) and to export it in an .stl file format. The .stl file is loaded in Cura and prepared for 3D printing. Some overhang parts shallower than 45° may require the use of support material (France, 2013). The machine type in Cura is set to Custom FDM printer with PLA material. The polymer filament used can be either polylactic acid (PLA) or acrylonitrile butadiene styrene (ABS), converting it into a physical object by depositing it in thin, sequential layers. PLA is used in this printer rather than ABS because of its lower melting temperature and superior adhesion to the glass substrate. The layer height, shell thickness, fill density, print speed, retraction distance, and print temperature are some of the parameters that are set and calibrated as per the print material and output quality requirements. The slicing software converts this .stl file into consecutive thin layers to generate G-code (Cano, 2015). The commonly used open source slicing software includes Cura and Slic3r Repetier. The Polar 3D company provides cloud services, where the CAD model can be converted to slices online and then downloaded to run the code.

Franklin is a Web-based 3D control system to regulate the machining process parameters with any internet-connected device. The main function of this software, shown in Figure 12, is to drive the hardware systems by integrating with the slicer software program (Wijnen, Anzalone, Haselhuhn, Sanders, & Pearce, 2016).

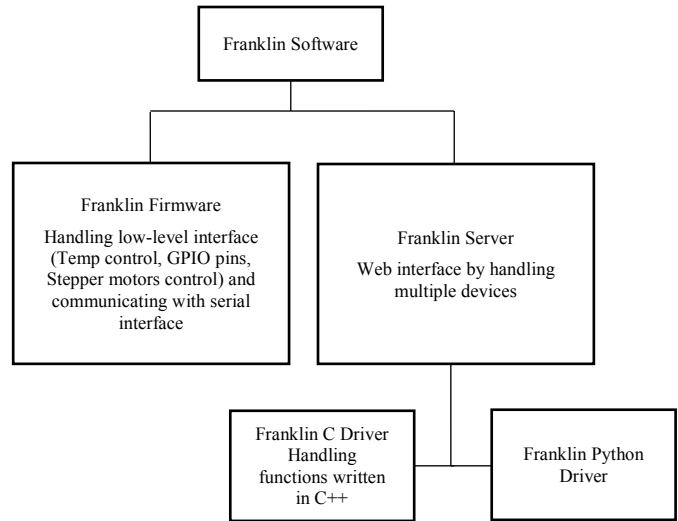


Figure 12. Franklin software.

The software aims to be more powerful and user-friendly by having improved robustness, system reliability (error checking), and a powerful scripted interface to smoothly run the G-code specifically for the large-scale 3D printing and sophisticated scientific/medical designs. The main communication interfaces for this software include:

1. Web socket connection to the browser or script client (JSON array)
2. Franklin Server and Franklin Python driver (JSON array)
3. Franklin Python driver and Franklin C driver (binary packet)
4. Franklin C driver and Franklin interface (physical serial line)

Calibrating the printer is important in order to ensure the accuracy of positioning of the nozzle and distance traveled along the respective axes. Calibration includes choosing the right amount of current and micro-stepping for the three axes. It is also important to calibrate the absolute zero position for the three axes. The dip switches on the motor drivers are used to set the amount of current for each motor, and were set to half current for this system. Micro-stepping is decided based on the torque requirements and the necessary motion accuracy. The motor stepper drivers were set to 800 pulses per revolution for the Z-axis and 6,400 pulses per revolution for the Theta- and R-axes. Micro-steps are also set using the dip switches on the stepper motor drivers. The number of revolutions are calculated to enter Franklin software based on the 200-step-per-revolution motors. Equation 1 was used to calculate the new steps for the R- and Z-axes (Pearce, 2014). For the Theta-axis, the distances are replaced with the desired and actual angles, which can be calibrated by the same method.

$$\frac{\text{Steps in firmware} \times \text{Desired distance}}{\text{Actual distance traveled during testing}} \quad (1)$$

The Z-axis travel was calculated as 2.54 mm/rev by converting the 0.100-inch pitch for the 1"-10-threads-per-inch acme screw to metric units. Finally, the Theta-axis travel has 500 teeth on the internal ring gear and 24 teeth on the pinion; thus, from Equation 2, the table rotates 17.28 degrees per motor revolution.

$$\text{Theta-axis travel (degrees/rev)} = 360 \left( \frac{\# \text{ teeth ring gear}}{\# \text{ teeth pinion}} \right) \quad (2)$$

Finally, Table 2 shows that the Franklin software requires an entry for steps/mm or steps/degree for each motor, based on the motor stepper driver pulses per revolution. The number of micro-step pulses per revolution are divided by the travel per revolution for each axis, as given by Equation 3:

$$\frac{\text{Franklin Coupling setting (steps/mm)}}{\text{Micro steps/Axis travel (mm/rev or degrees/rev)}} \quad (3)$$

To finely tune the OSALS-Polar, Equation 4 was used to calculate a calibrated number of steps for the R- and Z-axes (Pierce, 2014). For the Theta-axis, the distances were replaced with the desired and actual angles, which can be calibrated by the same method.

$$\frac{\text{Calibrated Franklin Coupling setting (steps/mm)}}{\text{Original steps/mm in Franklin} \times \frac{\text{Desired distance}}{\text{Actual distance traveled during testing}}} \quad (4)$$

Absolute zero was calibrated by first marking the center on the rotating table. Reference positions are set by homing the machine using the Franklin interface. The limit switch positions in Franklin are changed to specify the distance between reference points and absolute zero. For the R-axis, a fixed end stop was placed on the horizontal arm bracket and the switch position calibrated to 820 mm in Franklin. Similarly, for setting the Z-axis switch, position can be calibrated by using a paper gage (0.1 mm thickness) on at least four equiangular points of the circular base. Currently, the Z-axis switch position was set to 96 mm. For the Theta-axis, the reference point used was zero. The movement accuracy

for the Z- and R-axes were tested by using dial indicators to validate that the software could manually jog the axis the desired distances. For the theta axis, one complete revolution is measured when the axis is jogged 360°. When the OSALS-Polar is successfully calibrated, it is ready to create a 3D-printed part.

## Results of 3D Printing

By manually jogging the Z- and R-axes in the Franklin interface, measurements taken with a 12-inch travel dial indicator length gage indicate precision from zero to 1 mm. For the Theta-axis, a 360° rotation varies within 1°, indicated by an alignment mark on the table and stationary frame. Causes for variations in travel of the R- and Theta-axes are due to the timing belt and gear as well as the ring gear and pinion interfaces. Adjusting the Theta-axis motor too tightly against the internal ring gear will cause the gear teeth to bind and stop rotating. So, the looser fit in the mating of the gear teeth causes some backlash. The R-axis belt, having a 9.525 mm pitch, yields a travel of 171.45 mm per motor revolution, so a finer pitch belt will improve the R-axis precision. The Z-axis accuracy is due to the tight connection of the motor shaft to the acme screw, eliminating backlash and slippage.

Figure 13 shows various geometries for testing the OSALS-Polar, which include a cylinder and cuboid. Initial test results for the 50x50x5 mm-high part were unsuccessful in achieving accurate and smooth surface results. The printing time was estimated at 15 minutes, which was approximately the time for the trial test. Figures 14 and 15 show the actual printed part and the top surface, which is angled lower towards the center of the printing surface. This result was consistent with all sample test prints and was likely caused by the R-axis planar misalignment with the Theta-axis table surface. The R-axis arm deflected slightly downward, as the extruder mechanism reached the end of its travel at the center of the table. The deflection of the R-axis arm caused the extruder nozzle to drag over the surface of the part as the Theta-axis rotated and the R-axis translated, thereby forming a buildup of plastic on the leading edge of the printed path.

Table 2. Step values set in Franklin.

Axis	Steps	Number of teeth	Pitch type	Pitch (inches)	Pitch per revolution	Micro-steps	Actual Steps
r	200	18	Linear	0.375	171.45 mm/rev	6400	37.32 /mm
theta	200	Pinion 24	Circular	-	17.28 degrees/rev	6400	370.37/degree
		Ring Gear 500					
z	200	-	Acme	0.1	2.54 mm/rev	800	314.96/mm

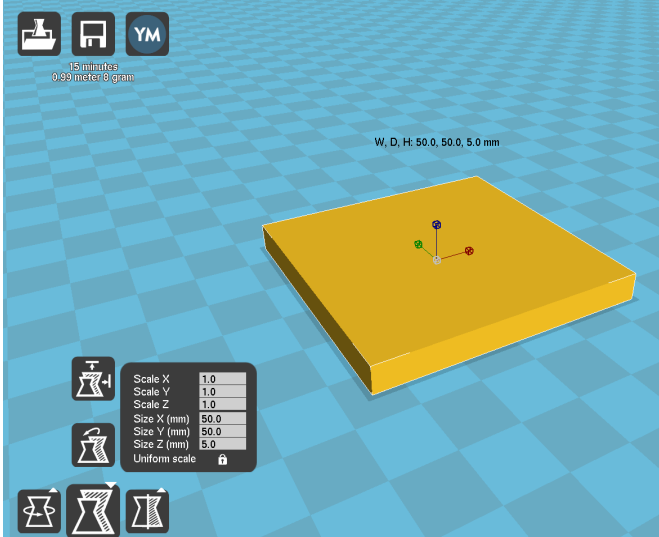


Figure 13. Cura file, 50x50x5mm high.

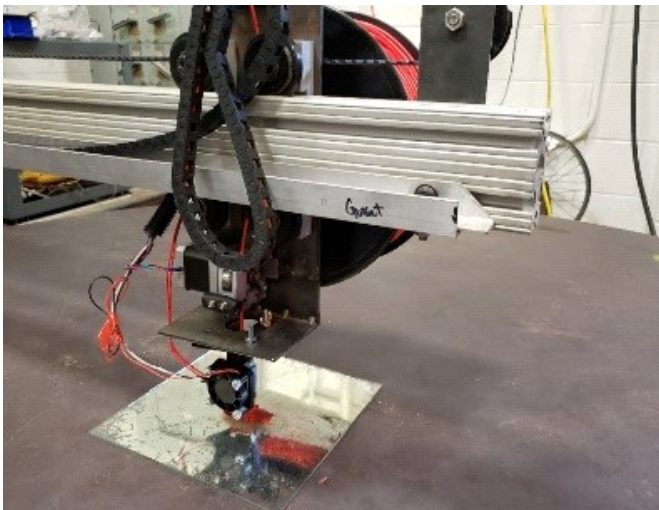


Figure 14. Initial test part, 50x50x5mm high.



Figure 15. Part accuracy.

The results of the 50x50x5 mm-high part were difficult to measure with precise accuracy, due to the uneven surface. Unwanted movement of the horizontal arm was reduced by adding additional screws to secure the vertical axis guide rods to the mounting rails, which improved the stability of the arm. The PLA material spool was removed from the R-axis extruder assembly to decrease possible deflection of the arm, but this did not significantly improve print quality. The Theta- and R-axes motors need to move simultaneously for the extruder tool to move in a straight line using conversions performed in the Franklin C driver, which sends the Franklin Firmware a list of numbers of steps to move in either the positive or negative direction. The firmware takes this list and sends the steps to the motors. The reason for the inaccuracies in the 3D-printed part can be attributed to the Theta- and R-axes not operating simultaneously at the same speed. The Franklin coupling settings (steps/mm) in Delta-style 3D printers using the Franklin Firmware have had all motors for the extruder tool movement set to the same step/mm value.

Using a larger diameter nozzle will alleviate some inaccuracies, due to the large scale of the OSALS-Polar, and reduce overall printing time. Proper retraction and travel speed settings in the Cura software will minimize the stringing and oozing issues in the part. Some of the other issues that arose during testing included hot-end jamming, though only when the nozzle was too close to the table. Adjusting the Z-axis motor switch settings during the calibration process will correct this problem.

## Conclusions

The advantages of the OSALS-Polar 3D printer include a large print volume; but, with a large mechanical device, there are disadvantages in the scaling-up of inaccuracies in planar and perpendicularity of components. The OSALS-Polar can successfully operate in the R- and Z-axes with precision with 1 mm accuracy, and in the Theta-axis within 1°. The Franklin software efficiently controls the temperature of the hot end at the desired 210° C within a range of  $\pm 2^\circ$ . The Franklin software can operate the extruder motor to feed the 3-mm-diameter PLA material through the hot end nozzle at the desired rate. The G-code generated from Cura for a cylinder and cuboid test are not producing an accurate result at this time, but all three axes are operating automatically when the G-code is initiated.

The OSALS-Polar is deemed a partial success at this point, due to having accomplished most of the project's goals. This printer was relatively inexpensive to construct—under \$5,000 for materials. It operates using open source Franklin software that is continuously being improved. The

final testing of the system produced small extruded parts, although the accuracy and scaling up to larger-sized parts was not accomplished. Further work is planned in order to determine if the inaccuracies in the printed parts are due to the non-planar R-axis and Theta-axis table. The level of the R-axis arm and the printing surface can be adjusted with metal shims. New conversions may be necessary by the Franklin C driver to take into account the differences in the steps/mm Franklin coupling settings for the Theta- and R-axes motors. In the future, testing of larger parts may encounter limitations in the size of prints, due to material cooling at various rates and causing warpage.

## Acknowledgements

Appreciation for troubleshooting of the Franklin software for Gerald Anzalone, research engineer, Michigan Technological University. Also, assistance in testing, data collection and troubleshooting of the OSALS-Polar from MS in Mechanical Engineering students, Sachin Rana and Divy Patel, is much appreciated.

## References

- About Polar 3D LLC.* (2014). Retrieved from <https://about.Polar3d.com/printer/>
- Anderson, T. (2014). *Theta printer: A 3D printer with 4 extruders that can move independently and simultaneously.* Retrieved from <https://hackaday.io/project/812-theta-printer>
- Barnett, E., & Gosselin, C. (2015). Large-scale 3D printing with a cable-suspended robot. *Additive Manufacturing*, 7, 27-44.
- Berman, B. (2012). 3-D printing: The new industrial revolution. *Business Horizons*, 55(2), 155-162.
- Cano, L. M. (2015). *3D printing: A powerful new curriculum tool for your school library: a powerful new curriculum tool for your school library.* Goleta, CA: ABC-CLIO.
- Deshpande, S., Rao, N., Pradhan, N., & Irwin, J. L. (2016, November). Hybrid polymer additive manufacturing of a Darrieus type vertical axis wind turbine design to improve power generation efficiency. *Proceedings of the ASME 2016 International Mechanical Engineering Congress and Exposition.* New York: ASME.
- France, A. K. (2013). *Make: 3D printing: The essential guide to 3D printers.* Sebastapol, CA: Maker Media, Inc.
- Farcas, K. (2016). *R 360.* Retrieved from [http://reprap.org/wiki/R\\_360](http://reprap.org/wiki/R_360)
- Gebler, M., Uiterkamp, A. J. S., & Visser, C. (2014). A global sustainability perspective on 3D printing technologies. *Energy Policy*, 74, 158-167.
- Gibb, A. (2014). *Building open source hardware: DIY manufacturing for hackers and makers.* Carmel, IN: Pearson Education.
- Horne, R., & Hausman, K. K. (2017). *3D printing for dummies.* New York: John Wiley & Sons.
- Hoy, B. (2016). *Design and implementation of a three dimensional printer using a cylindrical printing process.* Retrieved from <https://digitalcommons.calpoly.edu/cgi/viewcontent.cgi?referer=https://search.yahoo.com/&httpsredir=1&article=1370&context=eesp>
- Irwin, J. (2013). Wind turbine blade CAD models used as scaffolding technique to teach design engineers. *Engineering Design Graphics Journal*, 77(2), 1949-1967.
- Pearce, J. M. (2014). *MOST RepRap build.* Retrieved from [http://www.appropedia.org/MOST\\_RepRap\\_Build#Calibration](http://www.appropedia.org/MOST_RepRap_Build#Calibration)
- Pradhan, N. K., Irwin, J. L., Siddegowda, B. R., & Harsha, S. (2016). Design and fabrication of the power transmission system of a large scale 3D printer. *Proceedings of the Association of Technology, Management, and Applied Engineering Conference.* New York: ATMAE.
- Replicator Warehouse, R-360: The most simple and modular 3D printer.* (2013). Retrieved from <http://www.kickstarter.com/projects/2132002936/r-360-the-most-simple-and-modular-3d-printer>
- Sells, E., Bailard, S., Smith, Z., Bowyer, A., & Olliver, V. (2010). RepRap: the replicating rapid prototyper: Maximizing customizability by breeding the means of production. In F. T. Pillar & M. M. Tseng (Eds.). *Handbook of research in mass customization and personalization* (pp. 568-580). River Edge, NJ: World Scientific.
- Steele, W. (2013). *PiMaker 3D printer.* Retrieved from <https://www.thingiverse.com/thing:128700>
- Wijnen, B., Anzalone, G. C., Haselhuhn, A. S., Sanders, P. G., & Pearce, J. M. (2016). Free and open source control software for 3-D motion and processing. *Journal of Open Research Software*, 4(1). Retrieved from <http://dx.doi.org/10.5334/jors.78>
- Wittbrodt, B. T. (2014). *Development of practical applications for RepRap style 3-D printers in engineering* (Unpublished doctoral dissertation). Michigan Technological University, Houghton, MI.
- Wittbrodt, B. T., Glover, A. G., Laureto, J., Anzalone, G. C., Oppliger, D., Irwin, J. L., & Pearce, J. M. (2013). Life-cycle economic analysis of distributed manufacturing with open source 3-D printers. *Mechatronics*, 23(6), 713-726.
- Wohlers, T. (2013). *Wohlers report 2013: Additive manufacturing and 3D printing state of the industry—Annual worldwide progress report.* Fort Collins, CO: Wohlers Associates.
- Yusuf, B. (2015). *3D printers explained: Delta, Cartesian, Polar, Scara.* Retrieved from <https://all3dp.com/your-fdm-3d-printers-cartesian-delta-Polar-and-scar/>

---

## Biographies

**SOURABH PRASHANT DESHPANDE** is a PhD student in the Mechanical Engineering Program at the University of Cincinnati, with a focus on additive manufacturing. Mr. Deshpande may be reached at [sourabhd@mtu.edu](mailto:sourabhd@mtu.edu)

**SHRINIVAS KULKARNI** is an MS student in the Mechanical Engineering Program at Michigan Technological University, with a focus on additive manufacturing. Mr. Kulkarni may be reached at [skulkar2@mtu.edu](mailto:skulkar2@mtu.edu)

**SID SHAH** is an MS student in the Mechanical Engineering Program at Michigan Technological University, with a focus on additive manufacturing. Mr. Shah may be reached at [ssshah1@mtu.edu](mailto:ssshah1@mtu.edu)

**JOHN IRWIN** is a professor of mechanical engineering technology at Michigan Technological University. He earned his EdD in Curriculum and Instruction in 2005 from Wayne State University. Dr. Irwin's research interests include STEM education, CAD/CAM and CAE, residential wind turbine design, and additive manufacturing methods. Dr. Irwin may be reached at [jirwin@mtu.edu](mailto:jirwin@mtu.edu)

# A COMPARATIVE STUDY OF THE THERMAL EFFICIENCY OF SOLAR VACUUM-TUBE VERSUS FLAT-PLATE COLLECTORS FOR WATER HEATING SYSTEMS

S.V. Vishnu Samudrala, Zimmer Biomet; Ahmed ElSawy, Tennessee Technological University; Mohan Rao, Tennessee Technological University; Stephen Idem, Tennessee Technological University

## Abstract

The world runs on the energy generated from the combustion of non-renewable energy sources such as fossil fuels (coal, petrol, and diesel) causing an increase in atmospheric pollution. Due to recent scientific discoveries, the use of renewable energy sources is made possible, economical, and environmentally friendly. Specifically, solar energy has the greatest potential of all the world's renewable energy sources. To absorb the sun's radiation and convert it to heat, solar collectors are needed. This preliminary experimental study focused on comparing the thermal performance of a commercially marketed solar water heating system that featured an evacuated-tube solar collector (STC) to that of a system that utilized a flat-plate collector (FPC) constructed using an air conditioning radiator as the collector. The STC system generally exhibited a 14% higher efficiency than the FPC system. The FPC system was relatively inefficient in the absence of direct sunlight, whereas the STC system remained effective even without direct solar irradiation.

## Introduction

This investigation experimentally compared the thermal performance of two solar water-heating systems. One system employed a commercially available heat pipe evacuated-tube solar collector (STC). The system utilized a pump to transfer the heated water/glycol mixture from the receiver to an insulated storage tank. The tank had a built-in copper heat exchanger coil to transfer heat from the working fluid to the potable water in the tank, thereby preventing the two fluids from mixing. The complete closed-loop system included an expansion tank and a control unit containing the circulation pump, pressure gauge, tempering valve, pressure relief valve, and flow meter. The other system considered in this study used a repurposed air conditioner radiator as a flat-plate collector (FPC). It consisted of an array of serpentine tubes through which water was circulated. The presence of high-density corrugated fins attached to the tubes increased the absorption of incident solar radiation. The flat

-plate collector was enclosed by double-glazing that admitted solar radiation and minimized convection heat transfer losses to the environment. The shell of the collector was insulated to reduce conduction losses. This system likewise utilized a coiled copper heat exchanger coil to transfer heat from the working fluid to an insulated storage tank. The water flow through the receiver was obtained by means of an off-the-shelf circulation pump. As described subsequently, this system was then fully instrumented to measure the working fluid flow rate and temperatures, as well as the receiver and cover plate temperature, in an effort to estimate thermal losses. The goal of the present study was to assess whether a solar water heating system constructed using relatively inexpensive, scavenged components could exhibit thermal efficiency equivalent to that of a more expensive vacuum tube solar collector system that is available for sale.

It has been demonstrated (ASHRAE, 2015) through the use of STCs that the combination of effective convection suppression and selective surface absorption yields improved thermal efficiency at high temperatures. Like the FPC, STCs collect both direct and diffuse radiation. However, their efficiency is higher at low incidence angles, which gives STC an advantage over FPC in day-long performance. Depending on the solar insolation level of the locality, the authors found that working fluid outlet temperatures of 80°C to 200°C can be achieved (Made-in-China, n.d.). Fundamental studies of STC thermal performance have been reported by Duffie and Beckman (1991), Budihardjo and Morrison (2009), Rittidech and Wannapakne (2007), and Ma, Lu, Zhang, and Liang (2010). Kim and Seo (2007) and Shah and Furbo (2004) employed evacuated tube collectors made from a two-layered glass tube with circular fins and a U-tube absorber. Measured collector efficiencies were 55.8% and 60%, respectively.

The study reported by Tripanagnostopoulos, Souliotis, and Nousia (2000) using a flat-plate collector model achieved a minimum outlet temperature of 50°C, and had a collector efficiency of 80%. Zelzouli, Guizani, Sebai, and Kerkeni (2012) concluded that the number of FPCs that can

be connected in series is limited. When collectors are connected in series, the outlet temperature of each collector will increase, when compared to parallel or series-parallel connected collectors, and this leads to an increase in thermal losses, due to increased temperature differences.

Jouhari, Touhmeh, and Moukhayber (2015) demonstrated that by combining both flat-plate and evacuated-tube collectors, the thermal performance of the compound collector was improved. Ben Slama (2012) conducted experiments on an integrated flat-plate/evacuated-tube collector and found that the efficiency of double glazing was 42%, whereas with single glazing the efficiency was 30%. Shukla, Sumathy, Erickson, and Goung (2013) summarized the current state-of-the-art concerning system components of solar water heaters, such as the collector, storage tank, and heat exchanger, and likewise discussed various approaches to improving performance and cost effectiveness of solar water heaters. The FPC is usually permanently fixed in position and does not require any tracking of the sun. The collectors should be placed directly towards the equator, facing due south in the northern hemisphere. The ideal tilt angle of the collector is equal to the latitude of the location, with angle variations of 10-15°C, depending on the application. According to the test results of Duffie and Beckman (1991), they are capable of producing temperatures up to 100°C above the ambient temperature. FPCs are the most common type of collectors used in solar water heating systems in Africa, supplying hot water in hotels, hospitals, and to wealthier households (Karaekezli & Ranga, 1997).

## Experimental Setup

The STC utilized in this current study was a commercially available Duda Energy (model SC5815) solar collector (Duda, n.d.). It consisted of 15 parallel transparent glass tubes supported on a frame and connected to a header pipe. In each instance, the evacuated tube outer diameter was 58 mm (2.28 in.), and the overall length was 1.80m (70.9 in.). The tubes were evenly spaced on the frame, such that the overall footprint of the STC was 2,050 mm × 1,145 mm (80.7 in. × 46.7 in.); complete details are provided in Duda (n.d.) and Samudrala (2016). The STC was mounted on the roof of a building with a pitch of approximately 28°, and was oriented due south. Reflective insulation was placed beneath the STC to minimize losses and to enhance the solar energy incident on the backside of the tube array. The flexible steel pipes leading to/from the STC were wrapped with standard 6-mm-thick (0.25 in.) foam insulation. Each individual collector tube consisted of two concentric glass tubes. The annulus between the tubes was evacuated to minimize convection heat loss to the environ-

ment. The tubes were constructed using borosilicate or soda lime glass, which is resistant to high temperatures and has a high transmittance for solar irradiation. A flat or curved aluminum or copper fin was attached to a metal heat pipe running through the inner tube. The inner glass tube and fin was covered with a selective coating that maximizes absorption of solar energy.

The hollow copper heat pipe within the tube contained a small volume of a low-pressure alcohol/water liquid, as well as some additional additives to prevent corrosion or oxidation. This partial vacuum enabled the liquid to vaporize at a prescribed temperature, which is lower than would be possible at atmospheric pressure. When solar radiation was incident on the surface of the heat pipe, the liquid in the heat pipe was vaporized, due to the absorption of heat. Therein the increased vapor pressure drove the hot vapor to the top portion of the heat pipe, which consisted of a “hot bulb” inserted through a copper well located within a connecting manifold. A water/glycol mixture flowed through the manifold, and heat was transferred to the working fluid as it flowed past the hot bulb condensers in the manifold. As the hot vapor in the heat pipe lost energy, it cooled and subsequently condensed. Then it flowed back down the heat pipe through a wick/porous mesh by a combination of gravity and capillary action. This cyclic process of alternating evaporation and condensation of the liquid within the sealed heat pipe continued as long as radiant energy was incident upon the vacuum tubes. Per Tripanagnostopoulos et al. (2000), a depiction of the STC closed-loop solar water heating system is provided in Figure 1.

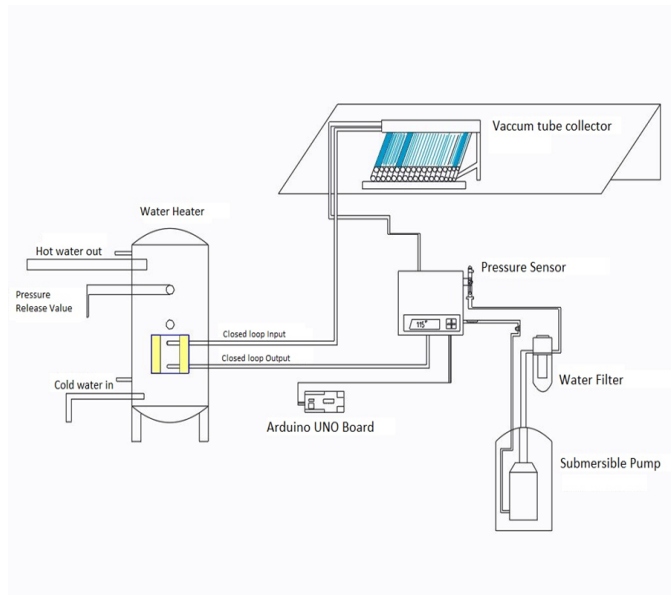


Figure 1. STC solar water heating system. Printed with permission.

The working station supplied with the STC system included an integrated flow meter with a digital display. Likewise, the working station contained a flow controller and pressure relief valve. The water storage tank used in conjunction with the STC system consisted of two concentric tanks, one larger and one smaller. The annular gap between the tanks was filled with mineral wool to reduce heat loss. Copper-constantan thermocouples were mounted at the inlet and outlet of the STC header to record the water/glycol temperatures. The ambient temperature and solar insolation data were downloaded directly from a local weather station. Further details regarding this aspect of the current study are available in the study by Samudrala (2016).

The FPC considered in this current study (Chittireddy, 2017; Chittireddy, ElSawy, & Idem, 2018) was fully instrumented to measure such variables as water flow rate and temperature rise, solar insolation, and receiver and cover plate temperatures. Figure 2 shows a photograph of the apparatus. Throughout the experiments, the flat-plate receiver was positioned to face directly south and was inclined at an angle so that solar insolation was directed normally onto the apparatus. This orientation was maintained throughout the duration of the experiments. Major components of the FPC solar collector system considered in this study were:

1. The receiver plate (a repurposed air conditioner radiator)
2. A water storage tank
3. The casing for the collector and insulation on the bottom to reduce heat loss
4. Two layers of glazing cover
5. A linear actuator to control the inclination of the collector
6. A water-circulating pump

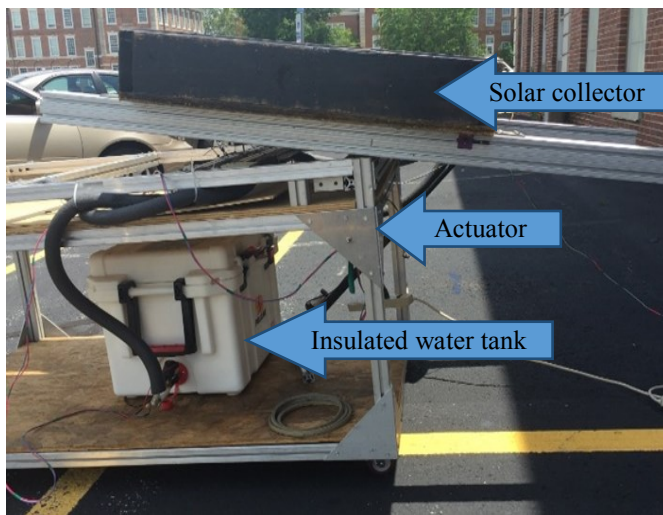


Figure 2. FPC solar water heating system. Printed with permission.

Other components of the FPC system included calibrated temperature sensors, a water mass flow-rate sensor, and a data acquisition system. An air conditioner radiator was selected as the receiver plate. The radiator coil consisted of a single continuous serpentine tube configured in three rows by means of headers. Each row of the radiator had 22 straight finned-tube sections that were parallel to one another, and were arranged in a single plane. The thickness of the fins was 0.25 mm, and there were 591 continuous plate fins per meter. The cross-sectional area of the receiver plate was 0.73m × 0.56m. The material of the tubes was copper and the fins were constructed from aluminum. These fins were coated with black paint to increase solar heat absorptivity. Two acrylic sheets were employed as glazing for the FPC. Plexiglas was used because it has a transmittance closely equivalent to optical glass. The total light transmittance of Plexiglas is 92%, and the emissivity is 0.86% (Chittireddy et al., 2018). Radiation losses from the glass cover were reduced, since it is transparent to the short-wave radiation emitted by the sun and is nearly opaque to long-wave thermal radiation emitted by the absorber plate.

In this experiment, double parallel glazing was used. Each glazing had a thickness of 6 mm. The distance between the two cover plates was 19 mm, and distance between the absorber plate and the lower cover plate was 36 mm. Eleven copper-constantan thermocouples were used to measure the temperature at prescribed locations on the receiver and cover plates, as well as the inlet and water temperatures. Three thermocouples were mounted to the upper cover plate, three were attached to the lower cover plate, and three thermocouples were affixed to the receiver plate, and the resulting values were averaged. Two thermocouples were used to measure the inlet and outlet temperatures of the receiver plate by inserting them directly into the 13-mm-diameter steel pipes leading to/from the copper pipes in the radiator. Prior to installation in the solar water heater, each temperature sensor was calibrated using a reference immersion thermometer.

Water flow was measured using a calibrated flow sensor. The flow sensor required a voltage input of 5-18VDC (supplied by the data acquisition system). It was capable of measuring flow rates from 1 to 30 L/min over a temperature range of -25°C to +80°C. The water flow sensor was installed in a 1.5m-long pipe, which was between the outlet of the collector and the storage tank. A sufficient length of pipe was employed upstream of the flow sensor to ensure that the entering flow was fully developed. The casing, receiver plate, and water storage tank used with the FPC were mounted on a moving trolley. The data acquisition system was placed on another moving trolley. Each time an experiment was performed, the experimental setup mounted on

the trolleys was moved out into an open area to receive solar radiation. In every instance, the solar water heater was manually positioned facing south during the acquisition of performance data. Once the setup was initially positioned, the setup was not further adjusted (i.e., solar tracking was not employed while measurements were being performed). The casing was placed on horizontal bars capable of moving vertically. The horizontal bar was connected to a 12VDC linear actuator to raise the casing vertically and to align the receiver's placement so that it was perpendicular to the solar irradiation at the start of the experiments. The storage tank was placed under the casing and a 12VDC circulating pump was connected to circulate the heat transfer fluid through the solar collector.

The solar thermal systems utilized solar collectors located remotely from the storage tank. Both systems used a pump to circulate a water/propylene glycol mixture between the storage tank and the collector in a continuous loop and back again to the storage tank. In each instance, a copper heat exchanger coil located in the insulated storage tank was used to transfer heat acquired by the collectors from working fluid to the potable water present in the tank without mixing the fluids together. In general, this is advantageous, since the storage tanks can be placed indoors, reducing heat loss in winter months. In addition, backup heating systems may be installed in the storage tanks to supply enough heat to meet the demands of the user in case of cloudy or rainy weather. Furthermore, this permits placing the tank close to where the water will be used, thereby reducing the time needed for hot water to flow from the tap.

## Data Acquisition and Reduction

A Raspberry Pi system was used to connect all of the temperature sensors for data acquisition. The Raspberry Pi is a low-cost, credit card-sized computer that plugs into a computer monitor or TV and uses a standard keyboard and mouse. A simple Python code was used to configure the temperature sensors. The data were collected and exported to a .csv file for further analysis. An open source computer hardware and software system was used to acquire the data from each of the experimental setups. The performance of a solar water heater was characterized by how efficiently it could convert the energy of incident solar energy to a corresponding increase in the temperature of a circulating hot water/glycol mixture. The thermal efficiency of each collector considered in the present study was calculated using Equation 1:

$$\eta_c = \frac{\dot{m} C_p (T_o - T_i)}{A_c \cdot G_t} \quad (1)$$

where,

- $\dot{m}$  = Mass flow rate in kg/sec
- $C_p$  = Specific heat capacity in J/kg-K
- $A_c$  = Collector area in  $m^2$
- $G_t$  = Global solar radiation on the collector in  $W/m^2$
- $T_o$  = Collector outlet temperature in K
- $T_i$  = Collector inlet temperature in K

In this instance,  $\dot{m}$  refers to the measured water/glycol mass flow rate through the system, and  $T_o$  and  $T_i$  are the temperatures recorded at the collector inlet and outlet, respectively. The quantity  $G_t$  is the measured solar radiation incident upon the collectors, as measured by the local weather station. Likewise,  $A_c$  denotes the effective cross section of each collector, and  $C_p$  indicates the average working fluid specific heat.

## Results

The testing of the STC and FPC solar water heating systems was performed under different ambient seasonal temperatures. Various weather conditions—cloudy, rainy, and sunny—were encountered throughout the test program. The measurements were conducted approximately five hours a day and were initiated around noon, when the sun was at its highest elevation. The data were acquired every 13 seconds throughout the test cycle. Figure 3 illustrates the performance of the STC system on different days, subject to disparate ambient temperatures and levels of solar insolation, in terms of the measured outlet water/glycol temperatures. At noon (peak incident solar radiation), the collector efficiency calculated by means of Equation 1 for cold weather conditions was 69.8%. At that time, the global solar radiation was found to be 812  $Watt/m^2$ . The useful energy collected was 1,136 kJ/day. By comparison, measurements conducted later in the season under warm conditions yielded a calculated collector efficiency at noon of 81.5%, when the measured global solar irradiation was found to be 842  $Watt/m^2$ . The energy collected in the STC system was determined to be 1,401 kJ/day. Under similar conditions of ambient temperature and incident radiation intensity, STC systems exhibited approximately 14% higher efficiency than the FPC system.

Figure 4 shows a comparison of the thermal performance of the STC and the FPC solar water heating systems considered in this study on the same day. Both systems were charged with a similar water/glycol mixture. In this instance, the initial ambient temperature was 71°F. At the start of the experiments, the measured water/glycol temperature stored in the insulated tank in the STC apparatus was 79°F, whereas the corresponding initial water/glycol temperature for the FPC system was 98°F. At the end of experi-

ment, the solar vacuum tube collector water/glycol temperature reached 147°F. This temperature was similar to that of the flat-plate collector; both systems yielded the same outlet temperature over the duration of the experiments, but the STC temperature rose to its final value more quickly. Since the ambient temperature was warm, the collectors performed similarly.

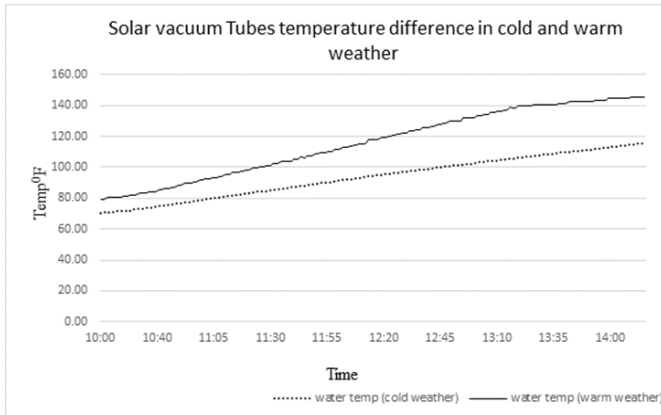


Figure 3. STC performance comparison in cold and warm weather.

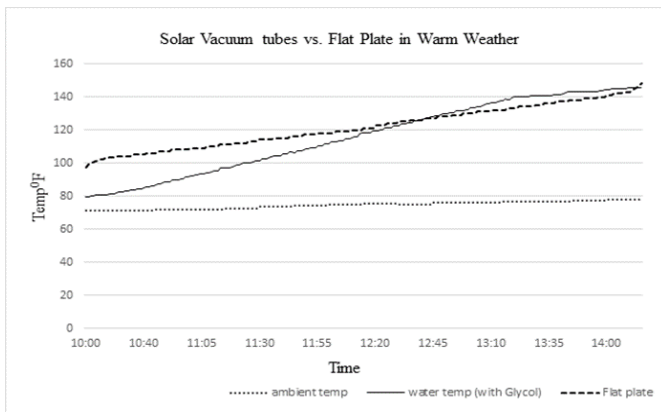


Figure 4. Daily performance comparison of STC and FPC solar water heating systems in warm weather.

Figure 5 provides an additional comparison of the STC and FPC solar water heating systems. At the start of the experiments, the ambient temperature was 86°F. In this case, the initial water/glycol temperature for the STC system was also 86°F. However, at the start of the measurements, the working fluid temperature in the FPC system was 80°F. Upon the completion of the tests, the final water/glycol temperature recorded leaving the STC system was 134°F, and the equivalent temperature for the FPC was 130°F. In this instance, the STC system yielded a higher final temperature; but, for both systems, the rate of tempera-

ture increase was almost identical. The calculated collector efficiency of the STC system at noon was determined to be 88.7%, when the incident solar radiation was 904 W/m<sup>2</sup>. That corresponded to a useful daily energy collection for the STC system of 1,636 kJ/day.

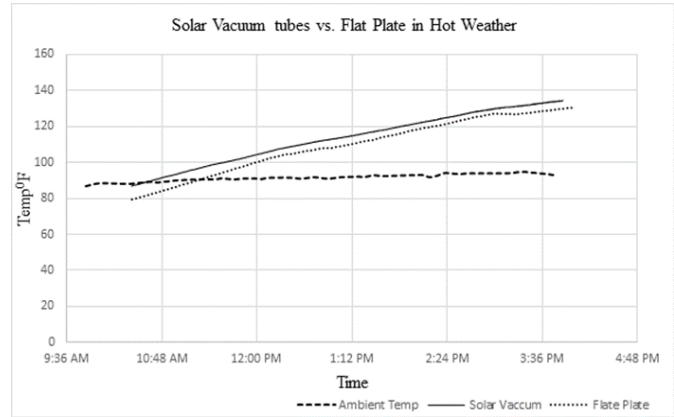


Figure 5. Daily performance comparison of STC and FPC solar water heating systems in hot weather.

## Conclusions

This preliminary study compared the thermal performance of a commercially marketed solar water heating system that featured an evacuated-tube solar collector to that of a system that utilized a flat-plate collector constructed using an air conditioning radiator as the collector. Although an extensive side-by-side comparison of the thermal efficiency of the two systems proved to be impractical, the STC system generally exhibited a 14% higher efficiency than the FPC system. It should be pointed out that the water heater systems considered in this study employed different water/glycol mixture flow rates and had unequal cross sections. Likewise, the same inclination angle of each collector was not consistent, and each system utilized different storage tanks that were not equally insulated. Collectively, these differences between the two solar heating systems make it difficult to definitively compare the two approaches in terms of thermal efficiency.

While flat-plate collectors are widely used in solar water heating applications, they are inefficient in the absence of direct sunlight. By comparison, STC systems are relatively more effective, even without direct solar irradiation. The simple flat-plate collector considered in this study was assembled using readily available spare components. It was designed to work in sunny and warm climates. However, the benefit of using the FPC system was reduced when there were cloudy, rainy, or windy weather conditions. Solar water heating systems that employ evacuated-tube col-

lectors similar to those employed in the present study may be more energy efficient than the flat-plate collectors, due to their unique construction. Since the concentric coated-glass tubes are vacuum-sealed, heat loss associated with convection heat transfer is reduced to a great extent. Although the STC system was deemed more thermally efficient, it was far more expensive than the FPC system. However, a detailed analysis of the relative initial and annual operating costs of the two systems was beyond the scope of the present study.

## References

- ASHRAE. (2015). *Handbook HVAC applications*. Atlanta: ASHRAE.
- Ben Slama, R. (2012). Experimentation of a plane solar integrated collector storage water heater. *Energy and Power Engineering*, 4(2), 67-76.
- Budihardjo, I., & Morrison, G. L. (2009). Performance of water-in-glass evacuated tube solar water heaters. *Solar Energy*, 83(1), 49-56.
- Chittireddy, V. R. (2017). *A study of flat plate solar collector with air conditioner radiator as absorber plate*. (Master's thesis). Retrieved from ProQuest Dissertations and Theses Database. (UMI No. 10246377)
- Chittireddy, V. R., ElSawy, A., & Idem, S. (2018). *Study of a flat plate solar collector with an air conditioner radiator as a heat absorber for a domestic water heater*. Paper presented at the International Conference on Renewable Energies and Power Quality. doi: <https://doi.org/10.24084/repqj16.205>
- Duda diesel. (n.d.). Retrieved from <https://www.dudadiesel.com/>
- Duffie, J. A., & Beckman, W. A. (1991). *Solar engineering of thermal processes*. 2nd ed. New York: Wiley-Interscience.
- Jouhari, M., Touhmeh, S., & Moukhayber, N. (2015). Manufacturing and thermal performance test of (compound) solar collector in Damascus City. *Journal of Biomedical Science and Engineering*, 8(6), 370-379.
- Karaekezi, S., & Ranga, T. (1997). *Renewable energy technologies in Africa*. London: Zed Book Ltd.
- Kim, Y., & Seo, T. (2007). Thermal performances comparisons of the glass solar vacuum tube solar collectors with shapes of absorber tube. *Renewable Energy*, 32(5), 772-795.
- Ma, L., Lu, Z., Zhang, J., & Liang, R. (2010). Thermal performance analysis of the glass Solar Vacuum tube collector with U-tube. *Building and Environment*, 45(9), 1959-1967.
- Made-in-China. (n.d.). Retrieved from <https://www.made-in-china.com>
- Rittidech, S., & Wannapakne, S. (2007). Experimental study of the performance of a solar collector by closed-end oscillating heat pipe (CEoHP). *Applied Thermal Engineering*, 27, 1978-1985.
- Samudrala, S. V. Vishnu. (2016). *A comparative study on the thermal efficiency of solar vacuum-tube vs. flat-plate collectors for water heating systems*. (Master's thesis). Retrieved from ProQuest Dissertations and Theses Database. (UMI No. 10243376)
- Shah, L. J., & Furbo, S. (2004). Vertical evacuated tubular collectors utilizing solar radiation from all directions. *Applied Energy*, 78(4), 371-395.
- Shukla, R., Sumathy, K., Erickson, P., & Goung, J. (2013). Recent advances in the solar water heating systems: A review. *Renewable and Sustainable Energy Reviews*, 19, 173-190.
- Tripanagnostopoulos, Y., Souliotis, M., & Nousia, T. (2000). Solar collectors with colored absorbers. *Solar Energy*, 68(4), 343-356.
- Zelzouli, K., Guizani, A., Sebai, R., & Kerkeni, C. (2012). Solar thermal systems performances versus flat plate solar collectors connected in series. *Engineering*, 4(12), 881-893.

## Biographies

**VENKAT VISHNU DEEPAK SAMUDRALA** is a manufacturing engineer at Zimmer Biomet and holds an MS degree from Tennessee Technological University (2016) in mechanical engineering. He was born in Hyderabad, India, and holds a BS degree from SCSVMV University, India (2010), in mechanical engineering. While pursuing his BS degree, he developed a profound interest in energy systems, which inspired him to work on solar water heating systems as his master's thesis. Currently, he lives in Memphis, Tennessee, and is working on a continuous improvement project focused on reducing product manufacturing time. Mr. Samudrala may be reached at [ssamudral42@students.tntech.edu](mailto:ssamudral42@students.tntech.edu)

**AHMED ELSAWY** joined Tennessee Technological University as a professor and chairperson in the Department of Manufacturing and Engineering Technology, in July 1999. Prior to joining TTU, he was a professor and graduate program coordinator in the Department of Industrial Technology at the University of Northern Iowa, the founding director of the Manufacturing Engineering Program at St. Cloud State University in Minnesota, and a full professor at the Department of Mechanical Design and Production Engineering at Cairo University. His teaching and research interests include material processing, metallurgy and manufacturing systems, recycling and reuse of solid waste materials, renewable energy, and sustainability. Dr. ElSawy advised

---

several master's and doctoral students who hold academic and industrial positions in the USA, Germany, and Taiwan. Dr. Elsawy may be reached at [aelsawy@tntech.edu](mailto:aelsawy@tntech.edu)

**MOHAN D. RAO** is a professor and chair of Mechanical Engineering at Tennessee Technological University. Previously, he was a professor of Mechanical Engineering at Michigan Tech. Dr. Rao is a fellow of ASME and SAE. He has conducted research in different areas of automotive body and powertrain dynamics, acoustics, and vibration over a span of 30 years. He has over 100 publications in technical journals and conference proceedings. He has advised 9 PhD and 35 MS students. Dr. Rao has received a US Fulbright award, National Science Foundation Research Initiation award, and was honored by the NASA Marshall Space Flight Center for his work on the damping of the Hubble Space Telescope truss system. Dr. Rao may be reached at [mr Rao@tntech.edu](mailto:mr Rao@tntech.edu)

**STEPHEN IDEM** is a professor in the Department of Mechanical Engineering at Tennessee Tech University. He received his PhD in mechanical engineering from Purdue University. He has more than 30 years of experience in the areas of scale model testing, fluid flow measurement, and thermal modeling. Currently, he is engaged in projects to measure airflow and pressure loss characteristics of residential HVAC duct systems. He has created a numerical model of downdraft evaporative cooling tower performance, which is being verified experimentally. He has extensive experience performing flow and pressure measurements on scale models of primary and secondary air supply ducts, wind boxes, and exhaust stacks of coal-fired power plants to improve their thermal performance. He has developed an online cleanliness factor model of the convection passes in coal-fired power plants. He has likewise created numerical models of transient heat exchanger performance. Dr. Idem may be reached at [sidem@tntech.edu](mailto:sidem@tntech.edu)

# DESIGN AND DEVELOPMENT OF A GUI FOR RF COMMUNICATIONS

Ehsan Sheybani, University of South Florida; Giti Javidi, University of South Florida

## Abstract

In this paper, the authors describe the requirements and features necessary to develop a GUI for RF airborne, spacecraft, and satellite communications. The proposed GUI is responsive to the variety of devices and tools an RF engineer would need to accomplish everyday tasks. This includes, but is not limited to, Smith charts, polar plots, Bode diagrams, and different types of data files associated with these graphs or charts. The GUI was designed and developed in MATLAB, with Adobe Photoshop used to create a custom background. The user interface was fully tested and validated for functionality and ability to import, plot, and export data for Smith charts, polar plots, and Bode diagrams. The GUI also has a toolbar, file browser with picture display, custom background, and a static textbox that displays the plotted data.

## Introduction

Following are the details of the steps that were taken in order to apply signal processing and data analytics algorithms in the design of a graphical user interface (GUI) for satellite and RF communications. Users may follow these steps with the specified set of hardware and software to get the same configuration on the proper RF communications and device design. These projects were implemented under the supervision of NASA scientists and faculty advisors in dedicated NASA labs. Using lessons learned in this study, and the authors' previous experience in data visualization and signal processing research and training, relevant labs were designed to enhance the Computer Engineering program at the Virginia State University (VSU). The classes and labs covered a variety of topics, including computer simulations and networking (Javidi & Sheybani, 2008), (Sheybani & Javidi, 2007), visualization and virtual labs (Sheybani & Javidi, 2006), image processing (Sheybani, Garcia-Otero, Adnani, & Javidi, 2012), game design (Ouyang, Yang, Franklin, Michaelson, Morge, et. al., 2010), STEM education (Javidi & Sheybani, 2008), (Javidi & Sheybani, 2010), spike removal (Sheybani, Mengshoel, & Poll, 2010), feature detection (Varde, Rundensteiner, Javidi, Sheybani & Liang, 2007), wireless communications (Hardy, Javidi, Denton, Campbell, & Sheybani, 2007), (Badombenawanta & Sheybani, 2010), network architecture (Sheybani & Sankar, 2002), optical communications (Sheybani & Aro-

ra, 1992), dimension reduction and noise removal (Sheybani, 2011), and senior design (Garcia-Otero & Sheybani, 2011).

RF engineers specialize in creating various devices that operate within the radio frequency spectrum. Some of the devices they work with include antennas, radios, WiFi, and mobile phones. In this current study, the RF engineer was in the process of developing an antenna for a NASA project called EcoSAR, a radar tool designed to help scientists better understand the carbon cycle by measuring biomass, forest height, density, and extent. This project was designed to help him by creating a GUI that could import, analyze, and export data.

## Technical Details

A GUI is a type of computer-human interface on a computer. It solves the blank screen problem that confronted early computer users (Norman, 1988). A computer-human interface is a "means by which people and computers communicate with each other" (Interface, 2019). GUI binds the user of the computer system to the operation and potential of the computer system. More specifically, a GUI is a specification for the look and feel of the computer system (Bonsiepe, 1989). GUIs usually have common characteristics, such as windows, icons, menus, and pushbuttons (WIMP). Collectively, WIMPs are pictures that bring forth a certain action or action space. The user issues commands via the GUI to computer applications. GUIs usually have three major components (Hayes & Baran, 1989): a windowing system, an imaging model, and an application program interface (API). The windowing system builds the windows, menus, and dialog boxes that appear on the screen. The imaging model defines the fonts and graphics that appear on the screen. WIMPs are products of both the windowing system and imaging model. Finally, the API is the means by which the user specifies how and what windows and graphics appear on the screen.

The proposed GUI consists of the following platforms: data input, selection menu, scientific computation, and results display. The scientific computations include file type conversion, S-parameter, polar-rectangular conversion, Smith chart, and graphs/plots. The GUI was designed in MATLAB and, as a result, MATLAB libraries were used for parts of the design and development of the GUI.

The GUI is capable of importing three main data types: (.CSV), (.DAT), and (.SNP) files. CSV stands for a “comma separated value.” This is a plain text file that separates each form of data with a comma. Figure 1 shows how CSV files can be written in either Notepad or Excel; and, when used properly, they can import and export data from Excel to MATLAB and vice versa.

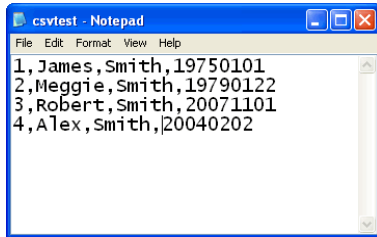


Figure 1. A CSV file written in Notepad.

DAT files are primarily associated with “data.” They can be used to store various types of data, such as text, graphics, attachments in emails, and general binary code. In most instances, it is best to open a DAT file with the program that created it. Users can also open a DAT file with an editor such as Notepad to view the contents inside. However, it is not guaranteed that all of the contents of the file will be readable when using an editor to open it. SNP files, which are also known as touchtone files, have five different file types: (.S1P), (.S2P), (.S3P), (.S4P), and (.SNP). The differences between these file types are the number of ports present (see Table 1).

Table 1. The number of ports and S-parameters associated with each file type.

File type	Number of ports	Number of S-parameters saved
.s1p	1	1
.s2p	2	4
.s3p	3	9
.s4p	4	16
.sNp	N	N <sup>2</sup>

The “S” in S-parameters stands for scattering. Figure 2 shows examples of how S-parameters come in matrices with the number of rows and columns equal to the number of ports. These S-matrices allow users to describe complicated networks as “black boxes” (Zhou & Chen, 2008). S-parameters are considered complex, because both phase and magnitude change the network. However, most microwave and RF engineers are only concerned with the magnitude. These engineers use S-parameters to refer to the RF “voltage out vs. voltage in.”

$$(S_{11})_{(\text{one-port})}$$

$$\begin{pmatrix} S_{11} & S_{12} \\ S_{21} & S_{22} \end{pmatrix}_{(\text{two-port})}$$

$$\begin{pmatrix} S_{11} & S_{12} & S_{13} \\ S_{21} & S_{22} & S_{23} \\ S_{31} & S_{32} & S_{33} \end{pmatrix}_{(\text{three-port})}$$

Figure 2. S-parameter matrices.

- (S11) Refers to the reflection on port 1 as an incidence of port 1.
- (S12) Refers to the reflection on port 1 as an incidence of port 2.
- (S22) Refers to the reflection on port 2 as an incidence of port 2.
- (S21) Refers to the reflection on port 2 as an incidence of port 1.

Since three-port measurements are extremely difficult to obtain accurately, the authors chose to focus only on one- and two-port systems. However, the aforementioned methodology would continue for all of the S-parameters present. These data formats are all associated with specific graphs. Figure 3 shows that the first graph, the Bode diagram, consists of both phase and magnitude plots. The magnitude plot expresses the magnitude of the frequency response gain either linearly or in decibels. The phase plot expresses the frequency response phase shift in either degrees or radians (Zhou & Chen, 2008).

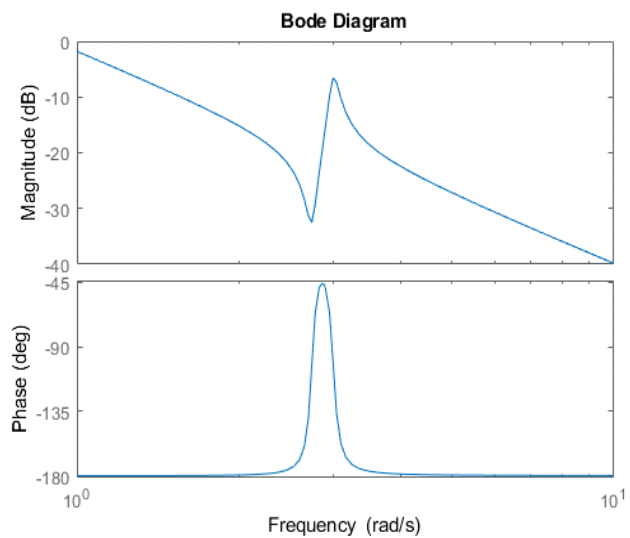


Figure 3. A Bode diagram.

Figure 4 shows the next graph, a polar plot. This is a two-dimensional system that plots polar coordinates in a Cartesian plane and then draws the polar grid on the plane. These plots sometimes display the voltage reflection coefficient. This plays an important role in helping microwave engineers with impedance matching. Polar plots are also similar to X & Y plots. However, instead of plotting data at X versus Y, they plot “R” (magnitude) at an angle between 0 and 360 degrees.

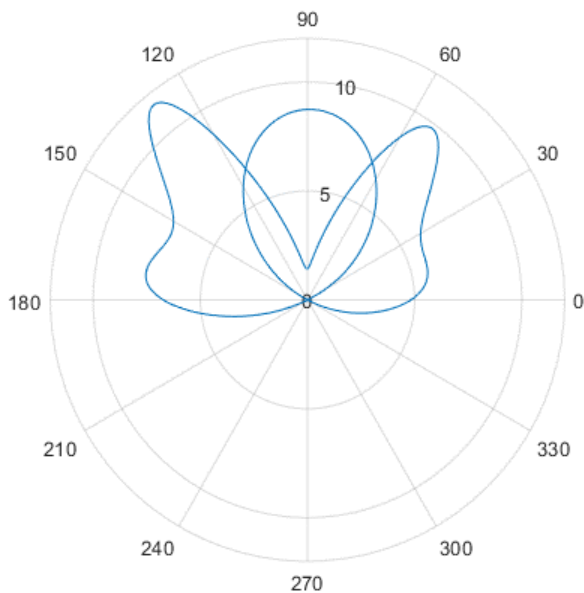


Figure 4. A polar plot.

Figure 5 shows the last graph, a Smith chart. The capabilities of this chart are limitless, and it is standard in microwave engineering. The Smith chart is a plot of complex reflection overlaid with impedance and/or admittance grids referenced to a 1-ohm characteristic impedance. Smith charts help assist RF engineers in many ways, but some of the most notable tasks include impedance matching, displaying antenna impedance, and visualizing the impedance of a transmission line. There are two types of Smith charts: the classic chart displays only positive real impedances, while the more modern chart displays imaginary impedances from negative infinity to positive infinity (Gawa, 2006).

## Methods and Procedures

To create this GUI, MATLAB was used to program/develop the GUI, and Adobe Photoshop was used to create the custom background. The hardest part of the project was writing the code to make the GUI accomplish various tasks.

When complications were encountered, the authors used various problem-solving methods. The “help” and “doc” functions in MATLAB and MATLAB online forums were used extensively. General steps to implementing this project were as follows:

1. Researching data types and graphs
2. Brainstorming what the end result should look like
3. Creating flow charts
4. Developing program code
5. Ensuring the GUI could accomplish the assigned tasks
6. Creating a custom background
7. Adding extras (static text display, toolbar, file browser, etc.)
8. Cleaning up code for efficiency
9. Finishing poster and final paper

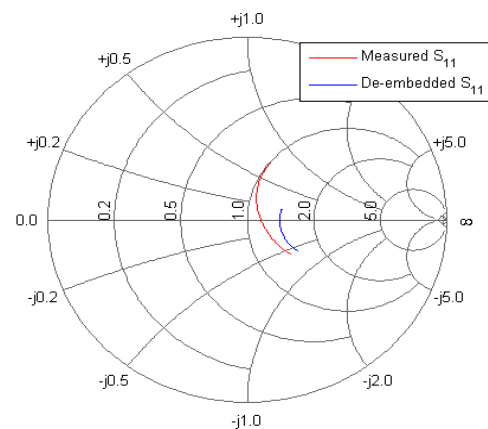


Figure 5. A Smith chart.

## Results and Discussion

Figure 6 shows the completed GUI. One attractive feature is the background/layout. This custom background was created in Photoshop and saved as a .JPG and then placed on a panel in MATLAB. The background of the GUI needed a visual appeal or style to it. The panels helped increase the overall intuitiveness of the design. This was because it gave everything its own special area, as opposed to the thin and basic borders MATLAB had to offer. The input function was placed in the toolbar of the GUI. From there one can select and import files located within the file directory. The GUI was programmed to automatically plot the Smith chart, polar plot, and Bode diagram when certain data were imported, allowing the user to import any file type and still plot it correctly. In addition to these features, the input allows the user to import M-files as well. Figure 7 shows how to access the import feature using the path: *File* → *Open* → (*Select Data*) *Open*.

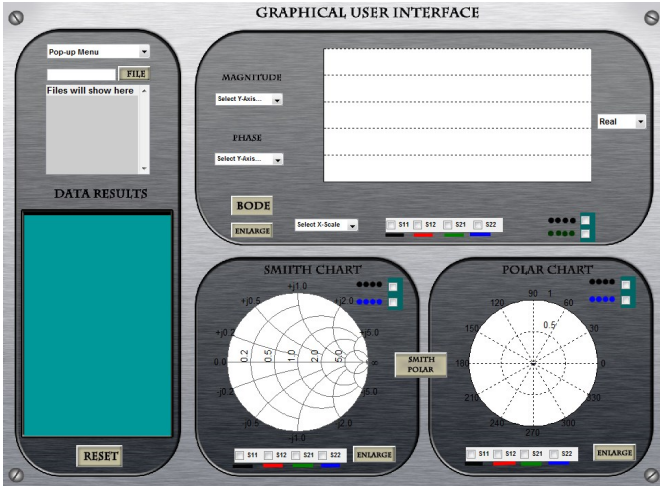


Figure 6. The completed GUI.

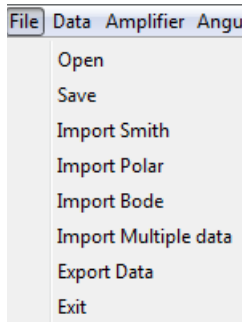


Figure 7. GUI file menu.

Another feature added to the GUI was the ability to graph multiple plots. By using this feature, two sets of data could be displayed on one plot simultaneously. Figure 8 shows how this can be highly effective in helping RF engineers compare results.

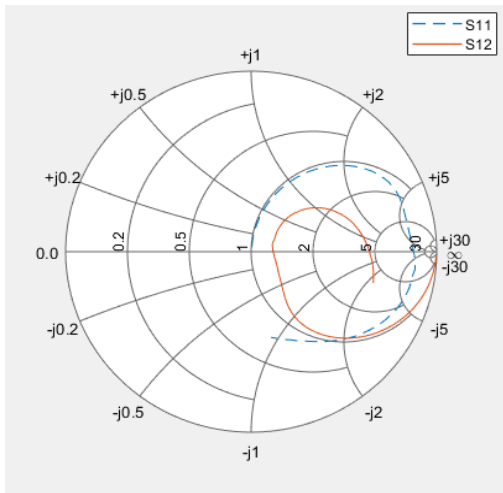
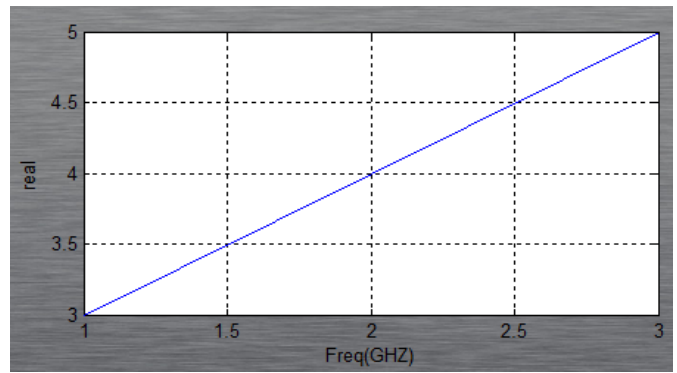


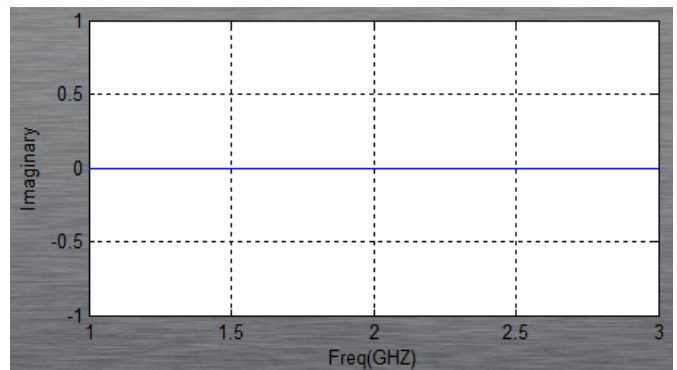
Figure 8. Multiple sets of data plotted on one Smith chart.

An export button was also created that allows the user to export data anywhere within the file directory. However, instead of an “open” button, the user would see a “save” option. To access the import feature: *File* → *Save* → *(Name & Location) Save*.

The Bode diagram section is located in the large rectangular area of the GUI. Here, the user can select the number of options and change how to view the imported data. The first option the user can manipulate is the Y-axis for the magnitude and phase plots. Under the magnitude option, the user can choose from either linear or log (dB), and under the phase option the user can choose degrees or radians. The second option to choose is the real and imaginary axis of the Bode diagram. Figure 9 shows how this option allows users to select the axis most practical for their research.



(a) The real axis.



(b) The imaginary axis.

Figure 9. The axes.

The interface has checkboxes to allow users to select which color they would like their graph or specific S-parameters to appear in. This allows users to more easily distinguish different sets of data. In addition to adding color checkboxes, checkboxes to select between solid and dotted lines were added. This also helps users distinguish between different sets of data. To graph random data, the “Bode”

button was added, and the “enlarge” button was added right beneath it to display a larger version of the Bode diagram in a separate window. This helps engineers get a closer look at the data plot in case the view on the GUI is not large enough. The same approach was used for other types of graphs. The control panel is the long rectangular panel located on the left side of the GUI. Here, the user can perform a of actions, such as view data or reset graphs. When the users click on the “file” button, they are able to select any image file within the file directory that can be added to the list box below to be selected (see Figure 10).



Figure 10. The “file” button and image selector listbox.

A “data results” static textbox was added to the control panel. This box is used to view the data of the image currently selected in the list box. This allows the user to see the data being plotted or selected. Additionally, Figures 11 and 12 show how users can view the data being plotted in Notepad by going to the toolbar and selecting the data. A reset button was added to the control panel to allow users to reset the current graph back to a blank state. This button does not reset all the graphs at once, so users can erase one graph at a time. The amplifier button located on the toolbar can be used to generate a Smith chart. After the button is selected, users are taken through a wizard-style setup to select what type of Smith chart they would like to generate. This feature is extremely useful, because it allows users to create different types of Smith charts that may be hard to duplicate using the Smith chart located on the GUI (see Figures 13 and 14).

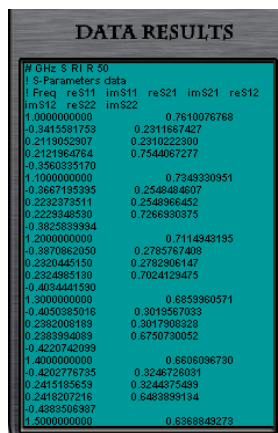


Figure 11. The “data results” static textbox.

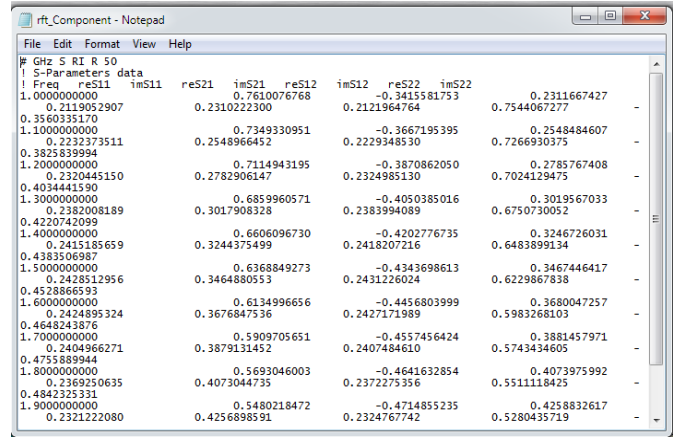
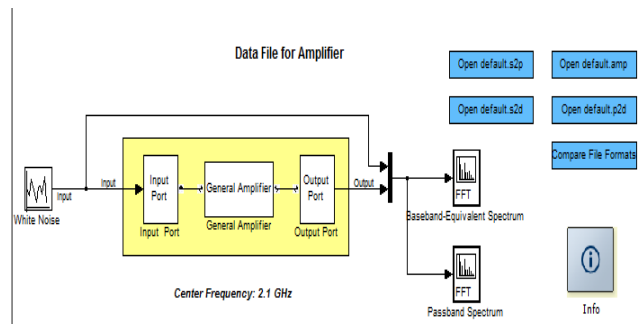
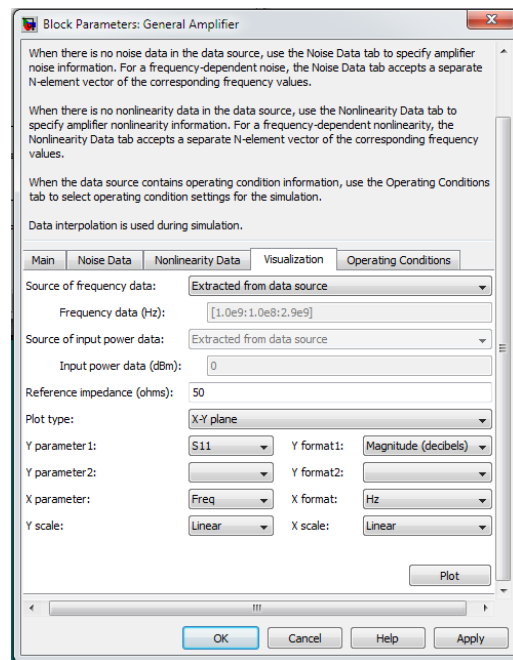


Figure 12. Data displayed in Notepad after using the “data” function.



(a) Step #1.



(b) Step #2.

Figure 13. The amplifier process.

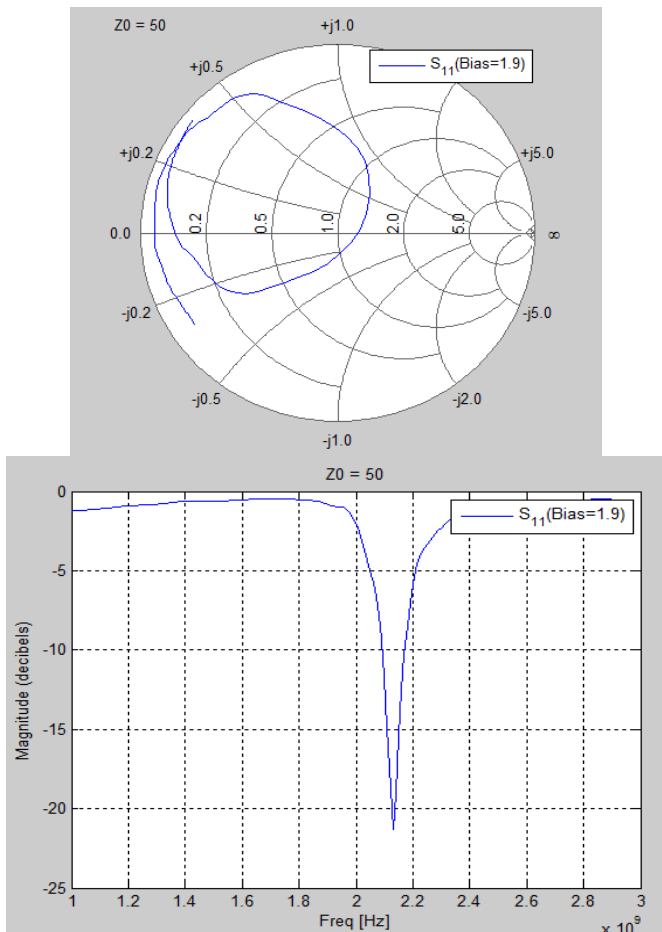


Figure 14. Results of the amplifier generator.

The angular average function was also added to the toolbar. Figure 15 shows how this function plots various polar plots and saves them to the file directory. A help menu was also added to the toolbar. Here, users can access help using the GUI through demos and help menus. In addition to finding help, users can obtain contact information for the help desk.

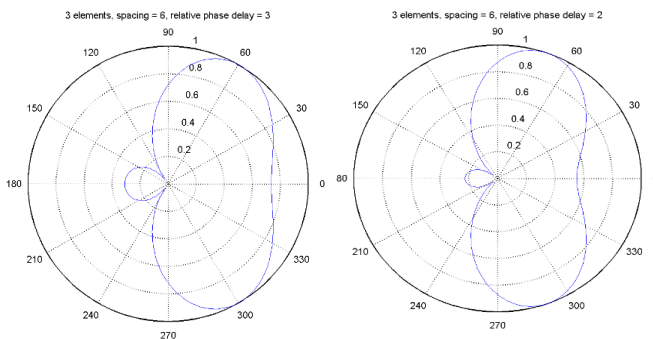


Figure 15. The angular average of some random data.

## Conclusions and Future Work

This project was extremely successful. The most prized accomplishments throughout this entire experience was the comprehensive set of features for manipulating and displaying data and the custom background that worked well with all of the functions. The plan for future work is to take the code written in MATLAB, create an iPhone/iPad-compatible app that could do the same thing that this GUI did, and enable users to accomplish these tasks from an iPad or iPhone.

## Acknowledgments

This research was funded by 2010 and 2011 NASA CI-PAIR and NASA NSTI Research Grants, and supported by Goddard Space Flight Center and NASA Langley Research Center. We would like to thank the NASA team of collaborators lead by Dr. Deshpande and our colleagues at Virginia State University for their time and thoughtful insights during *ad hoc* research gatherings. In addition, the authors wish to extend their gratification to the anonymous reviewers for their time, assistance, and patience.

## References

- Badombena-Wanta, S., & Sheybani, E. O. (2010). Mobile communications for development: Enabling strategic and low-cost e-applications for rural and remote areas. *Proceedings of Wireless Telecommunications Symposium*. Piscataway, NJ: IEEE. doi: [10.1109/WTS.2010.5479644](https://doi.org/10.1109/WTS.2010.5479644)
- Bonsiepe, G. (1989). Interpretations of human user interface. *Visible Language*, 24(3), 262-285.
- Hayes, F., & Baran, N. (1989, July). A guide to GUIs. *Byte*, 4, 250-257.
- Garcia-Otero, S., & Sheybani, E. (2010). Engineering senior design course ("new and improved"). *Proceedings of ASEE Annual Conference*. Washington, DC: ASEE.
- Gawa, A. (2006). *Smith chart*. Retrieved from <http://amanogawa.com/archive/docs/G-tutorial.pdf>
- Hardy, M., Javidi, G., Denton, L., Campbell, Y., & Sheybani, E. (2007). Enhancing research capacity and developing wireless communications curriculum for students in computer science and engineering. *Proceedings of IEEE/SECon 2007*. Piscataway, NJ: IEEE. doi: 10.1109/SECON.2007.342995
- Interface. (2019). *Business Dictionary*. Retrieved from <http://www.businessdictionary.com/definition/interface.html>
- Javidi, G., & Sheybani, E. (2008). Content-based computer simulation of a networking course: An assessment.

- Journal of Computers*, 3(3), 64-72.
- Javidi, G., & Sheybani, E. (2010). Making youth excited about STEM education. *Journal of Computing Sciences in Colleges*, 26(1), 140-147.
- Norman, D. (1988). *The psychology of everyday things*. New York: Basic Books.
- Ouyang, Y., Yang, S., Franklin, T., Michaelson, K., Morge, S., Sheybani, E.,...Narayan, S. (2010). Games, sims, and virtual worlds in K-20 STEM education. *Proceedings of 21st International SITE Conference*. Chesapeake, VA: Association for the Advancement of Computing in Education.
- Sheybani, E., & Arora, K. (1993). Measurement of temporal coherence of underwater optical scattered field. *Microwave and Optical Technology Letters*, 6(2): 151-154.
- Sheybani, E., & Sankar, R. (2002). Integrated network architecture and signal processing for telemammography. *Proceedings of IEEE/ICASSP*. Piscataway, NJ: IEEE.
- Sheybani, E., & Javidi, G. (2006). Visualization effects in virtual engineering labs II. *Proceedings of IEEE/FIE*. Piscataway, NJ: IEEE.
- Sheybani, E. (2011). Dimensionality reduction and noise removal in wireless sensor networks. *Proceedings of 2011 4th IFIP International Conference on New Technologies, Mobility and Security*. Piscataway, NJ: IEEE. doi: 10.1109/NTMS.2011.5721151
- Sheybani, E., & Javidi, G. (2007). Development and evaluation of an educational computer network software. *Proceedings of IEEE/SECon 2007*. Piscataway, NJ: IEEE. doi: [10.1109/SECON.2007.342904](https://doi.org/10.1109/SECON.2007.342904)
- Sheybani, E. O., Mengshoel, O. J., & Poll, S. (2010). Removing spikes while preserving data and noise using wavelet filter banks. *Proceedings of IEEE Aerospace Conference*. Piscataway, NJ: IEEE. doi: 10.1109/AERO.2010.5446821
- Sheybani, E., Garcia-Otero, S., Adnani, F., Javidi, G., & Deshpande, M. (2012). An algorithm for real-time blind image quality comparison and assessment. *International Journal of Electrical and Computer Engineering*, 2(1). doi: <http://dx.doi.org/10.11591/ijece.v2i1.112>
- Varde, A., Rundensteiner, E., Javidi, G., Sheybani, E., & Liang, J. (2007). Learning the relative importance of features in image data. *Proceedings of IEEE ICDE's DBRank-07*. Piscataway, NJ: IEEE. doi: [10.1109/ICDEW.2007.4400998](https://doi.org/10.1109/ICDEW.2007.4400998)
- Zhou, Y., & Chen, Y. (2008). Properties of mixed-mode S-parameters. *Microwave and Optical Technology Letters*, 50(11), 2869-2874.

## Biographies

**EHSAN SHEYBANI** earned his BS, MS, and PhD in electrical engineering from UF, FSU, and USF respectively. His main research area is applications of communication, signal processing, and data analysis. He has been involved in teaching, practicing, researching, and consulting applications of DSP in technology, system analysis, and data sciences for the past 20 years. He has a long list of publications and research grants, including projects with NASA, NSF, NIH, DoD, DED, and industry partners. Currently, he serves as a faculty member at the University of South Florida. Dr. Sheybani may be reached at [sheybani@usf.edu](mailto:sheybani@usf.edu)

**GITI JAVIDI** earned her BS from the University of Central Oklahoma and MS and PhD from the University of South Florida. Her main research area is human computer interaction, data visualization, and STEM education. She has been involved in teaching computer science and conducting research in that area for the past 16 years. Dr. Javidi has a long list of publications and research grants, including projects with NASA, NSF, MSIP and industry partners. Currently, she serves as a faculty member at the University of South Florida. Dr. Javidi may be reached at [javidi@usf.edu](mailto:javidi@usf.edu)

# A DIAGNOSTIC CLOCK FOR VERIFICATION OF IMAGE TIME SYNCHRONIZATION

Curtis Cohenour, Ohio University

## Abstract

The GPS clock is a diagnostic tool for measuring time synchronization errors in aerial surveillance systems. Aerial surveillance systems are used in many civilian and military applications, including law enforcement, border security, military situational awareness, and military forensics. The goal is to collect images and project them onto the local terrain such that the images form a map. A common example is Google Earth. Aerial platforms can include drones, fixed or rotary winged aircraft, and lighter-than-air vehicles. An aerial surveillance system consists of an imaging system and a navigation system. The navigation system is used to determine the camera position and attitude, known as the pose, which contains the necessary information required for the projection of the image onto the terrain. The images and pose come from two sources and must be synchronized. Any error in the synchronization will create a projection error.

One method of determining when an image has been captured is to take a picture of a clock. The GPS-synchronized clock creates a display of the GPS time that can be recorded in an image. By taking images of the clock using the surveillance system, each image will have a true time from the image of the GPS clock and a time derived from the pose. If the synchronization is correct, they will match. Any difference between the clock time from the image and the time from the pose is an error that must be corrected. In this paper, the author describes the operation, testing, and accuracy of the clock. Tests were performed using an independent GPS receiver and a precise time protocol (PTP) server. The resolution of the clock was 1 millisecond (ms), and the accuracy was 0.1 ms. Case studies describe how the clock is used to discover and subsequently correct timing errors in a surveillance system.

## Introduction

Aerial surveillance is used in many civilian and military applications, including law enforcement (Ersoy, Palaniappan, Seetharaman, & Rao, 2012), border security, and improved situational awareness (Bryant, Johnson, Kent, Nowak & Rogers, 2008). The goal is to collect images and project them onto the local terrain such that the image forms a map. A common example is Google Earth (GE), where, for example, the image of a road overlays a map of the road.

Images are captured by a camera, while the pose is most often generated by an integrated global positioning system (GPS)/inertial measurement unit (IMU). Distortion in the camera image and errors in the GPS/IMU will result in errors in the projection. These errors have been studied in detail and are well documented in the literature for camera models (Cohenour, Price, Rovito, and van Graas, 2015) and corrected pose data (Cohenour, Price, Rovito, & van Graas, 2015). The assumption was made that the pose would be synchronized with the image, as the author was unable to find research into projection errors caused by time synchronization errors nor any device to measure these errors. It was also assumed to not always be true that an image is synced with the pose, as will be seen in the case studies below. In this paper, the author describes a means of testing this assumption.

The pose, by default, includes an accurate time. If the image includes the time, the two can be compared directly. The GPS clock provides a mechanism for including the time in the image. The clock was used as a diagnostic tool. Data were collected and analyzed, and the results used to diagnose, correct, and ultimately verify the synchronization of the image and the pose. The details of the projection are described in a number of papers for camera models (Cohenour et al., 2015), corrected pose data (Cohenour et al., 2015), and others (Wolf, 1974; Tsai, 1987; Di & Li, 2004). The projection is based on the camera pose (position and attitude) that corresponds to the image. The pose will have random errors that generate random errors in projection. For example, errors in GE can range from a few centimeters to a few meters, depending on the aerial survey used. In this current study, the focus was on errors that occurred because the pose data were not captured at the same time the image was captured.

The pose data typically come from an integrated GPS IMU, while the image data come from a camera or a bank of cameras. The pose and image data are placed in one-to-one correspondence. But what happens if there is an extra message in the IMU buffer or the image buffer? If this happens, then the images will be off by one or more frames. GPS is a four-dimensional positioning system; it produces position in three dimensions and time. The position errors are typically less than 10m (Kaplan, 1996). A 10m error in time is  $10\text{m}/300\text{e}6\text{m/s} = 33\text{ns}$ . An aerial surveillance camera typically operates with an integration time of 1ms. If an aircraft is traveling at 85m/s then the 1ms is 0.85 of aircraft travel.

The GPS time is available for free with an accuracy much greater than that needed for image time registration. This provides an opportunity for verifying the synchronization of the pose and the image. If there is an accurate clock in the image, the clock time can be compared with the GPS time in the pose. If they match, the synchronization is confirmed. If they do not match, then hardware or software modifications are required.

## GPS Clock Version 1

The original clock, Version 1, was not designed specifically for testing image synchronization and so was modified for this purpose. The clock displayed the minutes and seconds with six gray code bits (Dewar & Stevens, 2012) and milliseconds with 10 gray code bits. Two additional indicators were also displayed. The first indicated a valid display, labeled “GPS Ok”; the second indicator changed state each time the GPS receiver time sync pulse was received and was labeled 1 pulse per second (1PPS). Gray code was used in the clock because only one bit changes at a time. If binary were used, the transition from 7 to 8, which in binary is  $0111_b$  to  $1000_b$ , could be read as  $0000_b$ , or  $1111_b$  which would be 0 or 15 in decimal. Version 1 of the clock had a number of issues:

1. Heavy, about 35 pounds
2. Separate gray code displays for minutes, seconds, and milliseconds
3. No diagnostics for the GPS receiver
4. No way to test the LEDs and drivers
5. Second update occurs 20ms after the 1PPS
6. LEDs are dim
7. Requires 120V alternating current (AC) power
8. Satellite tracking issues

While 35 pounds is not prohibitively heavy, the clock was awkward, hard to carry, and sometimes used in areas inaccessible to autos. The clock did not operate on batteries, which could cause issues in remote locations. The separate gray code displays for minutes, seconds, and milliseconds meant that multiple bits would sometimes change at the same time. If the change occurred while the exposure was being made, this would create errors, since the second update was 20ms late. The milliseconds must be read first and then the seconds adjusted. With no receiver diagnostics, simple problems like a bad antenna cable could not be diagnosed. There was no way to test for a bad LED or driver. The LEDs were not bright enough for use outdoors in the sun or with a short, 0.1ms integration time. Finally, receiver tracking was optimized for survey work and would not track satellites that were not clearly visible. This led to trouble getting a solution, if the antenna did not have a clear view of the sky.

## GPS Clock Version 2

Version 2 of the clock resolved all of the aforementioned issues (see Figure 1). The clock was lightweight, designed for remote use, included diagnostics, and worked well in direct sunlight. There were test buttons for the LEDs, a liquid crystal display (LCD), and a diagnostic RS-232C port.

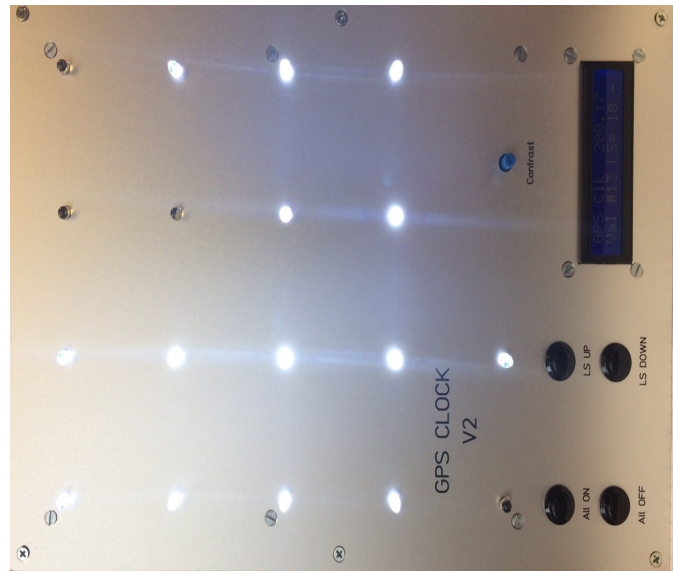


Figure 1. The GPS clock version 2.

The GPS clock version 2 used an Arduino Mega 2560 R3 as the computing platform. The Arduino Mega (2017) had four serial ports, 54 digital input/output (IO) ports, and multiple hardware and software interrupts. The GPS receiver was manufactured by ITEAD and used a RoyalTek REB-4216 chip. The receiver tracked reflected satellites, operated with a limited view of the sky, and could often generate a solution indoors. The receiver was selected because it was the only GPS Arduino shield (at the time of writing) with a 1PPS output. All of the receiver outputs were echoed to an RS-232 serial port for diagnostics.

The LED outputs were buffered, generating an intense white light of 12,000 mcd. The LEDs could easily be seen in bright sunshine. A felt cover was provided to eliminate reflections when operating in direct sun. The LEDs, IO pins, and buffers could be tested using two buttons, “all on” and “all off.” The time display was 16 bits with 10 bits dedicated to the fraction. All 16 bits were a single gray code word. This complicated manual decoding but ensured that no more than one bit changed at a time. The fraction was 10 bits; therefore, the resolution was  $2^{-12}$ , 1/1024th of a second, or 0.9766 ms. The resolution was approximately 1ms, which was adequate for an airborne imaging system that typically has a minimum exposure time of 1 or 2ms.

GPS time was kept in seconds of the week starting with 0 at 0:00:00 coordinated universal time (UTC) on Sunday. The six most significant bits of the LED display showed the GPS time modulo 64. There are 86,400 seconds in a day, so  $86,400/64$  is 1,350 with a remainder of zero. This happy coincidence ensured that there would be a continuous rollover over each day and each week. The aerial surveillance system was assumed to have a time error of less than 32 seconds. This could be verified with a single frame of data and a watch. Assuming that the system met this requirement, the error would be at most a few seconds, and a modulo 64 second clock would be adequate.

An LCD was provided on the clock. The LCD displayed the clock version, valid/invalid, the number of satellite vehicles (SVs) tracked, the leap second, and a graphic indicating serial data received. The number of SVs tracked was a key piece of troubleshooting data, as was the serial data graphic. The GPS receiver sent out six National Marine Electronics Association (NMEA) messages. The Arduino decoded two of these messages to extract the time of day, valid/invalid, and the number of SVs. All of the messages were echoed to a serial port on the left side of the clock for user diagnostics. Finally the clock was lightweight, only 3.5 pounds, 8"x12"x3", with a carry handle, and powered by six AA batteries or an AC adapter. The clock and accessories were shipped in a small Pelican case.

## Hardware and Software

Figure 2 shows a hardware block diagram of the GPS clock. The ITEAD GPS receiver sends serial data to the Arduino Mega via serial port 2. The baud rate is 9600 with eight data bits, one stop bit, and no parity. These data are converted to RS-232 signal levels using a MAX-232-CPE, and outputted to a 9-pin d-shell serial port. The 1PPS signal is routed to the Arduino on pin 2, interrupt 0. The Arduino processes the data and outputs to 18 LEDs, which are connected to three SN74LS07 hex buffers and drivers with open-collector high-voltage outputs (Texas Instruments, 2016). The LEDs are connected to the battery or AC adapter and do not draw power through the Arduino voltage regulator. There are 16 LEDs for the time display, one for the 1PPS, and one for the valid indicator. The Arduino drives a backlit LCD display. There is an analog contrast adjustment for the LCD.

There are four button inputs to the Arduino: lamp test buttons “all on” and “all off” and leap second “up” and “down.” The lamp test buttons override the normal LED outputs and verify the Arduino output, the buffer, and the LED. Not shown is the power. A switched barrel jack disconnects the batteries when the AC adapter is connected.

An on-off switch connects the power to the clock. The clock can operate for about two hours on six AA batteries. An SMA female connector is provided on the left side of the clock for connection to an amplified 3.3V GPS antenna. Figure 3 shows a software block diagram for the clock, which is interrupt-driven. The 1PPS event sets the seconds of the day based on the input from the serial parser and zeros out the 1/1024-second timer. This starts the 1/1024-second counter at zero on the 1pps event. From here on, the 1/1024-second clock increment will be referred to as 1 ms for brevity.

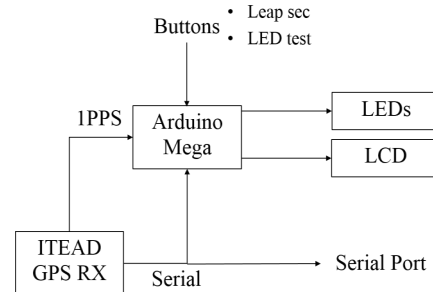


Figure 2. GPS clock version 2 hardware block diagram.

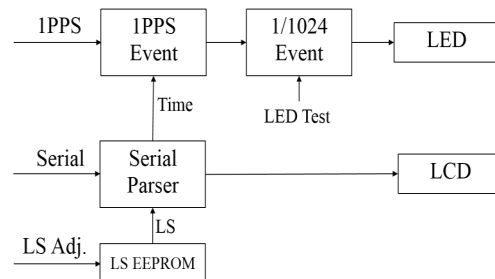


Figure 3. Software block diagram of the GPS clock.

The ITEAD receiver generates six NMEA output messages. The serial parser reads and parses the recommended minimum data (RMC) and global positioning system fixed data (GGA) messages, other messages are not parsed to reduce processor load. All messages are passed via hardware to the diagnostic serial port. The RMC message is parsed to extract the UTC time and the valid flag. The GGA message provides the number of SVs in the solution. The seconds of the day (SOD) is computed based on the hour, minutes, and seconds in the RMC message. The RMC message completes 750 ms into the seconds and is one second old at the time of the next 1PPS. The leap seconds are added to the SOD to convert UTC SOD to GPS SOD. The GPS SOD is all that is needed for the clock, because the seconds in a day, 86,400, is an even multiple of 64. During the 1PPS event, if the time is valid, the clock is reset to the  $(\text{SOD GPS} + 1) \text{ modulo } 64$ , the milliseconds is set to zero, and the millisecond timer, timer 2, is set to zero.

The 1/1024 event is tied to timer 2. The timer pre-scaler is set to 64. The clock is 16 MHz so the timer counts at 250 KHz. The counter should time out at  $250,000/1024-1=243.1406$ . The timer is set to 243, and the remainder, 0.1406, is accumulated until it is greater than 1.0. When this happens, one is subtracted from the accumulator, and the timer is set to 244. In this way, the clock remains accurate. If this were not done, then the last millisecond, 1023, would be over four milliseconds long. This is further complicated by the inaccuracy of the Arduino clocks. The clock was tested with three different Arduinos to investigate the variability in the oscillators. The average number of microseconds per 1PPS was  $1e6$  for a perfect oscillator. The results for the three units tested were 992,592, 1,001,216, and 1,000,002. The GPS 1PPS had an error of less than  $1\mu s$ , so it could be used to calibrate the Arduino internal oscillator. To compensate for the oscillator errors, the average value of the microseconds per 1PPS was divided by four and used in the above calculation instead of 250,000.

The REB 4216 receiver does not reveal the leap second. To convert from UTC to GPS the leap second is needed. The current leap second is 18 as of August, 2017, and can change twice per year during the first week epoch in January and the first week epoch in July. The current leap second is officially available on line at <https://www.navcen.uscg.gov> but is more easily found by doing a Google search for “GPS leap seconds.” The conversion is given by Equation 1 [IS-GPS-200]:

$$GPS = UTC + \text{Leap seconds} \quad (1)$$

where, GPS is the seconds of the week in GPS time; UTC is the seconds of the week in UTC; and, Leap seconds is the integer number of leap seconds.

The leap second was stored in a EEPROM and manipulated by two buttons, “up” and “down.” When the leap second was changed, it was stored in the EEPROM. During startup, the EEPROM was read to initialize the leap seconds. The LED test buttons were implemented in the 1/1024 event. During this event, the seconds and milliseconds were computed as well as the status of the valid and 1PPS LEDs. The seconds and milliseconds were converted to gray code. If neither LED test button was pushed, the data were placed on the Arduino IO ports. If the “all on” button was pressed, the IO ports were set to on; if “all off” was pressed, then the IO ports were set to off. In this way, the IO ports, the buffers, and the LEDs were tested. Data displayed on the LCD included the GPS clock software revision on the top line and key data on the second line. The second line of the display included “val”/“inv” to indicate the status of the clock, the number of satellites, the number of leap seconds, and a ro-

tating slash to indicate that the GPS messages were being received.

## Verification

Accuracy of the GPS clock was verified in a number of ways. First, the 1PPS signal was checked against a Novatel survey receiver; second, a precise time protocol-enabled camera (Kaplan, 1996) was used; and, third, a Novatel receiver was used. Figure 4 shows a histogram of the error collected from 31,521 images.

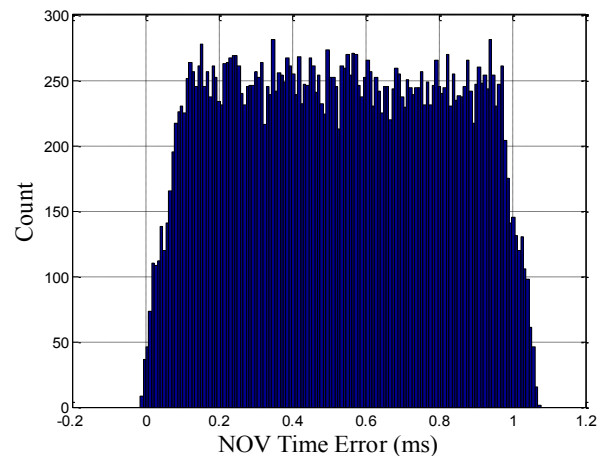


Figure 4. Histogram of clock errors (31,521 measurements).

The first test conducted was to determine the accuracy of the 1PPS interrupt. A NovAtel PWRPAK-4-3151W P/N: 01016783 was connected to an AeroAntenna AT575-9W-TNCF-000-05-26-NM amplified antenna. The 1PPS was connected to the Arduino interrupt 0, IO pin 2. The interrupt routine was set up to toggle the 1PPS LED on the Arduino. The Arduino output was connected to the NovAtel Event1 input. The NovAtel “MarkTime OnNew” log (Novatel, 2015) was used to determine the interrupt delay. This test showed a delay of  $11\mu s$ , which is the time required to process the interrupt. Figure 5 shows how the second and third tests were set up. Table 1 provides descriptions of the components.

The camera was powered using power over Ethernet (POE). Communications and control of the camera was by gigabyte Ethernet. A PTP (IEEE, 2008) time server was connected to the camera to provide microsecond-level absolute time to the camera. In this configuration, a console application running on the laptop triggered and recorded 10 images about 0.8 seconds apart. Each image was saved using the PTP time in microseconds. The PTP time is Temps Atomique International (TAI) seconds since January 1,

1970 (McCarthy & Seidelmann, 2009). TAI is always ahead of GPS by 19 seconds (Time Service Dept., n.d.), and can be determined using Equation 2:

$$GPS = PTP + 19s \quad (2)$$

where, PTP is seconds since January 1, 1970.

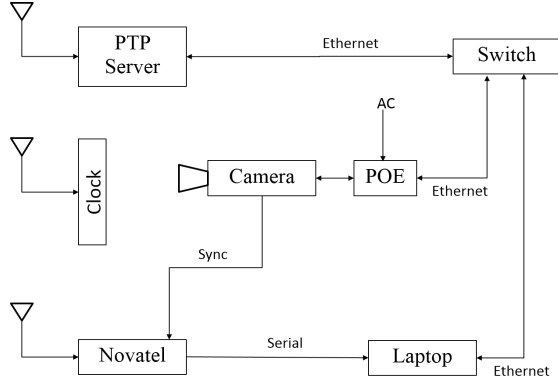


Figure 5. Test configuration for the clock.

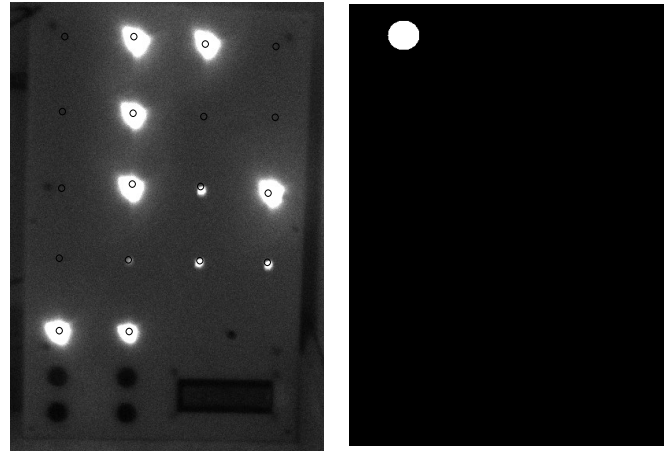
Table 1. Equipment used for clock testing.

Item	Description
Camera	Allied Vision Manta G-319B
Novatel	Novatel PWRPAK-4-3151W P/N: 01016783
PTP Server	Time Machine TM2000A
Switch	NetGear ProSAFE GS108
Antennas	Generic Magnetic Base L1 Patch Antenna

PTP time synchronization in the camera is known to be within  $2 \mu s$  (Allied Vision, 2016). If the PTP time from the camera is correct, then this would be all that is required to validate the clock readings to the millisecond. To check the camera PTP time, the sync 1 output of the camera was tied to the Event 1 input of the Novatel. Using MATLAB, the console app was executed, and the file names/PTP times were extracted. The Novatel logs were collected and the time extracted. Each image was read, and the first 20 bytes of the image were replaced with the GPS time from the Novatel receiver. This was done 10 images at a time to ensure that there were no buffering errors. Later, when processing the images, the PTP time was extracted from the file name and the GPS time was extracted from the image.

Other items in the test setup included a NetGear Ethernet switch and Cat. 5E Ethernet cables. This set up was used for all of the results in the following section. Tests were conducted with the lens aperture at max, an exposure time of

0.1 ms, and a gain of 35 dB. This produced images having an exposure much shorter than the resolution of the clock. Figure 6(a) shows that the LEDs and clock were clearly visible. Figure 6(a) also shows image one of 31,521 images used to verify the clock accuracy. The images were processed automatically using MATLAB. First, the location of the LEDs was captured. This was done by displaying image one and clicking on each of the 18 LEDs. The location of the LEDs was saved and indicated by circles in Figure 6(a). Once this was completed, the LED locations could be used for all images, as long as the clock and camera were not moved.



(a) The first of 31,521 images used for clock verification.

(b) Mask for bit G15.

Figure 6. The LEDs and clock are clearly visible.

For each image, the LEDs are read as follows: a mask is generated for each LED position with a value of one within a radius of pixels. Figure 6(b) shows the mask for LED G15. The mask and the image are multiplied element by element, and the results are summed. This gives a low value for an LED that is off, and a high value for an LED that is on. This is repeated for each of the 16 gray code LEDs, the 1PPS, and the valid LED. A threshold value is chosen midway between on and off to differentiate the two states. In this way, the 16 gray code bits are extracted. This is done for each image. The gray code values for each image are converted to seconds using Equation 3. Note that the clock reading is, by definition, modulo 64.

$$ModGPS = \frac{gry2int(Gry)}{1024} \quad (3)$$

where, Gry is the clock reading in gray code; gry2int(\*) converts \* in gray code to an integer; and, 1024 converts clock increments to seconds.

\* Additional MATLAB scripts are available from the author (see contact information included with this paper).

The MATLAB code for this conversion is:  
`decGPS=gray2int(Gry);`  
`ModGPS=decGPS/1024;`

When in use, it was assumed that the clock was correct so the error was the time stamp—the GPS clock time in the image. The time stamp error can be computed using Equation 4:

$$\begin{aligned} \text{ModTimeStamp} &= \text{mod}(\text{TimeStamp}, 64) \\ \text{Err} &= \text{ModTimeStamp} - \text{ModGPS} \\ \text{if } (\text{Err} < -32), \text{Err} &= \text{Err} + 64 \end{aligned} \quad (4)$$

where, *TimeStamp* is the time stamp in GPS time; *mod*(a, b) returns the remainder of a/b; and, *Err* is the clock error.

Note that the “if” statement compensates for events where the *ModGPS* and the *ModTimeStamps* occur on opposite sides of the 64 second boundary.

Using the setup above, the clock distribution was 0.5 ms  $\pm$  0.3 ms, as seen in the histogram of Figure 4. The camera was triggered asynchronously so that the errors should form a uniform error distribution in Figure 4. Theoretically, the distribution of the error should be a uniform distribution with a mean of 0.5 ms, and standard deviation of 0.28 ms (Miller & Freund, 1977), which is very close to the measured values of 0.5 for the mean and 0.3 for the standard deviation. The clock resolution was 1 ms, while the actual accuracy is better than 0.1 ms. To understand why, examine what happens to images taken at various times A through D in Figure 7. The clock reads 0.000 in the range 0.000 to 0.001, and 0.001 in the range from 0.001 to 0.002. An image taken at B will have a time stamp of 0.0011, but the clock will read 0.001, and the error is 0.1 ms. The same applies for C, where the error is 0.9 ms. The image taken at A has a time stamp of 0.00047, and the clock reads 0.000 so the error is 0.47 ms. All of the errors will map into the range of 0 to 1 ms.

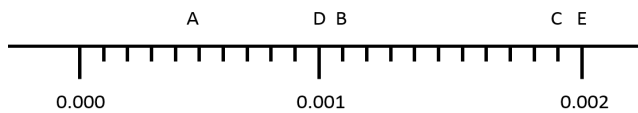


Figure 7. Timeline showing various image capture times.

Now consider the image at D. This time stamp is 0.001 but the clock could be in transition and read either 0.000 or 0.001. If the clock reads 0.000 then the time error for D is 1 ms. If the clock reads 0.001 then the time error reads 0. So the image at D could have an error of 0 or 1 ms. The same argument can be made for the image taken at E. This is illustrated in Figure 8. Note that most of the images occur between B and C. Since they are random in time, they map

to a uniform distribution with an error between 0 and 1 ms. The points at D and E may map to 0 ms  $\pm$  a few microseconds, or to 1 ms  $\pm$  a few microseconds. The result is the plot in Figure 4. The camera integration time is 0.1 ms for the data collected in Figure 4. This results in a few observations in the range of 1.00 to 1.07 ms.

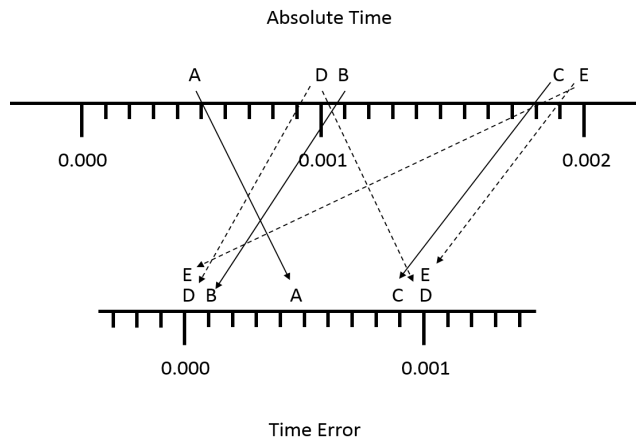


Figure 8. Mapping of image times to error space.

The GPS clock has an LED to indicate that the clock is valid. The clock may go to invalid if the GPS solution is corrupt due to jamming, an antenna failure, poor visibility of the sky, or other reasons. If this happens, the valid LED should turn off. To test this, the clock was allowed to sync to GPS time. Data recording was started, and the GPS antenna was disconnected. After a period of time, the antenna connector was reconnected, and the clock synced. The data were checked and the invalid state started almost immediately when the antenna was disconnected. When the antenna was reconnected, the time recovered and the clock returned to valid. All measurements with the valid indicator on were correct. For accuracy, the imaging system should be set for a short integration time. The recommended exposure time is 0.1 ms to extract maximum accuracy from the clock. This can usually be achieved by setting the integration time 0.1 ms and increasing the gain. The clock does not have to be visible, as long as the LEDs can be seen in the image. An underexposed image will work because the LEDs are very bright. If a longer exposure time is used, the results will be smeared, but the results are still meaningful. Some systems using webcams, for example, do not allow the user to control the exposure. This is illustrated in the two tests that follow.

Two tests were performed using 1 ms and 2 ms integration times. For a 1 ms exposure with 1,661 images, the mean is 67  $\mu$ s and the standard deviation is 0.6 ms, or 0.0  $\pm$  0.6 ms. For a 2 ms exposure with 3,701 images, the mean is -0.4ms, with a standard deviation of 1.0 ms.

---

## Case Studies

Version 1 of the clock was developed in 2009 and used to troubleshoot, fix, and, ultimately, verify a number of systems. Case studies are provided here to give the reader an appreciation of how time sync errors can arise and how the clock can be used to investigate and correct the any synchronization errors. Seven case studies are listed in Table 2. Some of these cases were investigated thoroughly and documented in publications; in others, the results were transmitted and results were never communicated to the author.

Table 2. Table of case studies using the clock.

Case	Description
1	Incorrect Novatel Log
2	Novatel Log Error
3	DC 3 Camera System
4	DC 3 PTP System
5	Hi Rate Data Collection
6	1/2 frame error
7	Forward Looking EO and IR

Case 1: The Novatel “InsPva OnMark” log was used, but this log was not supported by Novatel. There was an interpolation error that returned the position and attitude at the wrong time. The correct log is the “Mark1Pva OnNew” log. There is a -10 ms error in the “InsPva OnMark” log that reaches as high as 50 ms near the one-second boundary. This indicates that perhaps the Novatel has housekeeping chores on the one-second boundary that create issues with the unsupported log.

Case 2: The system was switched to use the “Mark1Pva OnNew” log. This created additional problems with yaw errors from IMU. Knowing the time tags were correct led to an examination of the errors. Based on this test, it became clear that the “InsPva OnMark” log has errors that cannot be explained. Novatel was contacted, and the user was advised to do a firmware update. This corrected the error.

Case 3: A nadir (down looking) camera system mounted on the Ohio University Avionics Center DC-3 was tested using the clock. The system had zero time errors, and no modifications were required.

Case 4: Two independent nadir camera systems were mounted on the Ohio University Avionics Center DC-3. Both of these systems used Allied Vision PTP cameras.

Both systems were tested using the clock and found to have correct time tags.

Case 5: A number of the Version 1 clock shortcomings were revealed. A 30 frames per second (FPS) with a long lens was tested using Version 1 of the clock. It was required to position the clock outside in order for the camera to capture the entire clock in the image. The sun was so bright that the LEDs could not be read. Folding tables and sawhorses were used to provide shade so that the clock could be read. The clock was placed in an area that was surrounded by buildings that obscured portions of the sky. The GPS receiver lost lock many times and slowed the data collection. Once usable data were obtained from the clock, it was discovered that the images were off by 1 to 3 frames. The system hardware included a divide-by-four circuit in the line between the camera sync and the Novatel mark input. The error occurred because the divide-by-four counter was not reset and not synced with the software. The software system was re-configured to reset the divide-by-four circuit when imaging was started. This resulted in synced images.

Case 6: An imaging system, similar to that described in Cohenour et al. (Camera, 2015) and Conehour et al. (Corrected, 2015), recorded at a rate of 3 frames per second. There was a time tag error of 0.16. The camera sync and the Novatel mark input were driven by an external time source. The error was  $\frac{1}{2}$  of the frame rate. One possible source of the error could be that the camera was triggered on the positive edge of the signal and the Novatel was triggered on the negative edge. Changing edge sensitivity of either the camera or the Novatel is trivial. The author did not receive any feedback on the resolution of this issue. This is a good example of the utility of the clock, an easily correctable problem but difficult to isolate without the clock.

Case 7: A forward-looking camera system was installed on the Ohio University Avionic Engineering Center Beechcraft Barron. The system included both IR and visible spectra cameras. A breadboard prototype of the Version 2 clock was used to test the time tagging of the visible camera. The LEDs used on the clock are not suitable for IR.

The cameras were triggered by a Novatel 1PPS signal. The software written for Microsoft Windows received Novatel position and attitude data as well as image data. The visible camera was tested and found to be off by 1 second. Software changes were made to correct this problem. The system was retested and shown to be correct. Flight data were recorded using the system. When the images were projected, there were large time synchronization errors. The data for a turn were analyzed to determine if the images matched the pose data. The horizon was tracked in a number of images to estimate the roll. The estimated roll from the

images was correlated with the IMU roll. The time error of the images was determined to be 14 seconds. This shows how buffering or other issues can cause problems. The project was shelved due to a failure of the IR camera, and the issue was never resolved.

## Conclusions

A GPS synchronized clock was described. The purpose of the clock was to measure time synchronization errors in an aerial surveillance system. Using the clock, a precise GPS time could be extracted from the image. The image time was compared to the pose time to determine the time error. Any time errors will create projection errors. With this information, corrective action can be taken. The clock described in this paper was Version 2. All of the shortcomings in Version 1 were corrected. The clock is lightweight, intensely bright, powered by AC or batteries, and includes test features and diagnostics. A detailed analysis of the timing error between the clock and a reference receiver showed that the resolution of the clock was 1 ms, while the accuracy was better than 0.1 ms. If the exposure time increased, the clock was still valid but the resolution was reduced.

The camera integration time impacted the clock readings. If the camera integration was longer than 1 ms, the least significant bit would appear as on with a 50% duty cycle. This was tested and the clock was still valid but the resolution was reduced. For best results, the minimum integration time that allows reading the LEDs should be used. A number of case studies were used to illustrate the utility of the clock. These case studies illustrate the types of errors that can be encountered, and how corrective action can be taken once the errors are discovered. The clock presented here was for visible light. There was also a need for time verification of infrared (IR) image data. The clock could easily be converted to cover shortwave IR images simply by using IR LEDs. This becomes more complex at longer wavelengths. A number of schemes are being considered for wavelengths up to 8  $\mu\text{m}$ . Additional information about the clock and ongoing work is available from the author.

## References

- Allied Vision. (2016). *Application note, IEEE 1588 precision time protocol, prosilica GT, GC and manta cameras*. Vancouver, British Columbia, Canada: Allied Vision.
- Arduino. (2017). Arduino Mega 2560. Retrieved from <http://www.arduino.org/products/boards/arduino-mega-2560>
- Bryant, M., Johnson, P., Kent, B. M., Nowak, M., & Rogers, S. R. (2008). *Layered sensing: Its definition, attributes, and guiding principles for AFRL strategic technology development*. Wright-Patterson Air Force Base, OH: Sensors Directorate Air Force Research Laboratory.
- Cohenour, C., Price, R., Rovito, T., & van Graas, F. (2015). Camera models for the Wright Patterson Air Force Base (WPAFB) 2009 wide area motion imagery (WAMI) data set. *IEEE Aerospace & Electronic Systems Magazine*, 30(6), 4-15.
- Cohenour, C., Price, R., Rovito, T., & van Graas, F. (2015). Corrected pose data for the Wright Patterson Air Force Base (WPAFB) 2009 wide area motion imagery (WAMI) data set. *SPIE Journal of Applied Remote Sensing*, 9(1), 4-15.
- Dewar, M., & Stevens, B. (2012). *Ordering block designs—Gray codes, universal cycles and configuration*. New York: Springer.
- Di, K., & Li, R. (2004). CAHVOR camera model and its photogrammetric conversion for planetary applications. *Journal of Geophysical Research*, 109(E04004), 1-9.
- Ersoy, I., Palaniappan, K., Seetharaman, G. S., & Rao, R. M. R. (2012). Interactive target tracking for persistent wide-area surveillance. Interactive target tracking for persistent wide-area surveillance. *Proceedings of SPIE Conference on Geospatial InfoFusion II*. Bellingham, WA: SPIE. doi: 10.1117/12.920815.
- IEEE. (2008). *IEEE standard for a precision clock synchronization protocol for networked measurement and control systems*. Retrieved from <http://standards.ieee.org/>
- Kaplan, E. D. (1996). *Understanding GPS: Principles and applications*. Boston: Artech House.
- McCarthy, D., & Seidelmann, K. (2009). *Time: From earth rotation to atomic physics*. Weinheim, Germany: Wiley-VCH.
- Miller, I., & Freund, J. (1977). *Probability and statistics for engineers*. Englewood Cliffs, NJ: Prentice-Hall.
- NovAtel. (2015). *OEM6 family firmware reference manual OM-20000129, rev 8*. Calgary, Alberta, Canada: NovAtel.
- Texas Instruments. (2016). *SN74LS07 hex buffers and drivers with open-collector high-voltage outputs*. Dallas: Texas Instruments.
- Time Service Dept. (n.d.). *Leap seconds*. Retrieved from <http://tycho.usno.navy.mil/leapsec.html>
- Tsai, R. Y. (1987). A versatile camera calibration technique for high-accuracy 3d machine vision metrology using off-the-shelf tv cameras and lenses. *IEEE Journal of Robotics and Automation*, RA-3(4), 323-344.
- Wolf, P. R. (1974). *Elements of photogrammetry*. New York: McGraw-Hill.

---

## Biography

**CURTIS COHENOUR** is an assistant professor in the Ohio University Engineering Technology and Management Department. He received his BS degree from West Virginia Institute of Technology in 1980, MS degree from Ohio University in 1988, and PhD in electrical engineering from Ohio University in 2009. He is a registered professional engineer in West Virginia and Ohio. Dr. Cohenour has worked in industry as an electrical engineer in the areas of control systems, automation, and power. He joined Ohio University in 2002 as a research engineer working for the Ohio University Avionics Engineering Center. He has worked on projects covering a wide variety of avionics and navigation systems, such as the instrument landing system, microwave landing system, distance measuring equipment, LAAS, WAAS, and GPS. His recent work has included research with the Air Force Research Laboratory in Dayton, Ohio, aimed at understanding and correcting image georegistration errors from a number of airborne platforms. Dr. Cohenour may be reached at [cohenour@ohio.edu](mailto:cohenour@ohio.edu)

# ASSESSING THE EFFECTIVENESS OF AN AUTOMATIC DOOR LOCK SYSTEM BY DISCHARGE DETECTION TO LOWER CASUALTIES DURING AN ACADEMIC ACTIVE SHOOTER INCIDENT

Jae Yong Lee, Purdue University; James Eric Dietz, Purdue University

## Abstract

The 2018 Stoneman Douglas High School (Parkland) shooting emphasized the importance of testing active shooter responses for both first-responder communities and the general public. Since the 1999 Columbine massacre, the preparedness for active shooter incidents (ASIs) included aggressive police tactical responses to neutralize the shooting threat. Currently, the run.hide.fight. response for unarmed individuals has been implemented as part of the active shooter response for both the public and private sectors. However, despite the RHF's nationwide implementation, there are few studies in the literature to support the effectiveness of RHF. Additionally, modeling a scenario similar to the Parkland shooting suggests that the application of RHF without situational awareness of the shooter's location could cause higher casualty rates by an average of more than 1.26 individuals.

In this study, the authors compared the casualty rates of two models. The first model consisted only of hide (shelter-in-place) and run (evacuate). The second model applied the first model's components with the automatic door lock system, which was triggered by discharge detection. To exclude human participation, and to prevent physiological and psychological impact, agent-based modeling (ABM) was used to recreate a one-story academic infrastructure with 26 lecture halls and three exits containing 600 unarmed individuals. The flexibility of ABM allows multiple iterations, while manipulating various parameters. The ABM approach in active shooter research also eliminates human error and logistical issues. The outcome of this study evaluates the effectiveness of an automated door lock system, based on firearm discharge detection with a campus-wide alert system to conduct lockdown.

## Introduction

The term active shooter incident (ASI) may be a familiar term for the general public. Federal Bureau of Investigation (2016) statistics suggest that the number of active shooter incidents has risen from 7.4 (2000-2008) to 19.1 (2009-

2016) incidents per year. Additionally, 45.6% of the active shooter incidents occur in areas of commerce, and 24.4% in educational institutions. Finally, 60% of ASIs were terminated prior to the arrival of law enforcement. The increasing rate of active shooter incidents in the areas of commerce and educational institutions with short duration challenges the first responder and the civilian communities to mitigate such incidents.

Law enforcement communities have applied mitigation tactics, such as unified incident command system (FEMA, 2017), hosting school resource officers (Scott & Schwartz, 2014), and the formation of contact teams (Scott & Schwartz, 2014) to mitigate such incidents. The most common ASI response for the civilian population in both private and public sectors was "run.hide.fight" (RHF) (City of Houston, 2012). The RHF response was created in 2012 by the City of Houston under the Federal Emergency Management Agency's grant. Yet, despite the nationwide application of RHF, there is a lack of literature supporting the effectiveness of RHF to lower casualties during ASIs. Additionally, RHF cannot be applied in areas where the unarmed individuals are incapable of fighting the active shooter, such as kindergarten or elementary schools. In this study, the authors examined the casualty rates of two models. The first model represented an academic infrastructure without any preventative system. The second model applied an automated door lock system to the first model, which was initiated by the active shooters' first discharge. A campus-wide lockdown was automatically conducted among unarmed individual agents. The door lock system only prevented entry to the lecture hall, which allowed individuals to evacuate the lecture hall. Only run and hide were implemented in both models, since they assumed that the majority of unarmed individual agents were either kindergarten or elementary school students, who were limited in their ability to fight the shooter.

## Agent-Based Model

AnyLogic software consists of three major components: discrete event, agent-based, and system dynamic methods

that could be used interchangeably. For this study, the agent-based method was used predominantly to recreate active shooter incidents within the educational environment. The model consists of pedestrian and process modeling libraries, which recreates the interaction between an active shooter and the unarmed individual agents within the model.

The benefits of ABM were its ability to measure emergent phenomena and collect individual agent's interaction with other agents. Additionally, ABM can illustrate "behavior, degree of rationality, and ability to learn and evolve" (Bonabeau, 2002), which was a crucial component in measuring the cause and effect of hypothesizing what increased or decreased the casualty rate. Finally, using ABM allows active shooter research to be conducted in a safe environment by eliminating the participants' potential to experience post-traumatic stress disorder or other anxieties (DHS, 2017). Both models were based on a general floor plan for an academic institution, which was available in the public domain as a visual aid intended to support the emergency evacuation plans. The floor plan included classrooms and hallway corridors, which were converted to an image file and added to the AnyLogic software.

## Model Physical Infrastructure

The *Wall*, *Target Line*, *Service with Lines*, and *Polygonal Area* from the Space Markup section in the Pedestrian Library were used to model the physical infrastructure. The wall creates a physical barrier within the model, which limits the agent's movement. For example, if a wall is encountered by an agent within the model, the agent seeks alternative routes by moving away from the obstacle. The service with lines section can send an agent through the wall, which represents an agent passing through the doorway. The polygonal area represents lecture hall seats, where the agents remain in one location for the duration of the class. Each lecture hall consists of one attractor as a point of gathering during the lockdown phase.

## Model Agents

There were two agents in this model, an active shooter and the unarmed individuals: *State Configuration – Line of Sight (LOS)* and *State Configuration – Casualty*. Each agent carries different states in order to add flexibility to what an agent can and cannot do, depending on the location. For example, just because an active shooter's discharge range is set to 100 feet, does not mean that the shooter is capable of selecting targets through the wall of the lecture hall or agents in a different hallway section. To limit target selection of the shooter, line of sight (LOS) was modeled by placing agents into different states, depending on the loca-

tion. In Figure 1, the agent's state under green LOS is colored purple.

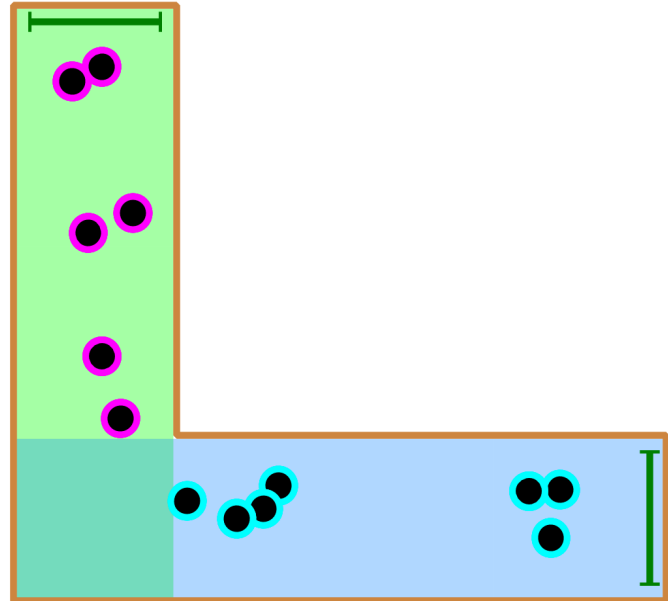


Figure 1. The change of agent's state by location.

Once the agent enters the light blue LOS, the agent's state and color change to cyan. Additionally, an agent could be under both green and blue LOS if two areas are merging. Both agents operate under this concept in order to limit target selection probability, based on the physical location, such as hallways or lecture halls. The active shooter selects the target by using a Function within the Agent Library. Each function is coded in Java, which selects the shooter target based on the LOS state, followed by the discharge range. One target could be selected per search, where the rate of each search was set to one target within a 21.2-second interval. Anklam, Kirby, Sharevski, and Dietz (2015) used the victim interval ratio by the statistics from the Patrol Response Challenges (Buster, 2008), where there was one victim every 15 seconds by averaging the 65 active shooter incidents to the number of victims. For this study, the shooter casualty interval was based on the Parkland Shooting (Fausset, Kovaleski, & Mazzei, 2018) by assessing total death count and the duration of the shooting.

The Java function was divided into three sections. The first section was the target selection among the agent's population. For instance, the shooter searches for one target among the pool of unarmed individual agents. The second section of the function entails determining the state of the potential target agent. If an agent's state was a casualty, then the function starts over to find a new target. If the agent's state was not a casualty, then the function determines whether the target was within the same LOS state as

the shooter. If the shooter and the unarmed individual were in the same state, then the function evaluates the discharge range. If the potential target does not qualify under either state, the function restarts. The third section of the function executes the act of firearm discharge to the targeted agent. The exchange of fire was modeled by sending a string message to the targeted agent. The probability of a failed message delivery was zero, since the execution would occur immediately. Once the message has been received, then the state of the target agent will change to casualty, and the speed of the agent will be set to zero and the color to red.

The agent's movement was conducted by the following blocks from the pedestrian library: *PedSource*, *PedGoTo*, *PedService*, and *PedSink*. *PedSource* determines the agent and the rate of entry from the agent to the model. For this model, there were two *PedSource* blocks, one for an active shooter and the other for the unarmed individual agents. *TargetLine* was used as an entry point, which was determined within the *PedSource* block. Once the agent exits the model by the *PedSource* block, the agent enters the *PedService* block, which allows the agent to enter the lecture hall. The *PedService* block prohibits the agent from traveling through the wall, which represents a door. Each lecture hall consists of a polygonal area, where the agent waits throughout the model runtime. Figure 2 shows how the agent's state was changed from green to either purple or yellow, based on their location.

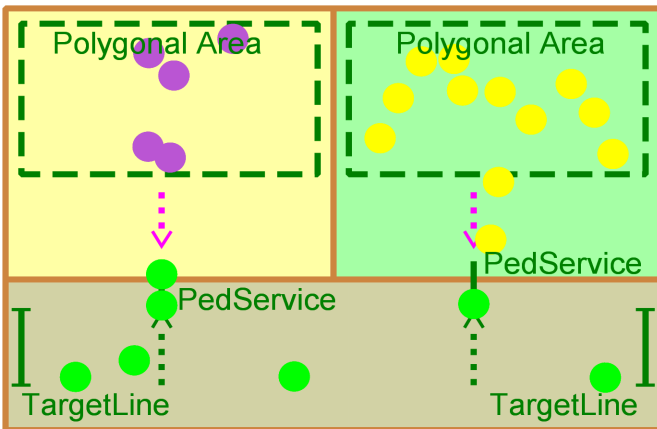


Figure 2. The change of an agent's state by location.

## Agents Logic

All 600 unarmed individual (UI) agents enter the model and move randomly toward the available lecture hall. Once an agent arrives in a lecture hall, it will remain at the randomly selected point until the shooting begins. Prior to the shooting, all 600 UI agents are distributed within the lecture halls; no UI agents remained in the hallway.

The active shooter enters the model without discharging and continues to advance down the hallway until the in-class population count reaches 600. Once all 600 UI agents are in the lecture hall, the shooter immediately begins to discharge. UI casualties will always occur in the lecture hall. The shooter's discharging function is set to one casualty per 21.2 seconds for UI agents that are in range. If there are zero potential targets within the range, the 21.2-second delays starts over. Once the active shooter agent begins shooting, the UI agents will then evacuate to the nearest exit. The shooter will attempt to randomly enter a lecture hall one after another, while running UI agents in the hallway are considered as potential targets. If the automatic door lock system is in place, the shooter will remain in the hallway until the model is terminated, while having the same ability to discharge at the running UI agents.

The automatic door lock system begins as soon as the active shooter discharges the first shot. The lock system prevents the active shooter from entering the lecture halls, while still allowing any UI agents inside to evacuate via the hallway. The shooter's discharge initiates the unarmed individual agents to either hide (shelter-in-place) or run (evacuate) from the shooter. The hide probability parameter determines what percentage of UI agents will hide, while the rest will run from the shooter. Table 1 shows that if the hide probability is set to 20% then the remaining 80% will run toward the nearest exit after exiting the designated lecture hall.

Table 1. Hide and run probability parameter manipulation per iteration.

Iteration	1	2	3	4	5	6	7	8	9	10	11
Hide	0	.1	.2	.3	.4	.5	.6	.7	.8	.9	1
Run	1	.9	.8	.7	.6	.5	.4	.3	.2	.1	0

## Model Runtime Properties: Limitations and Iterations by Parameter Manipulation

- The duration of the model was limited to six minutes, which was equivalent to the Parkland Shooting event (Fausset et al. 2018).
- The casualty rate was limited to one casualty per 21.2 seconds by the active shooter, again based on the Parkland Shooting event (Fausset et al. 2018).
- The target selection began once all 600 unarmed individuals entered the lecture halls, which limited the first casualty to occur only in the lecture hall.
- If there were no potential target within the first 21.2 seconds, the shooter required an additional 21.2 seconds to select another target.

- The unarmed individuals, who were hiding in the lecture hall, could not attempt to escape if the shooter entered the lecture hall.

To allow for position and time variation, each hide parameter was run 100 times and measured the following output data:

- Hide parameter (Double)
- Run parameter (Double)
- Number of unarmed individuals in the lecture hall (Integer)
- Number of unarmed individuals in the hallway (Integer)
- Number of unarmed individual casualties (Integer)
- Number of unarmed individuals who successfully evacuated (Integer)
- Number of lecture hall casualties of unarmed individuals (Integer)

## Results

Figure 3 suggests a highest average total casualty rate of 9.43 of 600 (1.57%), where 20% hid and 80% ran to the nearest exit. The lowest average total casualty rate was 4.23 of 600 (0.71%), where all unarmed individual agents were seeking shelter within the lecture halls. The highest average hallway casualty rate was 5.24 of 600 (0.87%) with 80% hide probability, where the lowest rate was 3.60 of 600 (0.6%) with 0% hide probability. The highest average lecture hall casualty rate was 4.79 of 600 (0.79%) with 10% hide probability with the lowest at 0 of 600 (0%) with 100% hide probability.

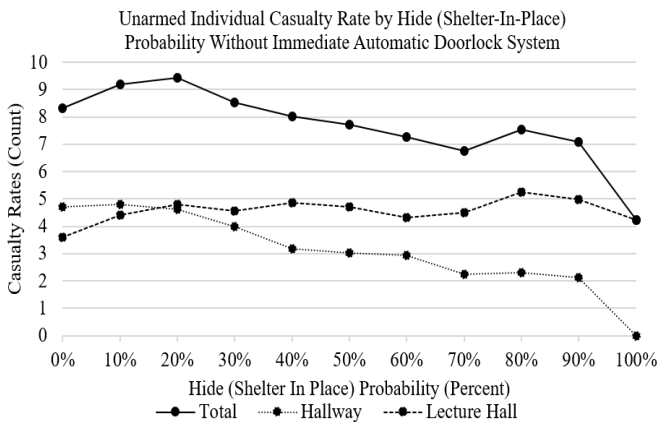


Figure 3. Unarmed individual casualty rate by hide (shelter-in-place) probability without immediate automatic door lock system.

Figure 4 shows a comparison of the casualty rate of unarmed individuals to the automatic door lock system by the hide (shelter-in-place) probability.

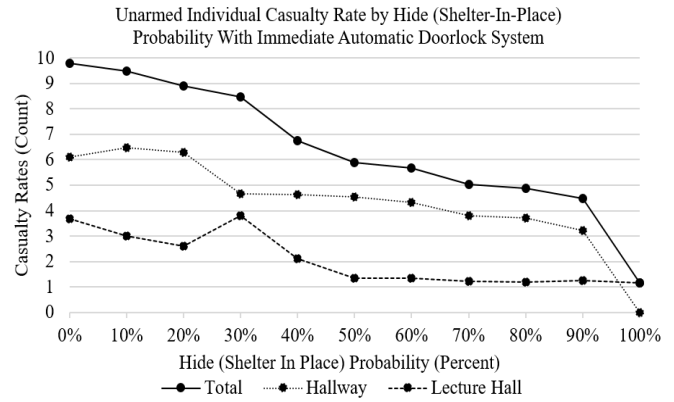


Figure 4. Unarmed individual casualty rate by hide (shelter-in-place) probability with immediate automatic door lock system.

Figure 4 suggests the lowest average casualty rate of 1.15 (0.19%) was reported when all unarmed individuals hide from the shooter with the automatic door lock mechanism in place. The highest average casualty rate was 9.8 (1.63%), where all agents had to evacuate from the lecture hall, regardless of the automated lock mechanism. The highest average hallway casualty rate was 6.47 of 600 (1.08%) with 90% hide probability, where the lowest rate was 0 of 600 (0%) with 0% hide probability. The highest average lecture hall casualty rate was 3.81 of 600 (0.64%) with 30% hide probability with the lowest at 1.15 of 600 (0.19%) with 100% hide probability.

The locations were made up of total, hallway, and lecture hall, where casualty probabilities were measured based on two parameter manipulations. The first parameter was the hide probability, ranging from 0%, where zero unarmed individuals (UI) evacuated the lecture hall, to 100%, where all 600 evacuated to the nearest exit. The second was a Boolean parameter, which determined whether the automatic door lock system was in place or not. The total casualty probabilities were calculated by dividing the total number of casualties by 600. The hallway and the lecture hall casualty probabilities were calculated by dividing the casualty rates by the total number of either run or hide casualties. For example, hallway casualty probability was calculated by dividing the hallway casualty rate to the total number of evacuees. Figure 5 compares the UI agent's casualty probability without the immediate door lock system, based on the agent's location of casualty.

Figure 5 illustrates the total, hallway, and lecture hall casualty probability, based on the hide parameter without the door lock system. The highest total casualty probability was 1.57%, when 20% of unarmed individuals hid and 80% ran to the nearest exit. The lowest total casualty probability was 0.71%, when 100% evacuated to the nearest exit. The lec-

ture hall casualty probability was the highest at 7.35%, when 10% of the unarmed individuals evacuated. The lowest lecture hall casualty probability was 0.6%, when everyone sought shelter. The highest hallway casualty probability was 3.53%, when 90% hid upon the first discharge. The lowest hallway casualty probability was 0%, when 100% hid from the shooter. Figure 6 compares the UI agent's casualty probability with the immediate door lock system, based on the agent's location of casualty.

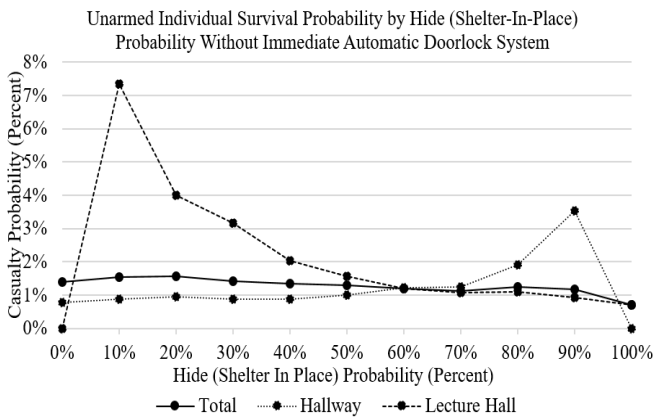


Figure 5. Unarmed individual survival probability by hide (shelter-in-place) probability without immediate automatic door lock system.

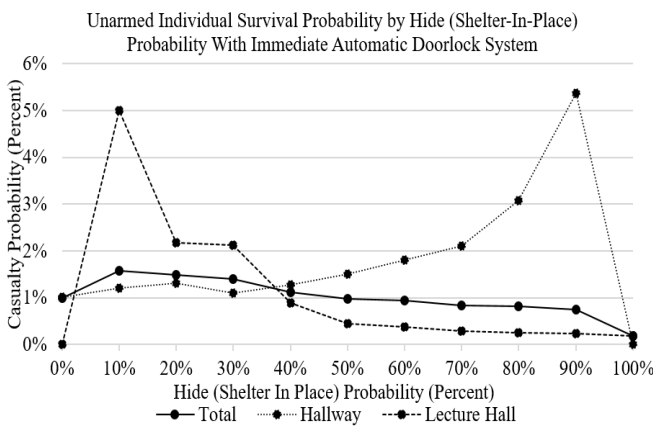


Figure 6. Unarmed individual survival probability by hide (shelter-in-place) probability with immediate automatic door lock system.

Figure 6 illustrates the total, hallway, and lecture hall casualty probability, based on the hide parameter with the door lock system. The highest total casualty probability was 1.58% during the 10% hide probability, where the lowest probability was 0.19% during the 100% hide probability. The highest lecture hall casualty probability was 5% during the 10% hide probability, where the lowest lecture hall probability was 0.19 for the 100% hide probability. The highest hallway casualty probability was 5.36% during the

90% hide probability. The lowest hallway casualty probability was 0% for the 100% hide probability. Table 2 compares the total casualty probabilities for the model with and without a door lock.

Table 2. Total casualty probability with and without door lock per iteration.

Probability	Total Casualty Probability	Survival Probability Difference		
		Without Door Lock	With Door Lock	
Hide	Run			
0%	100%	1.39%	1.00%	-.39%
10%	90%	1.53%	1.58%	.05%
20%	80%	1.57%	1.48%	-.09%
30%	70%	1.42%	1.41%	-.01%
40%	60%	1.34%	1.12%	-.21%
50%	50%	1.29%	.98%	-.31%
60%	40%	1.21%	.94%	-.27%
70%	30%	1.13%	.84%	-.29%
80%	20%	1.26%	.81%	-.44%
90%	10%	1.18%	.75%	-.44%
100%	0%	.71%	.19%	-.51%
Average Casualty Probability	1.27%	1.01%	-.26%	

The overall casualty probability decreased by 0.26%, with the highest casualty rate decrease of 0.51% with all agents sheltering in place. In contrast, the casualty rate increased by 0.05% for the 10% hide probability. Table 3 compares the hallway casualty probabilities for the model with and without a door lock. The overall casualty probability increased by 0.59%, with the highest casualty rate increasing by 1.83% when 90% sought shelter. There was no decrease in casualty probability for hallway casualties. Table 4 compares the lecture hall casualty probabilities for the model with and without a door lock. The overall casualty probability decreased by 1.01%, with the highest casualty rate decrease of 2.35% when 10% sought shelter. In contrast, the casualty rate increased by 0.01% when all agents evacuated.

Table 3. Hallway casualty probability with and without door lock per iteration.

Probability	Total Casualty Probability	Survival Probability Difference		
		Without Door Lock	With Door Lock	
Hide	Run			
0%	100%	.79%	1.02%	.23%
10%	90%	.89%	1.20%	.31%
20%	80%	.96%	1.31%	.35%
30%	70%	.87%	1.11%	.23%
40%	60%	.88%	1.29%	.40%
50%	50%	1.01%	1.51%	.50%
60%	40%	1.22%	1.80%	.58%
70%	30%	1.25%	2.11%	.86%
80%	20%	1.92%	3.08%	1.16%
90%	10%	3.53%	5.36%	1.83%
100%	0%	0%	0%	0%
Average Casualty Probability	1.21%	1.80%	.59%	

Table 4. Lecture hall casualty probability with and without door lock per iteration.

Probability	Total Casualty Probability	Survival Probability Difference		
		Without Door Lock	With Door Lock	
Hide	Run			
0%	100%	.60%	.61%	.01%
10%	90%	7.35%	5.00%	-2.35%
20%	80%	4.02%	2.18%	-1.84%
30%	70%	3.17%	2.12%	-1.06%
40%	60%	2.03%	.88%	-1.14%
50%	50%	1.57%	.45%	-1.11%
60%	40%	1.20%	.37%	-.83%
70%	30%	1.07%	.29%	-.78%
80%	20%	1.09%	.25%	-.85%
90%	10%	.92%	.23%	-.69%
100%	0%	.71%	.19%	-.51%
Average Casualty Probability	2.16%	1.14%	-1.01%	

## Conclusions

Assuming locked doors are effective at separating potential victims from the shooter, this study further demonstrated the value of agent-based models to design effective policies by testing the impact of automatic door locking technology on casualty rates. Using this model, shelter-in-place proved to be an effective strategy for reducing the impact of an active shooter event with the greatest reduction shown when all individuals sought to shelter in place. The implementation of an automated door lock system, triggered by discharge detection, did decrease the total casualty rate an average of 0.26% over 100 simulated iterations. The total lecture hall casualty rate decreased an average of 1.01%, while the total hallway casualty rate increased by 0.59%. While the automatic door locking system did reduce casualties, individuals in the hallways also saw an increase in casualties, due to limits in protection from the shooter and evacuation paths.

## References

- Anklam, C., Kirby, A., Sharevski, F., & Dietz, J. (2015). Mitigating active shooter impact: analysis for policy options based on agent/computer-based modeling. *Journal of Emergency Management*, 13(3). Retrieved from <https://www.wmpllc.org/ojs-2.4.2/index.php/jem/article/view/176>
- Bonabeau, E. (2002). Agent-based modeling: Methods and techniques for simulating human systems. *Proceedings of the National Academy of Sciences*, 99(suppl. 3), 7280-7287.
- Buster, C. (2008). Patrol response challenge. *NCJRS Law and Order*, 56(6), 62-68.
- City of Houston. (2012). *Run.Hide.Fight—Ready Houston*. Retrieved from <http://readyhouston.wpengine.com/suspicious-activity/run-hide-fight/>
- Department of Homeland Security [DHS]. (2017). *Active shooter recovery guide*. Retrieved from <https://www.dhs.gov/sites/default/files/publications/active-shooter-recovery-guide-08-08-2017-508.pdf>
- Fausset, R., Kovaleski, S., & Mazzei, P. (2018). On a day like any other at a Florida school, 6 minutes of death and chaos. *The New York Times*. Retrieved from <https://www.nytimes.com/2018/02/16/us/stoneman-douglas-shooting.html>
- Federal Bureau of Investigation. (2016). Quick look: 220 Active shooter incidents in the United States between 2000-2016 FBI. Retrieved from <https://www.fbi.gov/about/partnerships/office-of-partner-engagement/active-shooter-incidents-graphics>

---

Federal Emergency Management Agency [FEMA]. (2017). Incident command system resources. Retrieved from <https://www.fema.gov/incident-command-system-resources>

Scott, M., & Schwartz, J. (2014). *The police response to active shooter incidents*. Washington, D.C: Police Executive Research Forum. Retrieved from [https://www.policeforum.org/assets/docs/Critical\\_Issues\\_Series/the%20police%20response%20to%20active%20shooter%20incidents%202014.pdf](https://www.policeforum.org/assets/docs/Critical_Issues_Series/the%20police%20response%20to%20active%20shooter%20incidents%202014.pdf)

## Biographies

**JAE YONG LEE** is a graduate research assistant in computer and information technology at Purdue University. He earned his BA in public relations and minor in computer and information technology in 2017 from Purdue University. His research interests include examining the effectiveness of active shooter response and mitigation policies with agent-based modeling utilizing AnyLogic. Mr. Lee may be reached at [jaelee@purdue.edu](mailto:jaelee@purdue.edu)

**J. ERIC DIETZ** is a Professor of Computer and Information Technology at Purdue University and the Director of Purdue Homeland Security Institute. He earned his BS and MS degrees in chemical engineering in 1986 from Rose-Hulman Institute of Technology, and PhD in chemical engineering from Purdue University. He had served as Founding Executive Director for the Indiana Department of Homeland Security and retired Lieutenant Colonel from the US Army. Dr. Dietz may be reached at [jedietz@purdue.edu](mailto:jedietz@purdue.edu)

# INSTRUCTIONS FOR AUTHORS: MANUSCRIPT FORMATTING REQUIREMENTS

The INTERNATIONAL JOURNAL OF ENGINEERING RESEARCH AND INNOVATION is an online/print publication designed for Engineering, Engineering Technology, and Industrial Technology professionals. All submissions to this journal, submission of manuscripts, peer-reviews of submitted documents, requested editing changes, notification of acceptance or rejection, and final publication of accepted manuscripts will be handled electronically. The only exception is the submission of separate high-quality image files that are too large to send electronically.

All manuscript submissions must be prepared in Microsoft Word (.doc or .docx) and contain all figures, images and/or pictures embedded where you want them and appropriately captioned. Also included here is a summary of the formatting instructions. You should, however, review the [sample Word document](http://ijeri.org/formatting-guidelines) on our website (<http://ijeri.org/formatting-guidelines>) for details on how to correctly format your manuscript. The editorial staff reserves the right to edit and reformat any submitted document in order to meet publication standards of the journal.

The references included in the References section of your manuscript must follow APA-formatting guidelines. In order to help you, the sample Word document also includes numerous examples of how to format a variety of scenarios. Keep in mind that an incorrectly formatted manuscript will be returned to you, a delay that may cause it (if accepted) to be moved to a subsequent issue of the journal.

1. **Word Document Page Setup:** Two columns with ¼" spacing between columns; top of page = ¾"; bottom of page = 1" (from the top of the footer to bottom of page); left margin = ¾"; right margin = ¾".
2. **Paper Title:** Centered at the top of the first page with a 22-point Times New Roman (Bold), small-caps font.
3. **Page Breaks:** Do not use page breaks.
4. **Figures, Tables, and Equations:** All figures, tables, and equations must be placed immediately after the first paragraph in which they are introduced. And, each must be introduced. For example: "Figure 1 shows the operation of supercapacitors." "The speed of light can be determined using Equation 4:"

5. **More on Tables and Figures:** Center table captions above each table; center figure captions below each figure. Use 9-point Times New Roman (TNR) font. Italicize the words for table and figure, as well as their respective numbers; the remaining information in the caption is not italicized and followed by a period—e.g., "*Table 1.* Number of research universities in the state." or "*Figure 5.* Cross-sectional aerial map of the forested area."
6. **Figures with Multiple Images:** If any given figure includes multiple images, do NOT group them; they must be placed individually and have individual minor captions using, "(a)" "(b)" etc. Again, use 9-point TNR.
7. **Equations:** Each equation must be numbered, placed in numerical order within the document, and introduced—as noted in item #4.
8. **Tables, Graphs, and Flowcharts:** All tables, graphs, and flowcharts must be created directly in Word; tables must be enclosed on all sides. The use of color and/or highlighting is acceptable and encouraged, if it provides clarity for the reader.
9. **Textboxes:** Do not use text boxes anywhere in the document. For example, table/figure captions must be regular text and not attached in any way to their tables or images.
10. **Body Fonts:** Use 10-point TNR for body text throughout (1/8" paragraph indentation); indent all new paragraphs as per the images shown below; do not use tabs anywhere in the document; 9-point TNR for author names/affiliations under the paper title; 16-point TNR for major section titles; 14-point TNR for minor section titles.  

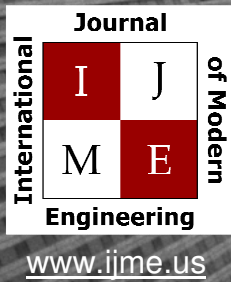
11. **Personal Pronouns:** Do not use personal pronouns (e.g., "we" "our" etc.).
12. **Section Numbering:** Do not use section numbering of any kind.
13. **Headers and Footers:** Do not use either.

- 
14. **References in the Abstract:** Do NOT include any references in the Abstract.
  15. **In-Text Referencing:** For the first occurrence of a given reference, list all authors—last names only—up to seven (7); if more than seven, use “et al.” after the seventh author. For a second citation of the same reference—assuming that it has three or more authors—add “et al.” after the third author. Again, see the *sample Word document* and the *formatting guide for references* for specifics.
  16. **More on In-Text References:** If you include a reference on any table, figure, or equation that was not created or originally published by one or more authors on your manuscript, you may not republish it without the expressed, written consent of the publishing author(s). The same holds true for name-brand products.
  17. **End-of-Document References Section:** List all references in alphabetical order using the last name of the first author—last name first, followed by a comma and the author’s initials. Do not use retrieval dates for websites.
  18. **Author Biographies:** Include biographies and current email addresses for each author at the end of the document.
  19. **Page Limit:** Manuscripts should not be more than 15 pages (single-spaced, 2-column format, 10-point TNR font).
  20. **Page Numbering:** Do not use page numbers.
  21. **Publication Charges:** Manuscripts accepted for publication are subject to mandatory publication charges.
  22. **Copyright Agreement:** A copyright transfer agreement form must be signed by all authors on a given manuscript and submitted by the corresponding author before that manuscript will be published. Two versions of the form will be sent with your manuscript’s acceptance email.
  23. **Submissions:** All manuscripts and required files and forms must be submitted electronically to Dr. Philip D. Weinsier, manuscript editor, at [philipw@bgsu.edu](mailto:philipw@bgsu.edu).
  24. **Published Deadlines:** Manuscripts may be submitted at any time during the year, irrespective of published deadlines, and the editor will automatically have your manuscript reviewed for the next-available issue of the journal. Published deadlines are intended as “target” dates for submitting new manuscripts as well as revised documents. Assuming that all other submission conditions have been met, and that there is space available in the associated issue, your manuscript will be published in that issue if the submission process—including payment of publication fees—has been completed by the posted deadline for that issue.

Missing a deadline generally only means that your manuscript may be held for a subsequent issue of the journal. However, conditions exist under which a given manuscript may be rejected. Always check with the editor to be sure. Also, if you do not complete the submission process (including all required revisions) within 12 months of the original submission of your manuscript, your manuscript may be rejected or it may have to begin the entire review process anew.

Only one form is required. Do not submit both forms!

The form named “paper” must be hand-signed by each author. The other form, “electronic,” does not require hand signatures and may be filled out by the corresponding author, as long as he/she receives written permission from all authors to have him/her sign on their behalf.



Print ISSN: 2157-8052  
Online ISSN: 1930-6628



## INTERNATIONAL JOURNAL OF MODERN ENGINEERING

### ABOUT IJME:

- IJME was established in 2000 and is the first and official flagship journal of the International Association of Journal and Conferences (IAJC).
- IJME is a high-quality, independent journal steered by a distinguished board of directors and supported by an international review board representing many well-known universities, colleges and corporations in the U.S. and abroad.
- IJME has an impact factor of **3.00**, placing it among the top 100 engineering journals worldwide, and is the #1 visited engineering journal website (according to the National Science Digital Library).

### OTHER IAJC JOURNALS:

- The International Journal of Engineering Research and Innovation (IJERI)  
For more information visit [www.ijeri.org](http://www.ijeri.org)
- The Technology Interface International Journal (TIIJ).  
For more information visit [www.tiij.org](http://www.tiij.org)

### IJME SUBMISSIONS:

- Manuscripts should be sent electronically to the manuscript editor, Dr. Philip Weinsier, at [philipw@bgsu.edu](mailto:philipw@bgsu.edu).

For submission guidelines visit  
[www.ijme.us/submissions](http://www.ijme.us/submissions)

### TO JOIN THE REVIEW BOARD:

- Contact the chair of the International Review Board, Dr. Philip Weinsier, at [philipw@bgsu.edu](mailto:philipw@bgsu.edu).

For more information visit  
[www.ijme.us/ijme\\_editorial.htm](http://www.ijme.us/ijme_editorial.htm)

### INDEXING ORGANIZATIONS:

- IJME is indexed by numerous agencies.  
For a complete listing, please visit us at [www.ijme.us](http://www.ijme.us).

### Contact us:

**Mark Rajai, Ph.D.**

Editor-in-Chief  
California State University-Northridge  
College of Engineering and Computer Science  
Room: JD 4510  
Northridge, CA 91330  
Office: (818) 677-5003  
Email: [mrajai@csun.edu](mailto:mrajai@csun.edu)



[www.tiij.org](http://www.tiij.org)



[www.ijeri.org](http://www.ijeri.org)

The International Journal of Engineering Research & Innovation (IJERI) is the second official journal of the International Association of Journals and Conferences (IAJC). IJERI is a highly-selective, peer-reviewed print journal which publishes top-level work from all areas of engineering research, innovation and entrepreneurship.



## **IJERI Contact Information**

General questions or inquiries about sponsorship of the journal should be directed to:

Mark Rajai, Ph.D.

Founder and Editor-In-Chief

Office: (818) 677-5003

Email: [editor@ijeri.org](mailto:editor@ijeri.org)

Department of Manufacturing Systems Engineering & Management

California State University-Northridge

18111 Nordhoff St.

Room: JD3317

Northridge, CA 91330